# DEVELOPMENT OF NON-INVASIVE METHODS FOR IMAGING INFLAMMATORY RESPONSE

by

YI-TING TSAI

Presented to the Faculty of the Graduate School of

The University of Texas at Arlington in Partial Fulfillment

of the Requirements

for the Degree of

DOCTOR OF PHILOSOPHY

THE UNIVERSITY OF TEXAS AT ARLINGTON

May 2013

ACKNOWLEDGEMENTS

A number of individuals have contributed to my development as a researcher here at the University of Texas at Arlington, and I'd like to take this opportunity to express my gratitude to them for their contributions. I would first like to thank my dissertation committee, Dr. Connie Hsia, Dr. Hanli Liu, Dr. Jer-Tsong Hsieh, Dr. Xiankai Sun, and Dr. Liping Tang, for their guidance and suggestions during development of this dissertation. Specifically, I would like to acknowledge my advisor, Dr. Liping Tang, for the opportunity to pursue my research interest and for his guidance in developing and focusing the outline of this dissertation.

In addition, I would like to thank members of my lab group for their assistance as part of this dissertation and prior work. I would like to thank Dr. Hong Weng and Dr. Jinhui Shen for helping me with all the animal measurements and for providing support and helpful information when required. I also express my thanks to Dr. Jun Zhou for fabricating all the imaging probes. I would like to thank David Baker and Dr. Ashwin Nair for their patience and assistance in working out mechanisms in preparation for this dissertation.

Finally, I would ultimately like to thank my family for their support which has made this entire venture possible. To my husband, Zi-Jing Lin, I would like to express my sincerest appreciation for his patience. Without his companionship and the hope that this in some way could contribute to a better life for him and my son, Cheng-chih Lin, this work would not have been possible. I would also like to thank my mother and father, Tsan-Ho Tsai and Su-Chin Chan, for believing in me and supporting me throughout my academic career.

April 17, 2013

ABSTRACT

DEVELOPMENT OF NON-INVASIVE METHODS FOR IMAGING INFLAMMATORY RESPONSE

Yi-Ting Tsai, PhD

The University of Texas at Arlington, 2013

Supervising Professor: Liping Tang

Persistent inflammatory cell reactions are responsible for the pathogenesis of a variety of inflammatory diseases. Although many non-invasive imaging methods have been used in the clinics to monitor the extent of inflammatory responses, almost all of them are based on indirect detection of inflammation-associated anatomical or structure changes of tissues and organs. To fill the gap, our laboratory has focused research efforts on detecting different processes of inflammatory responses. Our results can be summarized in the sequence of inflammatory responses – edema formation, inflammatory cell recruitment, inflammatory product release, and cell death.

Shortly after medical device implantation or injury, edema results from fibrin deposition in tissue at the implant/injury site. A near-infrared (NIR)-based fibrin probe was fabricated to detect fibrin deposition. We found that the fibrin probe can be used to quantify the extent of fibrin formation *in vitro* as early as 15 minutes post subcutaneous particle implantation *in vivo*. Subsequent studies also revealed that fibrin deposition is mediated by mast cell activation and there is a good relationship between short term fibrin deposition and long term inflammatory responses to biomaterial implants. The accumulation of inflammatory cells, especially macrophages and neutrophils, is a hallmark of inflammatory responses. For the detection of

neutrophils and macrophages, formyl peptide receptor-targeting and folate receptor-targeting NIR probes were fabricated, respectively. Both probes can be used to monitor neutrophil and macrophage recruitment at the biomaterial implant sites. These probes similarly have a strong relationship with the acquired fluorescent intensities and the inflammatory cell counts from histological analyses. Both probes can be used to non-invasively monitor inflammatory responses, including foreign body reactions and infection, in real time. Activated inflammatory cells, particularly polymorphonuclear neutrophils (PMNs), can release reactive oxygen species (ROS) to eradicate foreign bodies and microorganisms. We find that L-012-associated chemiluminescence imaging can be used to identify and to quantify the extent of inflammatory responses. Furthermore, regardless of differences among animal models, there is a good linear relationship between chemiluminescence intensity and PMN numbers surrounding inflamed tissue. The release of inflammatory products and associated cell death will lead to the reduction of pH in tissue also called as tissue acidosis. A novel pH ratiometric optical probe was fabricated carrying both pH-sensitive and pH-insensitive fluorescence dyes for *in vivo* optical imaging. By taking the ratio of fluorescence intensities at different wavelengths, these probes provide excellent measurement, distribution, and change of tissue pH at different times. We find that the ratiometric pH changes are a good indicator of inflammatory responses, further confirmed by histological analyses.

Finally, to explore the possibility of monitoring fluorescence distribution via 3D models, we developed a 3D reconstruction model to enable mapping of the spatio-temporal distribution of fluorescence probes. This model may lead to enhanced understanding of *in vivo* fluorescent imaging modalities providing detailed location and anatomical structure information. We present the evaluation of the system and method in recovering three-dimensional surfaces from phantom data and living mice. The results obtained in this study showed our 3D reconstruction model could provide the shape, depth, and bio-distribution information for our inflammation model.

TABLE OF CONTENTS

LIST OF ABBREVIATIONS

| Abbreviations | Term |
|---|---|
| APMA | N-(3-aminopropyl) methacrylamide |
| cFLFLF | Cinnamoyl-Phe-(D)Leu-Phe-(D)Leu-Phe |
| CT | Computed tomography |
| DEX | Dexamethasone |
| DTPA | Diethylene triamine pentaacetic acid |
| EDC | 1-Ethyl-3-(3-dimethylaminopropyl) carbodiimide |
| FITC | Fluorescein isothiocyanate |
| FMT | Fluorescence molecular tomography |
| GPRPPGGSKGC | Gly-Pro-Arg-Pro-Pro-Gly-Gly-Ser-Lys-Gly-Cys |
| H&E | Hematoxylin-Eosin |
| HBSS | Hank's balanced salt solution |
| IHC | Immunohistochemical |
| LPS | Lipopolysaccharide |
| MPIO | Mircometer-sized Iron Oxide Particles |
| MRI | Magnetic Resonance Imaging |
| MTS | 3-(4,5-dimethylthiazol-2-yl)-5-(3-carboxymethoxyphenyl)-2-(4-sulfophenyl)-2H-tetrazolium) |
| NIR | Near-infrared |
| PBS | Phosphate buffered saline |
| PEG | Polyethylene glycol |
| PET | Positron emission tomography |

| | |
|---|---|
| PLA | Poly(lactic acid) |
| PMA | Phorbol 12-myristate 13-acetate |
| PMNs | Polymorphonuclear neutrophils |
| PNIPAM | Poly(N-isopropylacrylamide) |
| PNIPAM-co-St | Poly(N-isopropyl acrylamide-co-styrene) |
| PNIPAM-$NH_2$ | Aminated-poly(N-isopropylacrylamide) |
| PS | Polystyrenes |
| PU | Polyurethane |
| $R^2$ | Correlation Coefficient |
| ROI | Region of Interest |
| ROS | Reactive oxygen species |
| SPECT | Single-photon emission computed tomography |
| SPIO | Superparamagnetic iron oxide |
| UV | Ultraviolet |

LIST OF ILLUSTRATIONS

LIST OF TABLES

## DECLARATION OF ACADEMIC ACHIEVEMENT

The research performed for this dissertation was conceived, conducted, analyzed, written, and submitted for publication primarily by the author of this dissertation with the following exceptions:

• The synthesis and characterization of fibrin-affinity probe (Chapter 2.2.1), formyl peptide receptors-probe (Chapter 3.2.2.1), folate receptors-probe (Chapter 3.3.2.1), and pH probes (Chapter 4.3.3.2) were performed by Dr. Jun Zhou. Dr. Jun Zhou also wrote the sections in the chapter that describe the methods and results of the aforementioned techniques, and created Figures 3.1, 3.18, and 4.21.

• All the histological or Immunohistochemical staining images and quantification results shown in Chapter 2.2.5, 3.2.2.4, 3.3.2.4, 4.2.2.3, and 4.3.2.8 were performed by Dr. Hong Weng.

• The cell toxicity assay and cell culture study was done by other lab members, and created Figures 2.3, 3.3, 3.20, 3.21, and 4.22.

# CHAPTER 1

## 1.1 Inflammatory responses

Inflammation defends the body against harmful substances, disposes of dead or dying tissue and promotes the renewal of normal tissue. The process of inflammation begins immediately after injury/infection. Based on the duration of the reaction, inflammation can be divided into acute and chronic inflammation. Acute inflammation is a host response initiated by the increased movement of plasma and leukocytes (especially granulocytes) from the blood into the injured tissues. Prolonged inflammation, also called chronic inflammation, leads to a progressive shift in composition of cells present at the inflamed site and is characterized by simultaneous destruction and healing of the tissue.

### *1.1.1 Acute inflammatory responses and fibrin deposition*

Acute inflammation is an immediate response lasting for a few minutes, several hours, or one to two days. The typical signs of localized acute inflammation are swelling, redness, heat, pain, and loss of function. Swelling is caused by extensive vasodilation leading to increased blood flow, which also causes heat and redness. Increased vascular permeability leads to fluid leakage (edema) and temporary fibrin deposition in tissue which provides a base for cellular infiltration. Activated platelets attach to the fibrin matrix to further prevent excessive bleeding. Neutrophils are the first immune cells drawn to the site of injury/infection, arriving within a few hours. They are short-lived, fast migrating phagocytic cells. As neutrophils subside, they make way for macrophages. Macrophages tend to remain at a wound site for a few days to weeks and play multiple roles in inflammation and wound healing. Active neutrophils have been demonstrated to release ROS. Lactic acid and acidic by-products are increasingly produced and concentrated in and near inflamed tissues, causing tissue acidosis decreasing tissue pH to the order of at least 0.5–1.0 pH unit [1, 2].

*1.1.2 Mast cells*

Mast cells, a leukocyte subset present in the skin, contain many granules rich in histamine, chemokines and cytokines [3]. Following injury, resident mast cells degranulate to release a variety of granular products within minutes. The release of mast cells granular products (Table 1.1) promotes inflammatory responses and edema formation. Specifically, during degranulation, mast cells release a wide variety of vasoactive mediators (histamine, prostaglandins and others) which leads to an increase in capillary permeability. The increased vascular permeability in turn leads to the translocation of plasma constituents (and blood cells) into the tissue. The extravasation of fibrinogen from the blood into extravascular areas (where tissue factor is expressed in local cells) is followed by formation of fibrin and edema [4-6]. Mast cells have also been reported to modulate the recruitment of neutrophils into the site of injury [7].

*1.1.3 Neutrophils*

Neutrophils play an important role in inflammation and infection, and are also the most abundant cell type among all immune cells migrating from the blood stream to the sites of trauma or infection [3, 8, 9]. Neutrophils arrive at the site of a biomaterial implant within a few hours and then peak around 18-24 hours [10, 11]. Due to the short life span, neutrophils are often present at the injured site for less than a few days. Recruited neutrophils release free radicals and a variety of granular products prior to phagocytosis by macrophages [12]. It is well established that neutrophils release a large variety of highly active antimicrobial substances (ROS, cationic peptides, eicosanoids) and proteases (elastase, cathepsin G, proteinase 3, urokinase-type plasminogen activator) (Table 1.1) [3, 13]. Activated neutrophils and their products have also been shown to cause the degradation of polymeric implants and tissue engineering scaffolds [14, 15]. Furthermore, it has been suggested that the accumulation of activated neutrophils around an injury site may lead to increased fibrotic reactions, delayed tissue regeneration, or even tissue damage [16].

Table 1.1 Inflammatory cells, their functions and mediators released in tissue repair. (Modified from [3])

| Cell type | Functions | Mediators |
|---|---|---|
| Mast cells | Control vascular permeability | Histamine |
| | Control influx of PMN | Chymase, tryptase, MIP-1α, MCP-1 |
| | Regulate tissue remodeling | Serotonin, thromboxane |
| Neutrophils | Phagocytosis of infectious agents | ROS, cationic peptides, eicosanoids, proteases (elastase, cathepsinG, PR-3, and uPA) |
| | Degranulation | |
| | Amplify inflammatory response | TNF-α, IL-1β, IL-6 |
| | Stimulate repair response | VEGF, IL-8 |
| Macrophages | Phagocytosis of dead cells and tissue debris | |
| | Amplify inflammatory response | TNF-α, IL-1β, and IL-6 |
| | Anti-inflammatory function | IL-10, TGF-β1 |
| | Stimulate repair response: angiogenesis, fibroplasia | PDGF, VEGF, bFGF, TGF-α, and TGF-β |
| | Fibrolysis | t-PA, uPA, u-PAR, and PAI-1/-2 |

bFGF, basic fibroblast growth factor; FGF, fibroblast growth factor; MC, mast cell; MIP-1α, macrophage inflammatory protein 1α; MCP-1, monocytes chemoattractant protein-1; PDGF, platelet derived growth factor; PMN, polymorphonuclear leukocyte; ROS, reactive oxygen species; TGF, transforming growth factor; TNF, tumor necrosis factor; uPA, urokinase-type plasminogen activator; VEGF, vascular endothelial growth factor; IL, Interleukin

*1.1.4 Macrophages*

The accumulation of macrophages is a hallmark of inflammation [17]. Macrophages are a major constituent of mononuclear leukocytes. At the inflamed site, most macrophages are peripheral blood monocytes recruited from the blood. At the site of injury, macrophages typically perform three major functions; antigen presentation, phagocytosis, and immunomodulation through production of various cytokines and growth factors [18]. Recent studies have also suggested that polarized macrophages play a critical role in different phases of inflammatory responses. Pro-inflammatory M1 macrophages release products, including cytokines (interferon gamma, granulocyte-monocyte colony stimulating factor, and TNF-α), extracellular matrix proteins, and other chemical mediators (Table 1.1). At the beginning of wound healing, pro-

regenerative M2 macrophages release several anti-inflammatory cytokines (IL-10 and TGF-β) and several growth factors to enhance tissue regeneration. Since the products of polarized macrophages participate in both beneficial and detrimental outcomes in inflammation, therapeutic interventions that target macrophages and their products may open new avenues for controlling inflammatory diseases.

*1.1.5 Acidosis*

Tissue acidosis is another phenomenon which usually occurs in and surrounding inflamed tissue. Tissue acidosis is a hallmark of inflammatory diseases [11, 12]. Specifically, high hydrogen ion concentrations have been found in inflamed tissues (down to pH 5.4), in fracture-related hematomas (down to pH 4.7), in cardiac ischemia (down to pH 5.7) and in and around malignant tumors [19, 20].The acidification within diseased tissue is likely caused by cell death and hyperactive inflammatory cells [21].

*1.1.6 Chronic inflammation*

If the immune response of the body fails to stop, the inflammation becomes chronic. The chronic phase may last for days to years [22]. Chronic inflammation is not as uniform as acute inflammation. It is generally associated with the presence of lymphocytes, macrophages and the proliferation of small blood vessels and fibroblasts. Not surprisingly, chronic inflammation can cause significant tissue damage. Unregulated inflammation has also been linked to a variety of diseases including cancer, heart disease and autoimmune disease [23-25].

## 1.2 Imaging modality for Inflammation response

The extent of inflammatory responses can be determined by several established methods, including enzyme measurements and histological evaluation. The numbers of recruited macrophages/monocytes and neutrophils can be quantified using methods to measure the activities of non-specific esterase and myeloperoxidase, respectively [5, 10, 26]. However, enzyme extraction from implants and surrounding tissue can be tedious and time consuming. Histological analyses of tissue biopsies involving, studying, staining, and microscopic evaluation

are the most common method to diagnose inflammatory diseases. In addition to being invasive and unreliable, histological analyses are time consuming, require large numbers of animals, and can provide only semi-quantitative assessment of inflammatory reactions at one time point [27-29]. Many imaging procedures have been developed to overcome the challenges of diagnosis and therapy for monitoring inflammatory diseases. These imaging techniques include Computed Tomography (CT), Positron Emission Tomography (PET), Single-Photon Emission Computed Tomography (SPECT), planar scintigraphy, Magnetic Resonance Imaging (MRI), ultrasound, and optical imaging. All these techniques have specific advantages and disadvantages. To better understand the roles of these modalities in relation to the nuclear medicine techniques, it is important to be aware of their respective advantages and disadvantages (Table 1.2) [30-32].

*1.2.1 CT/ PET /SPECT*

CT is a highly reproducible imaging modality with an excellent spatial resolution. However, the disadvantages of CT include exposure of the patient to radiation and the lack of functional information. Furthermore, the use of contrast medium to enhance image contrast may also be limited or impossible in patients with impaired renal function or previous allergic reactions. Although PET and SPECT have limited spatial resolution (PET down to 3–5 mm; SPECT down to 8–10 mm), their asset is high contrast resolution, offering functional and molecular information with high sensitivities in the nano- or pico-molar range (PET, SPECT). The radiation exposure is mostly low however, dependent on the radiotracer used, may reach the radiation exposure of an abdominal CT scan [30].

A variety of radiotracers have been applied for detection of inflammation via these imaging modalities. Radiolabeled leukocytes are the gold standard to image inflammation [33], including $^{18}$F-FDG, autologous white blood cells (WBCs [leukocytes]) labeled with $^{99m}$Tc or $^{111}$In, $^{99m}$Tc-labeled bisphosphonates, $^{67}$Ga-citrate, $^{99m}$Tc-labeled nanocolloids, and $^{99m}$Tc- or $^{111}$In-labeled proteins. Although the benefit of this method is their specificity, their use is limited to the detection of acute inflammation [22].

Table 1.2 Comparison of imaging systems for small animals. (Modified from [32])

| Modality | Resolution | Depth | Signal | Radiation | Training |
|---|---|---|---|---|---|
| PET | 0.8-1.4mm | No limit | γ-rays | Yes | Yes |
| SPECT | 0.8-1.4mm | No limit | γ-rays | Yes | Yes |
| CT | 50um | No limit | X-ray | Yes | Yes |
| MRI | 10-100um | No limit | RF wave | No | Yes |
| Ultrasound | 50um | mm | Sound waves | No | Yes |
| Optical imaging | 0.3um | <1mm | Light waves | No | No |

MRI, Magnetic resonance imaging; PET, Positron emission tomography; SPECT, Single photon emission computed tomography; CT, Computed tomography. RF, radiofrequency,

*1.2.2* MRI

As compared with CT/PET/SPECT, MRI has higher resolution and also has some potential to obtain functional information. Most importantly, it causes no radiation exposure. Although it has become widely available, the relatively long examination time may be prone to movement artifacts. MRI is also relatively expensive compare to other modalities. Moreover, there are limitations to the scanning of patients with pacemakers, implants, and other devices.

In recent times, MRI is widely used to detect inflammatory arthritis [34-36], neuro-oncology and central nervous system inflammatory pathologies [37]. The sensitivity of MRI can be improved by increasing magnetic field strength and also via a variety of signal amplification schemes based on chemical exchange. Recently, targeted contrast agents for MRI with high specificity and sensitivity have become available for various applications, such as tumors, cerebral ischemia or stroke, carotid atherosclerosis, multiple sclerosis, and inflammation diseases [38]. Several small ligands, peptides, antibodies (such as antigen-specific T cells), plasma biomarkers, or small protein domains (such as HER-2 affibodies, VCAM-1), have also been applied to achieve targeting by MRI [38-40]. These targeting moieties are usually linked to MRI contrast agents (such as $^{1}H$, $^{19}F$, SPIO, MPIO) with high sensitivity in order to enhance the sensitivity of the contrast agents [38, 41-43].

*1.2.3 Ultrasound*

Ultrasound has been increasingly used in preclinical studies. The use of ultrasound in the clinical setting has many advantages which include: widely available, quick, inexpensive, and no radiation exposure. Ultrasound has better spatial resolution (may reach below 1 mm) and can also provide limited functional information such as blood flow by Doppler ultrasonography. However, the results of ultrasound are highly operator-dependent. The penetration and reflection of the sound waves in tissue may also be affected by gas (bowel) or dense structures (bone), and structures deep within the body may be difficult to visualize because the image quality suffers from the longer wavelengths used for deep imaging.

Many studies have shown that ultrasound has been used to measure the expression of vascular markers during the inflammation process. The contrast agents used in ultrasound may be fabricated to bind to certain proteins that become expressed in inflammatory diseases, like Crohn's disease, atherosclerosis, and even heart attacks. Some studies targeted specific cells, such as endothelial cells of blood vessels, or leukocytes. In addition, there are certain receptors expressed specifically in the inflamed blood vessels, like VCAM-1, ICAM-1, and E-selectin (cell adhesion molecules) [44]. When contrast agents are designed to target with ligands that bind these molecules, ultrasound may be used to detect the site of inflammation. Some studies have used microbubbles with monoclonal antibodies with P-selectin, ICAM-1, and VCAM-1 binding [45]. However, the targeting efficiency to the molecule was poor and most microbubbles were rapidly detached from the binding target [46]. To improve upon this some studies have shown high adhesion efficiencies using a dual-ligand selectin-integrin cell arrest system [47]. Although this technique has been proven to increase adhesion efficiency, the receptor to polymer microsphere targeting has not been sufficient to allow clinical use of targeted contrast-enhanced ultrasound agents for inflammation imaging [48, 49].

*1.2.4 Optical imaging*

Optical imaging has recently been applied to diagnose physiological and pathophysiological conditions, including cancer, arthritis, infection and cardiovascular disease [50-53]. Many approaches can be used for optical imaging, including fluorescence, luminescence, etc. The main advantage of optical imaging methods over many clinical imaging modalities is that optical imaging probes are not radioactive and have lesser concerns related to safety to the patients [54]. However, the major drawback of optical imaging is the limited penetration depth of light.

Fluorescent dyes are commonly used in optical imaging. The penetration depth of fluorescent light is related to the absorption and scattering of light (excitation wavelength). Light can be absorbed by endogenous chromophores in living tissue (such as hemoglobin, melanin, and lipids). Absorption and scattering of light is decreasing with increasing wavelength. The penetration depths below ~700 nm (visible wavelengths) are only a few millimeters. Water absorption can also interfere with signal-to-background ratio above 900 nm. Most optical imaging applications are carried out in the near infrared (NIR) region (700-900 nm) because NIR light can penetrate deeper (up to several centimeters) [32]. For NIR imaging, there are many commercially available NIR fluorophores, including Kodak X-SIGHT Dyes and Conjugates, Pz 247, DyLight 750 and 800 Fluors, Cy 5.5 and 7 Fluors, Alexa Fluor 680 and 750 Dyes, IRDye 680 and 800CW Fluors. These fluorophores have been use to label different ligands for targeting various receptors and cells [55, 56]. Some probes that can be activated, such as Cathespin B, Cathespin D, Neutrophil Elastase, and metalloproteinase 2 (MMP-2), have also been developed for imaging inflammation. In general, these probes are dark (quenched) in their native state and become fluorescent after reacting with specific proteases [31]. Since these probes are not designed to target inflamed tissue or inflammatory cells, the sensitivity of these probes in quantifying inflammatory responses is typically poor.

Luminescence is another optical imaging modality which is widely used for preclinical models. The difference between fluorescence and luminescence is that electronic excited state of luminescence is derived from the product of a chemical reaction. The major advantage of luminescence is its high sensitivity with minimal or no background. To detect inflammation, most of the progress in luminescent imaging has been made in the area of reactive oxygen species (ROS) detection using luminal or L-012 [57-59].

### 1.3 Three-dimensional imaging methodology for optical imaging

Many optical methods, including fluorescent and bioluminescent imaging, generate a planar image, flattening the animal into a 2D projection. Although 2D optical imaging could provide the quantitative results for evaluation of the fluorescent probe, it may lose the depth and spatial relationships in a 3D structure. To improve these issues, several optical 3D fluorescence models have been built to generate the quantification and visualization information of fluorescent probes [60-64]. Fluorescence molecular tomography (FMT) technology enables quantitative imaging of the fluorescent probe, or marker concentration to the picomolar level with no tissue depth limitation [64]. However, the costs of these techniques are significantly higher than traditional fluorescence reflection imaging. Some commercial products, such as MARS (Multimodal Animal Rotation System) of Carestream, can generate or at least approximate a 3D dataset at different angles (30º increment). However, they are often inadequate for the task of producing specimens that retain their 3D structure. Despite the 3D approximation optical tomography systems could give to determine spatial relationships, it still cannot provide the anatomical structure. Some researchers co-registered optical methods with micro-CT or MRI methods. However, they cause errors and are difficult to achieve simultaneously. Even though a new system can combine micro-CT and FMT in the same machine, the high hardware costs and differing levels of achievable accuracy and detail in the captured geometric models offset the advantages offered by the system. To fill the gap, a

robust, simple, cost effective, and flexible 3D modeling apparatus with different modalities will be developed for a variety of different biomedical applications.

## 1.4 Aims of this Dissertation to Improve Inflammatory Imaging Strategies

The aim of this dissertation is to examine the *in vivo* outcomes of two different strategies to continuously monitor and quantify inflammatory responses *in vivo*. The overall goals of the proposed work are to evaluate four groups of imaging probes developed in our laboratory on their ability to target four key processes of inflammatory/infection response *in vivo* (**1.4.1**). Additionally, we aim to create three-dimensional visualization models to observe the distribution for different biological applications (**1.4.2**). The following specific aims outline the path taken to accomplish the proposed objectives.

### *1.4.1 Development of optical imaging tools for detecting biological application*

Various optical imaging tools will be used to detect different characteristics of inflammatory responses, including fibrin deposition; inflammatory cell accumulation, and tissue acidosis. Many researchers have shown that fibrin deposition is a key mediator of inflammatory responses [4, 65]. In chapter 2, by fabricating probes with high affinity to fibrin, we explore whether fibrin accumulation can be used to assess the extent of inflammatory responses. Neutrophils and macrophages are two major cell types which are responsible for triggering inflammatory responses [5, 11, 26, 66, 67]. In chapter 3, two different fluorescence imaging probes have been fabricated to detect activated neutrophils and macrophages via their highly expressed formyl peptide receptors and folate receptors, respectively. Inflammatory diseases are also associated with the accumulation of activated inflammatory cells, particularly PMNs, which release ROS to eradicate foreign bodies and microorganisms [68, 69], and often tissue acidosis (where pH decreases) [19, 20]. In chapter 4, we apply L-012 as a chemiluminescence agent to monitor biomaterial-induced ROS *in vivo*, and also design pH imaging probes using a ratiometric imaging technique to detect inflammatory responses by measuring the associated tissue acidosis. All imaging agents are tested for their ability to detect and quantify their

respective targets both *in vitro* and *in vivo* using an optical imager.

*1.4.2 Development of three-dimensional visualization models from optical imaging*

The ability to visualize imaging modalities using 3D models will lead to a better understanding of the aforementioned processes [70-72]. To explore the possibility of monitoring fluorescence distribution via 3D models, 3D reconstruction models will be developed to enable mapping of the spatio-temporal distribution of the fluorescent probes leading to better understanding *in vivo* (Chapter 5).

# CHAPTER 2

# DEVELOPMENT OF OPTICAL IMAGING PROBE FOR EDEMA FORMATION

## 2.1 Introduction

Fibrinogen/fibrin accumulation at the implant site has been shown to be critical in triggering foreign body reactions, including coagulation, inflammation (such as heart attack, ischemic stroke, and pulmonary embolism) and infection [5, 11, 73, 74]. Since fibrin is a ligand for CD54 (ICAM-1), CD11b/CD18 (CR3, Mac-1), and CD11c/CD18 (CR4, p150/95), as well as adhesion-promoting receptors expressed by endothelial cells, neutrophils, monocytes/macrophages, subsets of dendritic, natural killer, and T cells, localized fibrin deposition is thought to be responsible for localized immune cell recruitment [75-77]. In addition, the interaction of Mac-1 (CD11b/CD18) and fibrin formation could trigger the production and release of inflammatory chemokines, such as tumor necrosis factor alpha (TNF-α) and IL-1β, by inflammatory cells [78, 79]. Since many studies have shown that fibrin depletion substantially alleviates many inflammatory diseases, such as glomerulonephritis, lung ischemia, and rheumatoid arthritis, fibrin-mediated immune responses are essential to the pathogenesis of many inflammatory diseases [65].

Many cells and processes may contribute to localized fibrin deposition and consecutive edema formation [6]. Substantial evidence shows that mast cells play a pivotal role in the initiation of edema and fibrin deposition in many inflammatory diseases, including cutaneous anaphylaxis, antigen-induced arthritis, and also reverse passive Arthurs reaction [4]. In addition, our previous studies suggest that mast cell activation (degranulation with histamine release) is mainly responsible for acute/chronic inflammatory responses to biomaterial implants [5, 80-82]. These results suggest that the monitoring of mast cell activation-mediated fibrin deposition at the implant site may serve as an early indicator of foreign body reactions.

Recently, fluorescence dye-labeled cross-linked iron oxide (CLIO) nanoparticles functionalized with FXIII-specific peptide (GNQEQVSPLTLLKC) and fibrin(ogen) targeting peptide (GPRPPGGSKGC) have been prepared for *in vitro* detection of clots by both MR and optical imaging modalities to detect fibrin deposition in inflammation and tumor sites [83]. However, none of these probes have been investigated for their ability to detect fibrin deposition surrounding biomaterial implants. In addition, the potential role of mast cell activation on fibrin deposition on biomaterials has yet to be determined.

## 2.2 Investigation of a fibrin-affinity NIR probe for fibrin detection and mast cell participation

### *2.2.1 Purpose*

Mast cell activation can trigger edema in allergic and inflammatory disease, and also contribute to the fibrin deposition. This study is aimed at developing an imaging tool to detect fibrin deposition which can also reflect the extent of mast cell activation, and then predict the extent of foreign body response. For that, NIR-based imaging probes were tested for their ability to target fibrin both *in vitro* and *in vivo*. First, the specificity of fibrin-affinity probes to surface fibrin was studied *in vitro*. Using an *in vivo* imaging system, the effectiveness of fibrin-affinity probes in quantifying the extent of biomaterial implant-mediated fibrin accumulation was also assessed. Finally, fibrin-affinity probes were also tested for their ability to continuously monitor and measure the extent of biomaterial-mediated fibrin deposition and mast cell activation *in vivo*.

### *2.2.2 Material and methods*

#### 2.2.2.1 Materials

The fibrin-affinity probe was fabricated based on a modified procedure [84]. Direct conjugated probes were fabricated by fibrin-targeting peptides (GPRPPGGSKGC) and fluorescence dye (Oyster800) according to manufacturer's protocol from BOCA Scientific. In brief, 5.5 mg of fibrin-affinity peptides (GPRPPGGSKGC) were dissolved in 1 ml of PBS buffering solution (pH: 8.0), and then 1.0 ml of Oyster800 dye PBS solution (pH: 8.0) were

added to the above peptide solution. The mixture was incubated overnight at 4$^{o}$C. The unbound dye was removed via dialysis against deionized water.

2.2.2.2 Optical property of fibrin-affinity probe

The optical property and bioactivities of the fibrin probe were characterized. Absorbance and fluorescence spectra of the fibrin-affinity probe were measured using UV-Vis spectrophotometer (Lambda 19 Spectrometer, PerkinElmer, MA) and fluorescence spectrometer (Shimadzu RF-5301PC, Japan), respectively. The cytotoxicity of the fibrin-affinity probe was then determined using 3T3 fibroblasts and MTS assay as described earlier [85].

2.2.2.3 *In vitro* fibrin binding tests

Fibrin-coated glass beads were produced by incubating all glass beads with 200 ml fibrinogen (4000 mg/ml in isotonic PBS; 50 mM sodium phosphate plus 100 mM NaCl, pH 7.4) in individual wells of a 48-well plate. Following the addition of fibrinogen, 0.5 ml (1 U/ml) thrombin was added to each well to generate a homogeneous fibrin coating on glass beads. Surface fibrin was then allowed to fully polymerize at 37°C for 5 minutes [5]. The glass beads were then transferred to new wells for the probe binding tests. For that, 100 µl of fibrin-binging probe (GPRPPGGSKGC-Oyster800) or its control (Oyster800) (10 µg/ml) were added to the wells and incubated at 37°C for 1 hour. The supernatant on the glass beads was removed and then washed three times to remove unbound probes from the glass beads.

2.2.2.4 *In vivo* inflammation models

Female Balb/c mice (20-25 gram), purchased from Taconic Farms (Germantown, NY), were used in this investigation. The animal experiments were approved by the University of Texas at Arlington Institutional Animal Care and Use Committee (IACUC). We evaluated the specificity of the fibrin probes by administration of thrombin in the subcutaneous space. To test the efficacy of the fibrin-affinity probe in targeting fibrin formation, 25U thrombin was injected subcutaneously as described earlier (n = 5) [86]. To induce localized inflammatory responses, 10 mg $TiO_2$ was injected subcutaneously into various locations on the back of mice (n = 6). To

investigate the effect of time, 60 µl of fibrin-affinity probe solution (0.5 mg/ml) was administered intravascularly after $TiO_2$ injection. The fluorescence intensities of $TiO_2$ at different time points were recorded. To determine the role of mast cell activation on fibrin deposition, mice were subcutaneously injected with 100 µg of compound 48/80 (n = 6), a mast cell activator, or saline. To trigger varying extents of inflammatory responses in the same animals, 10mg of $TiO_2$, $SiO_2$ and PLA particles were used as control substances to trigger various extents of foreign body reactions (n = 6). PLA particles (5–10 µm in diameter) were synthesized as previously demonstrated [12]. Finally, to investigate the role of mast cells in the biomaterial inflammatory responses, mast cell-deficient WBB6F1-W/$W^v$ mice and their normal littermates, WBB6F1-+/+ were used. Different particles, $TiO_2$, $SiO_2$ and PLA, were injected subcutaneously into both mice (n = 3). After the treatments, 60 µl of fibrin-affinity probe solution (0.5 mg/ml) was administered intravascularly. Whole body images of mice were then taken using KODAK *In Vivo* FX Pro (f-stop: 2.5, excitation filter: 760 nm, emissions filter: 830 nm, 4 × 4 binning; Carestream Health, Rochester, NY).

2.2.2.5 IHC evaluation of biomaterial-mediated tissue responses

At the end of the studies, the test animals were sacrificed and the implantation sites/inflamed tissues were isolated for histological analyses. All tissues underwent cryosection followed by Hematoxylin-Eosin (H&E) staining and also fibrin staining. All histological sections were imaged under a Leica DMLP microscope (Leica, Wetzlar, Germany) equipped with a Qimaging RetigaExi 1394 digital camera (Qimaging, Surrey, British Columbia, Canada).

2.2.2.6 Data Analyses

For *in vitro* binding study, fluorescence intensities of glass beads were measured using a Tecan Infinite M 200 plate reader (San Jose, CA) at emission of 830nm (excitation at 760 nm). The fluorescence intensities of whole body images were calculated using Carestream Molecular Imaging Software, Network Edition 4.5 (Carestream Health). In brief, regions of interests (ROIs) were drawn over the implantation locations after background correction, and

the mean fluorescence intensities for all pixels in the fluorescent images was determined. Quantitative histological analysis (H&E) of the total number of inflammatory cells throughout the implantation sites was determined using NIH ImageJ (National Institutes of Health, Bethesda, MD) [12, 87]. For IHC evaluation, the relative amount of fibrin (area covered by fibrin) was determined via a pre-determined threshold and the total thresholding area calculated using NIH ImageJ [88].

2.2.2.7 Statistical analyses

All the results will be expressed as mean ± Standard deviation (SD). One-way analysis of variance (ANOVA) and student t-test were performed to compare the difference between groups. A value of $p < 0.05$ was considered to be significant.

*2.2.3 Results*

2.2.3.1 Establishment of relationship between fibrin accumulation and inflammatory responses surrounding biomaterial implants

To investigate foreign body reactions to particle implants, $TiO_2$ (~5-10 mm in diameter, 50 ml, 10% w/v) and PLA particles (~5-10 μm in diameter, 50 ml, 10% w/v) and saline (100 ml) were injected subcutaneously (n = 3). After injection for 24 hours, tissue samples were harvested and then analyzed histologically. By analyzing implants and surrounding tissue, we found that both $TiO_2$ and PLA sites had a large amount of fibrin accumulation. However, the relative amount of fibrin at the $TiO_2$ implantation sites were more than those in PLA sites (Figure 2.1). Furthermore, saline controls had very low or no fibrin accumulation during the same time period. By quantifying the inflammatory cells and fibrin amounts, we found that there is a good relationship between the relative amount of fibrin and the inflammatory cell recruitment (Figure 2.2). These results support that fibrin deposition may serve as viable early indicators of foreign body reactions.

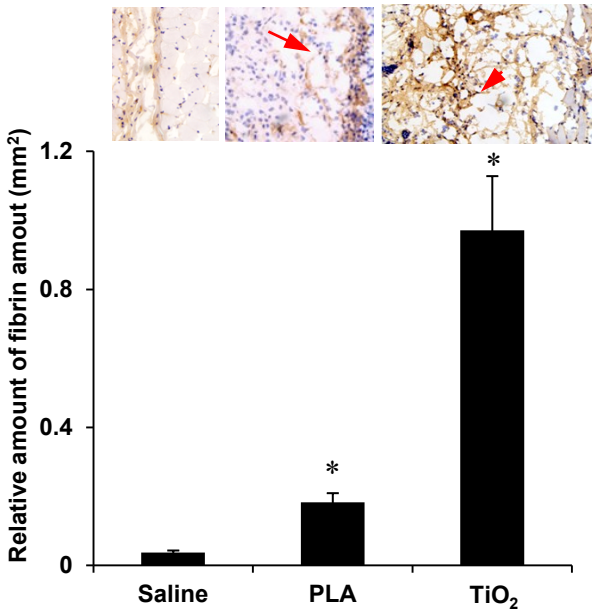


Figure 2.1 Fibrin accumulation at subcutaneous sites with particle implants of $TiO_2$ and PLA, and saline in Balb/C mice for 24 hours. Representative images of tissue sections stained with fibrin antibody show fibrin accumulation at the implant sites. The amounts of fibrin deposition (area covered by fibrin) were determined via a pre-determined threshold and the total thresholding area calculated by ImageJ. Vertical lines denote ± 1SD (n = 3 in all cases). Significance vs. saline treatment: * $p<0.05$

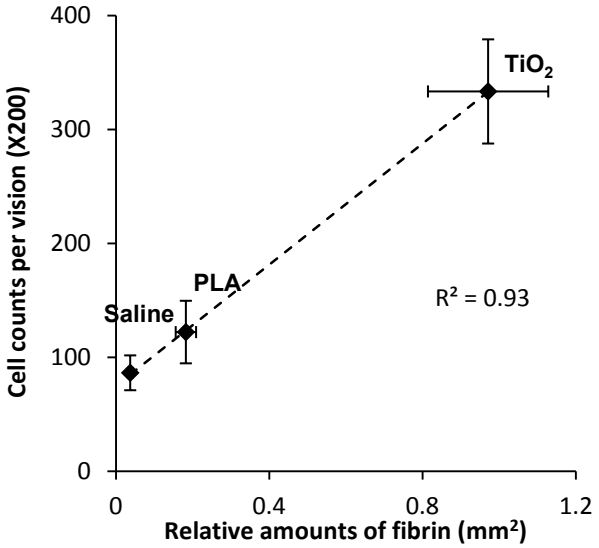


Figure 2.2 Correlation between inflammatory cell counts and fibrin accumulation at the sites of $TiO_2$, PLA implant and saline in the subcutaneous space in mice for 24 hours. The inflammatory cells counts per view field were quantified on H&E stained slides. The amounts of fibrin deposition were quantified via a pre-determined threshold and calculated the total thresholding area. Vertical and parallel lines denote ± 1SD (n = 3 in all cases). The linear regression has coefficient $R^2$= 0.93.

2.2.3.2 Properties of the fibrin-affinity probe

For real time monitoring of fibrin accumulation *in vivo*, we developed an imaging probe using fibrin affinity peptide and NIR dye. Fluorescence spectroscopic results demonstrate that the fluorescence spectrum of the fibrin-affinity probe has a maximum emission at 812 nm (excited at 796 nm) (Figure 2.3a). The cytotoxicity of the fibrin-affinity probe was determined using 3T3 fibroblasts and MTS assay. We found that the cytotoxicity due to the fibrin-affinity probe was not statistically significant over the studied concentration range (up to 0.35 ug/ml, Figure 2.3b), indicating that the above probes possess adequate cell compatibility for further in vivo testing.

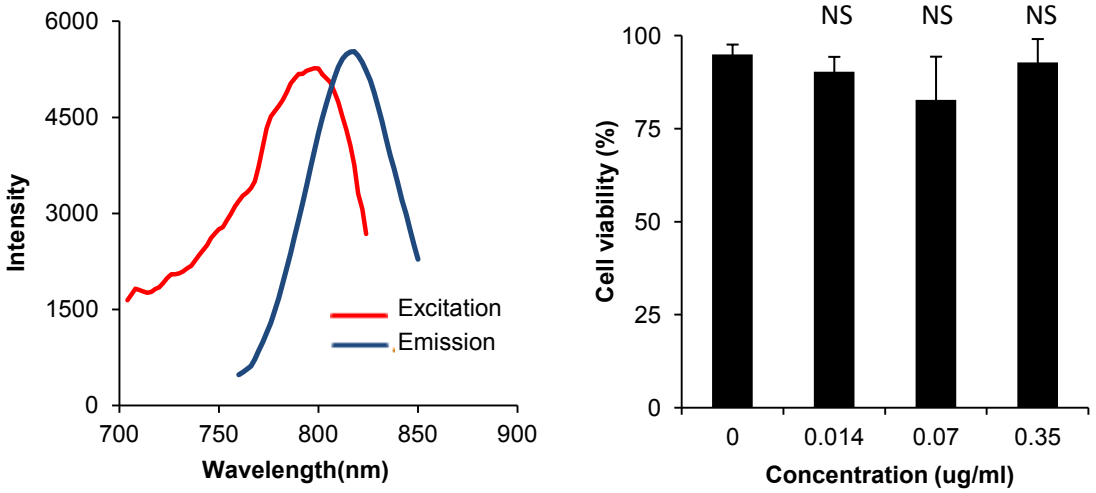


Figure 2.3 Characterization of the optical property and cell viability of fibrin-affinity probes. (a) Excitation and emission spectra of fibrin-affinity probes was determined based on fluorescent spectrum. (b) Cytotoxicity study of fibrin-affinity probes (0 - 0.35 µg/ml) was carried out using 3T3 fibroblasts and MTS assay. Vertical lines denote ± 1SD (n= 5 in all cases). Significance vs. no treatment: NS – no statistical significance.

2.2.3.3 *In vitro* fibrin targeting of the fibrin-affinity probe

The ability of the fibrin-affinity probe to detect fibrin deposition was evaluated using fibrin-coated glass beads. After incubation with fibrin-binging probe (GPRPPGGSKGC-Oyster800) or its control (Oyster800) for 1 hour, the glass beads were observed under an optical microscope. As expected, the fluorescence signals on the fibrin sites (shown in red)

were very high (fluorescence intensity = 81.95). However, there was almost no control probe accumulation in the fibrin area (fluorescence intensity = 31.96, Figure 2.4a). These findings support the hypothesis that fibrin-affinity probes may be used to specifically detect the presence of fibrin. To further study whether the probes can be used to quantify the amounts of fibrin *in vitro*, various amounts of fibrin on the surface of glass beads were incubated with the probes and the fibrin-associated fluorescence intensities were determined. In support of the hypothesis, a good linear relationship was found between amount of fibrin and fluorescence intensities in the fibrin probe group. In contrast, the intensities in the control group were close to the background (Figure 2.4b). Overall, the *in vitro* results support that fibrin-affinity probes can preferentially bind to fibrin and may be used to quantify the amount of fibrin *in vitro*.

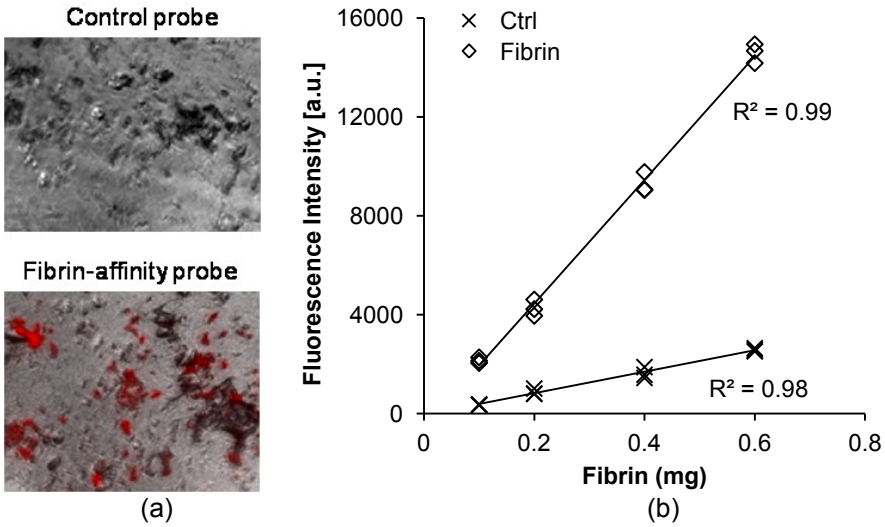


(a) (b)

Figure 2.4 Investigation of the specificity of the fibrin-affinity probe and dye only control probe to label fibrin-coated glass beads following 1 hour incubation *in vitro*. (a) Fluorescence microscopy images of fibrin coated glass beads following incubation with fibrin-affinity probes and control probes. (b) Correlation between relative amounts of surface fibrin and fluorescence intensities associated with either fibrin-affinity probes or control probes. The linear regression has coefficient $R^2$= 0.99 in fibrin-affinity probes and $R^2$= 0.98 in control probes.

2.2.3.4 Detection of fibrin accumulation *in vivo* using fibrin-affinity probes

First, to evaluate whether fibrin-affinity probes can be used specifically to assess the deposition of fibrin *in vivo*, thrombin (25 Units) and saline, as a control, were injected

subcutaneously, and then 60 µl of the fibrin-affinity probe (0.5 mg/ ml) was administrated intravascularly right after thrombin/saline injection. It is well known that thrombin prompts the polymerization and deposition as fibrin [79]. We found that the fibrin probe accumulated at the implantation site within 30 minutes of thrombin injection. Fluorescence signals increased over time, and the signal intensities at the thrombin implantation sites were consistently higher than those in saline control sites (Figure 2.5).

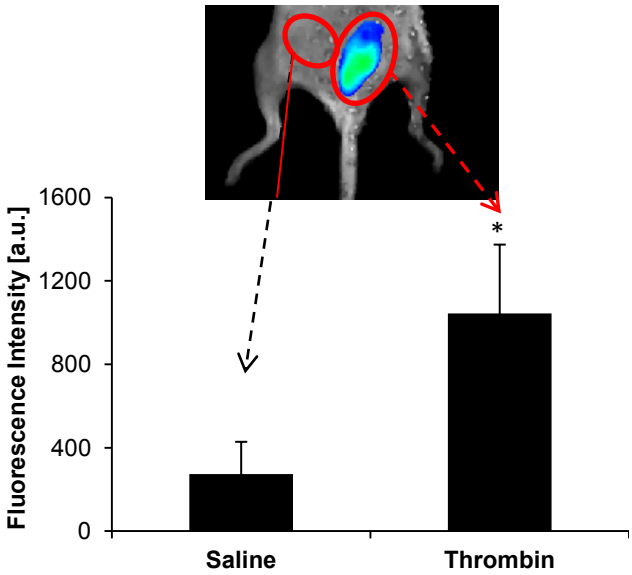


Figure 2.5 Accumulation of intravenously injected fibrin-affinity probe at the sites 30 minutes following administration of thrombin (25 units) or saline (as control) in mice. The representative merged fluorescence and white light image shows the accumulation of fibrin-affinity probe at different injection sites. The fluorescent intensities at the implantation sites were quantified (bottom). Vertical lines denote ± 1SD (n = 5 in all cases). Significance vs. saline treatment: * $p<0.05$.

The effectiveness of the fibrin-affinity probe in detecting fibrin deposition at biomaterial implant sites was then tested *in vivo*. $TiO_2$ (10 mg/50 µl) was administered subcutaneously on the back of mice prior to intravascular administration of a 60 µl of fibrin-affinity probe solution (0.5 mg/ml). Following the fibrin-affinity probe injection, the whole body images were recorded at different time points (Figure 2.6). A substantial increase in fluorescence intensity was found at the $TiO_2$ injection site, in as short a time period as 10 minutes following probe injection, in comparison with the saline control. The accumulation of the fibrin-affinity probe at the $TiO_2$ site

increased with time and reached a plateau around 1 hour, where the $TiO_2$ treatment triggered ~16 times higher fluorescence intensity than the saline control (Figure 2.6).

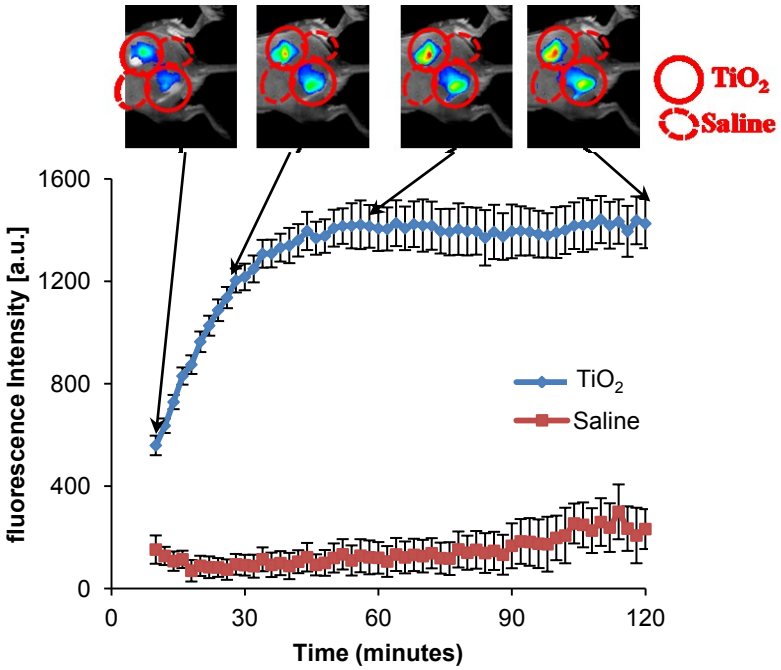


Figure 2.6 Accumulation of intravenously injected fibrin-affinity probe at different time (10-120 minutes) following subcutaneous implantation of $TiO_2$ particles or saline in mice. The representative merged fluorescence and white light image shows the accumulation of fibrin-affinity probe at different injection sites. The averages of fluorescent intensities at the implantation sites were quantified. Vertical lines denote ± 1SD (n = 6 in all cases).

To confirm that the accumulation of the fibrin-affinity probe was mediated by localized fibrin deposition, control studies were carried out in which animals were implanted with $TiO_2$ nanospheres in the presence or absence of anticoagulant – heparin (10 Units/site). Many studies have shown that heparin can prevent the formation of a stable fibrin clot by inhibiting the activation of the fibrin stabilizing factor [89, 90]. The probes were then intravenously administered and images were captured 1 hour after the probe injection. As expected, treatment with heparin substantially reduced the accumulation of the fibrin-affinity probe by about two fold at the implant site (Figure 2.7). These results show that the fibrin-affinity probe can be used to non-invasively monitor fibrin deposition at the implant sites. Since there is a good relationship

between fibrin deposition and inflammatory responses, it is likely that fibrin-affinity can also be used as a tool for the early detection of foreign body reactions.

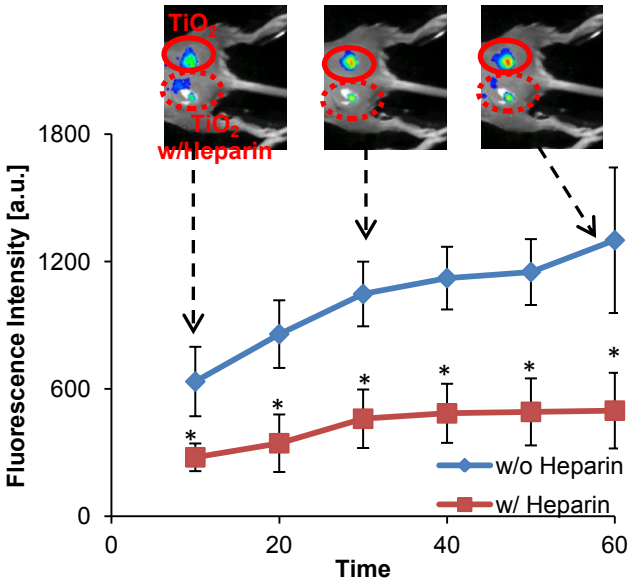


Figure 2.7 The localized treatment of heparin (10 units/site) or saline (as control) on the accumulation of intravenously administered fibrin-affinity probe at the sites of subcutaneously implanted $TiO_2$ particles. The representative merged fluorescence and white light image shows the accumulation of fibrin-affinity probe at different injection sites. The averages of fluorescent intensities at the implantation sites were quantified and compared. Vertical lines denote ± 1SD (n = 6 in all cases). Significant vs. without heparin treatment: * $p<0.05$.

2.3.3.5 Effect of mast cells on fibrin deposition using fibrin-affinity probes

Many previous studies have shown that mast cell activation is essential to fibrin accumulation in different inflammatory diseases. We thus hypothesize that mast cell activation is responsible for fibrin deposition surrounding biomaterial implants. To test the hypothesis, we investigated fibrin accumulation in mice treated with mast cell activator, compound 48/80 (100μg/site), or saline [91]. As expected, the fluorescence signal at the compound 48/80 site was approximately 16 fold higher than the saline control site (Figure 2.8). By quantifying fibrin densities from histological staining, we also found a large amount of fibrin accumulation at the site of compound 48/80 implantation, whereas less fibrin accumulation was found at saline sites (Figure 2.9).

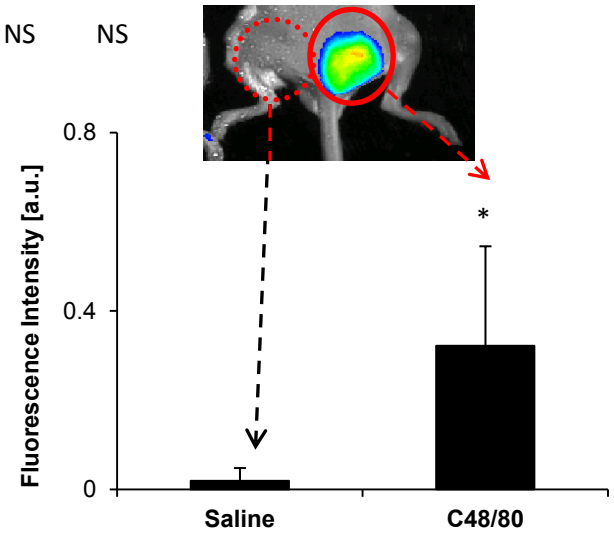


Figure 2.8 The effect of mast cell activation on fibrin accumulation. Activation of mast cells in the subcutaneous space of Balb/C mice was achieved with the injection of compound 48/80 for 2 hours and followed with intravenous with subcutaneous injection of fibrin-affinity probes. Saline injection was used as controls. After probe injection for 1 hour, whole body images of fibrin-affinity probe-associated fluorescence were taken and the fluorescent intensities were quantified and compared. The averages of fluorescent intensities at the implantation sites were quantified. Vertical lines denote ± 1SD (n = 6 in all cases) Significance vs. saline treatment: * $p<0.05$. (C48/80: compound 48/80)

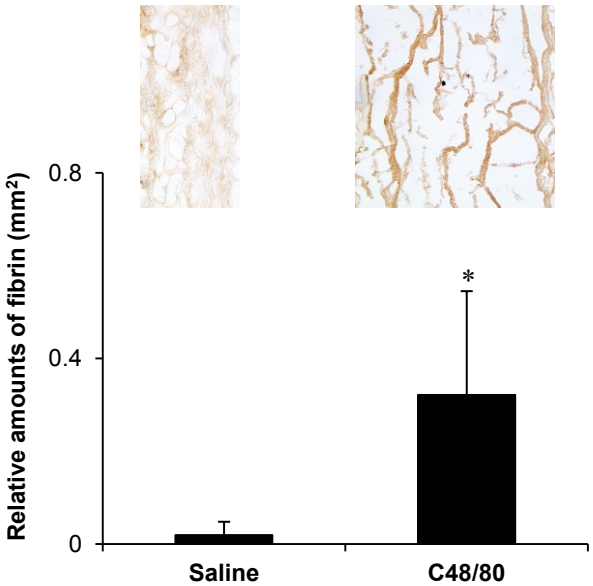


Figure 2.9 The subcutaneous accumulation of fibrin following the injection of compound 48/80 and saline for 2 hours was quantified based on relative stain intensities of the tissue sections using ImageJ software. Vertical lines denote ± 1SD (n = 6 in all cases). Significance vs. saline treatment: * $p<0.05$. (C48/80: compound 48/80)

To determine the relationship between fibrin-affinity probe accumulation and implant-mediated fibrin, we correlated both the relative amounts of fibrin with the fluorescence intensity. Our results show a good linear trend between the relative amount of fibrin and the fluorescence intensity (Figure 2.10).

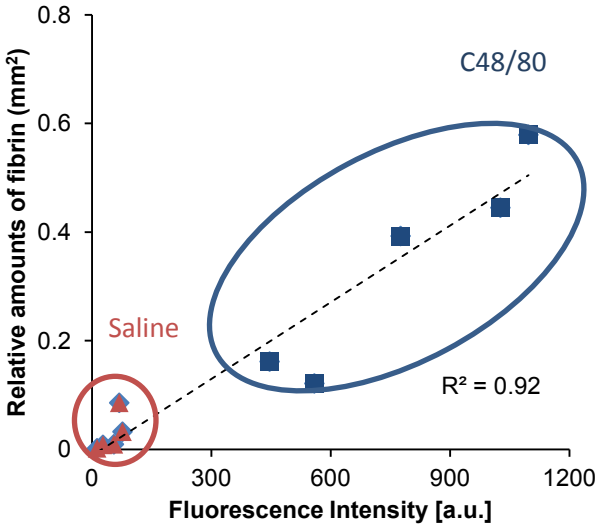


Figure 2.10 Correlation between relative fibrin accumulation (Figure 2.9) and fibrin-affinity probe associated fluorescent intensities (Figure 2.8) at the sites of saline and compound 48/80 injection sites. Vertical and parallel lines denote ± 1SD (n = 6 in all cases). The linear regression has coefficient $R^2$= 0.92. (C48/80: compound 48/80)

2.3.3.6 Quantification of inflammatory reactions induced by different types of implants

Subsequent studies were carried out to explore the possibility of using fibrin-affinity probes to assess inflammatory reactions to different biomaterial implants *in vivo*. $TiO_2$, $SiO_2$ and PLA particles were chosen as model materials which have been shown to trigger strong and weak inflammatory responses, respectively [92, 93]. After material implantation for 10 minutes, the fibrin-affinity probes were injected intravascularly and the animals were subjected to whole body imaging at 1 hour (Figure 2.11). Indeed, we found that different materials prompt various extents of fibrin-affinity probe accumulation in the order: $TiO_2$ > PLA > $SiO_2$ (Figure 2.12). By correlating imaging results with histology measurements, we found a very good relationship between implant-associated fibrin-affinity probe accumulation and localized fibrin deposition

(Figure 2.13). These results confirm that fibrin-affinity probes can be used to quantify implant-mediated fibrin deposition at the implant sites.

To confirm the role of mast cells in implant-mediated fibrin deposition, we used mast cell-deficient (WBB6F1-W/W$^v$) mice and their normal littermates (WBB6F1-+/+). A number of earlier investigations have shown these mice to be a valuable tool for determination of mast cell functions *in vivo* [4, 82]. Interestingly, the fluorescent intensities of different particles in the mast cell-deficient mice, WBB6F1-W/W$^v$ (W/W$^v$), were all dramatically decreased (~ 48% at $TiO_2$, ~ 52% at $SiO_2$, and ~ 44% at PLA) compared to the normal littermates (Figure 2.14). These results demonstrate that mast cell activation is responsible for fibrin deposition at biomaterial implant sites.

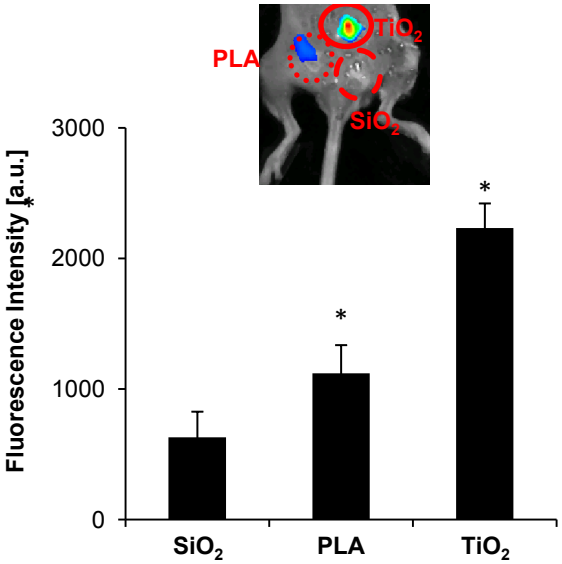


Figure 2.11 In a foreign body response mice model, $TiO_2$, $SiO_2$, and PLA were implanted subcutaneously in the back of animals for 10 minutes prior to fibrin-affinity probe injection. The animal images were taken 1 hour after probe administration. Representative images and quantitative analysis of the fluorescence intensities (bottom) at different implantation sites were quantified and compared. The averages of fluorescent intensities at the implantation sites were quantified. Vertical lines denote ± 1SD (n = 6 in all cases). Significance vs. $SiO_2$ treatment: * $p<0.05$.

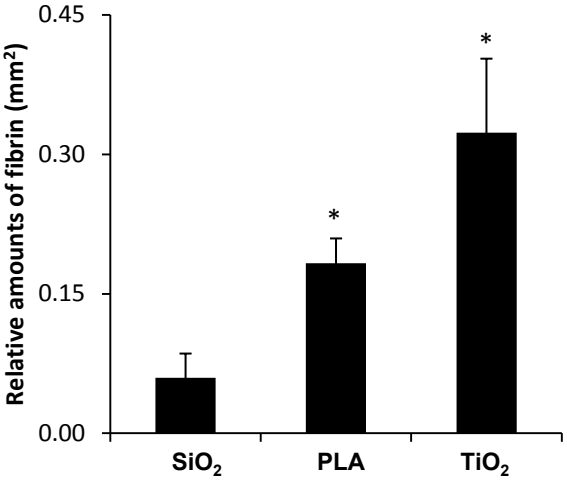


Figure 2.12 The subcutaneous accumulation of fibrin following the $TiO_2$, $SiO_2$, and PLA implants for 2 hours was quantified based on relative stain intensities of the tissue sections using ImageJ software. Vertical lines denote ± 1SD (n = 6 in all cases). Significance vs. $SiO_2$ treatment: * $p<0.05$

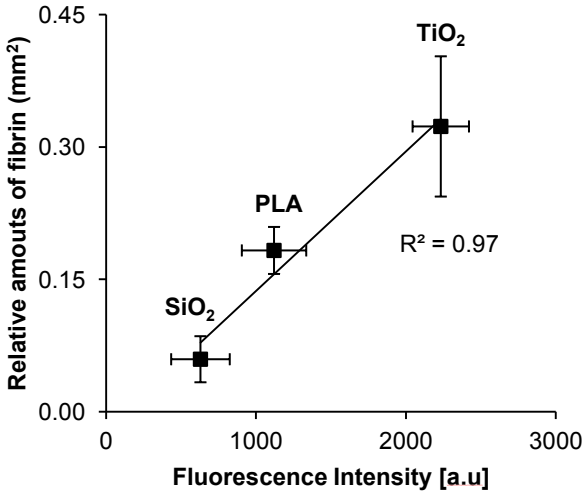


Figure 2.13 Correlation between fibrin-probe associated fluorescence intensity (Figure 2.11) and between relative fibrin accumulation (Figure 2.12) at the implantation sites of $TiO_2$, $SiO_2$, and PLA. Vertical and parallel lines denote ± 1SD. The linear regression has coefficient $R^2$= 0.97 and is statistical significant at $p<0.05$.

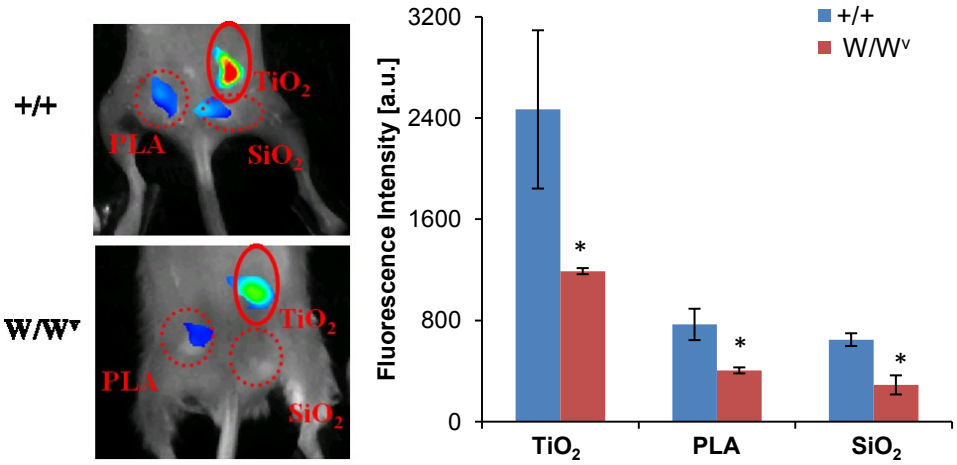


Figure 2.14 In a foreign body response of mast cell-deficiency mice model, $TiO_2$, $SiO_2$, and PLA were implanted subcutaneously in the back of animals for 10 minutes prior to fibrin-affinity probe injection. The animal images were taken 1 hour after probe administration. Representative images and quantitative analysis of the fluorescence intensities at different implantation sites were quantified in both mast cell deficient ($W/W^v$) animals and normal littermates (+/+) animals. Vertical lines denote ± 1SD (n = 3 in all cases). Significance vs. normal littermates animals: * $p<0.05$.

*2.2.4 Discussion and conclusion*

Many imaging probes have been developed by us and others to monitor different cells and processes of foreign body reactions [12, 87, 94, 95]. However, these probes cannot be used for early prediction of foreign body reactions. Since mast cell activation is critical to early fibrin deposition at the inflamed sites [4, 6, 82], and inflammatory cell recruitment to the implanted biomaterials [26, 96], it is likely that the early detection of fibrin deposition at the implant site may predict the extent of subsequent/long-term inflammatory cell recruitment and inflammatory/fibrotic tissue response. This hypothesis is supported by many early observations. Excessive generation of fibrin is always accompanied with the recruitment and activation of inflammatory cells, leading to an increase in the inflammatory response [97-99]. Many studies have documented that extravascular fibrin deposition can be an early and persistent hallmark of inflammatory responses and foreign body reactions [5, 74].

In the present study, GPRPPGGSKGC was selected for fibrin(ogen) targeting based on the following advantages. First, the tri-peptide, Gly-Pro-Arg, has been shown to inhibit the

clotting of fibrin and thrombin because it comprises the N-terminal sequence of the α-chain of fibrin [100]. Another study has identified the peptide Gly-Pro-Arg-Pro-Pro (GPRPP) as a highly avid fibrin-affinity agent possessing increased resistance to proteolysis [101, 102]. In this study, a fibrin-affinity probe was fabricated by conjugating fibrin-affinity peptides (GPRPPGGSKGC) and Oyster800 dye. Oyster-800 dye was chosen because of its biocompatibility and high wavelength (~800 nm) with minimal tissue absorbance and background to improved fluorescence sensitivity for *in vivo* imaging [12, 87, 103]. By directly conjugating the peptide with NIR dye, we substantially reduced the size of our probe less than 1 nm. This makes it a suitable vehicle to detect the accumulation of fibrin *in vivo*, especially since fibrin clots always occur in the injury/inflammation sites which are close to the blood stream [104, 105]. Indeed, our results have shown a substantial accumulation of the fibrin-affinity probe at the implant sites within 10 minutes, achieving a plateau at 1 hour following probe administration and material implantation. Many studies have demonstrated that inactive fibrinogen can convert into fibrin through thrombin injection [86, 106, 107]. Our results support this notion showing increased fibrin-affinity probe accumulation in areas of thrombin-induced fibrin deposition immediately following intravenous injection. Subcutaneous injection of particles such as $TiO_2$ is a well-established inflammation model prompting a foreign body response, accompanied by fibrin deposition [92, 93]. Indeed, immediately following intravenous injection, fibrin-affinity probes accumulated in the area of $TiO_2$-induced inflammation. Additionally, the substantial reduction of probe accumulation in mice treated with an anti-coagulant further supports the fact that this fibrin-affinity probe can target the accumulation of fibrin at the inflamed implant site. Furthermore, the ability of the fibrin-affinity probes to detect and quantify foreign body reactions was tested using different materials. It is well documented that different biomaterial implants can prompt varying inflammatory responses [108]. By implanting various biomaterials ($TiO_2$, $SiO_2$, PLA), it has been confirmed that our fibrin-affinity probes can be used to image and assess the deposition of fibrin

to different particle implants. Interestingly, optical imaging shows that the majority of the probes accumulate inside or in the tissue surrounding particle implants.

Many early studies have shown that mast cells are responsible for fibrin deposition in many inflammatory diseases [4]. Although previous studies have demonstrated that histamine release and mast cell activation are both important to the early-phase foreign-body reaction [5, 82], the role of mast cell activation on fibrin deposition at the biomaterial implant has not been determined yet. Thus, a series of studies were carried out to elucidate mast cell participation on fibrin deposition during foreign body responses. First, by localized activation of mast cells via compound 48/80 administration [82, 109], we found >10 fold increase in fibrin-affinity probe accumulation at the treatment sites in comparison with saline controls. The role of mast cells in implant-mediated fibrin deposition was further tested using mast cell-deficient WBB6F1-W/$W^v$ (W/$W^v$) mice and their normal littermates, WBB6F1-+/+ (+/+). As expected, we found that the accumulation of fibrin-affinity probes at the implant sites were substantially reduced in mast cell-deficient (W/$W^v$) mice (~ 48% at $TiO_2$, ~ 52% at $SiO_2$, and ~ 44% at PLA) in comparison to the normal littermates (+/+). The results indicate that mast cells may play a significant regulatory role in fibrin deposition during biomaterial-induced foreign body responses, which is in agreement with previous findings [82].

# CHAPTER 3

# DEVELOPMENT OF OPTICAL IMAGING TOOLS FOR DETECTING INFLAMMATORY CELL RESPONSE

## 3.1 Introduction

Inflammatory responses are frequently accompanied by an accumulation of phagocytic cells (especially macrophages and neutrophils) [27, 66, 67, 110]. Therefore, real time quantification of macrophages and neutrophils may provide direct assessment of the extent of inflammatory responses at the specific sites.

Neutrophils are the first-responders of inflammatory cells that migrate towards the site of inflammation. Several nuclear imaging probes have been used to diagnose inflammatory lesions using autologous leukocytes labeled with either $^{111}$In or $^{99m}$Tc [111]. Although this approach can yield useful results in specific situations, there are many drawbacks. For example, techniques used for *in vitro* labeling of white blood cells suffer from the disadvantage of lengthy, laborious, and potentially hazardous labeling procedures. In addition, the short life-span of radioactivity prohibits the use of this approach to monitor leukocyte responses over long time periods. In contrast, several recent studies have attempted to develop neutrophil-specific probes using peptides with high affinity for neutrophil surface receptors. Although formyl-methionyl-leucylphenylalanine (fMLP) have been used to image PMN *in vivo* [112, 113], fMLP-based probes have been found to induce neutrophil chemotaxis, adhesion and degranulation [114]. Recent studies have uncovered that the peptide, cFLFLF, has a high affinity for the formyl peptide receptor without significant side effects on neutrophil activities [5, 113-117].

Macrophages are another inflammatory cell type that migrate towards the site of inflammation. A study reported fluorescein isothiocyanate (FITC)-conjugated anti-antibody

F4/80 can be used to image macrophage recruitment [94]. However, these FITC-F4/80 probes produce emission wavelength close to autofluorescence emitted by skin and have limited *in vivo* sensitivities. Moreover, these probes can only provide qualitative, but not quantitative assessment of foreign body reactions [94]. To search for a different macrophages ligand, recent studies have revealed that activated macrophages express high degree of folate receptors [26, 118]. Although folate-targeted probes were found to accumulate in inflamed tissues such as arthritis and atherosclerosis [119, 120], it is not clear whether folate-conjugated probes can be fabricated to detect and quantify the degree of macrophage recruitment at the implant site.

This study will focus on the evaluation of newly fabricated optical imaging probes for detecting and quantifying the recruitment of neutrophils and macrophages to reflect the extent of the foreign body response.

## 3.2 Investigation of a formyl peptide receptor-targeting NIR probe for neutrophil detection

### *3.2.1 Purpose*

A series of studies were carried out to assess the effect of formyl peptide receptor-targeting probes for detecting neutrophil recruitment both *in vitro* and *in vivo*. First, we investigate the efficacy of formyl peptide receptor-targeting probes to recognize activated neutrophils *in vitro*. Using an *in vivo* imaging system, the effectiveness of formyl peptide receptor-targeting probes in quantifying the extent of biomaterial implant-mediated neutrophil recruitment was also assessed. Finally, formyl peptide receptor-targeting probes were tested for their ability to continuously monitor and quantify the extent of the inflammatory response to different biomaterial implants and infected catheters *in vivo*.

### *3.2.2 Materials and methods*

#### 3.2.2.1 Materials

The formyl peptide receptor-targeting probe was fabricated based on published procedures [12]. Briefly, PEG-O800 (eight-arm PEG-amine (20 mg/1.0 ml) with Oyster-800 (2.0 mg/1.0 ml)) was used for the fabrication of formyl peptide receptor-targeting probes. The probes

were fabricated by coupling the peptide cFLFLF (8.3 mg) with PEG-O800. The activated peptide solution was mixed with eight-arm PEG-Oyster-800 solution (peptide: eight-arm PEG-Oyster-800 = 27:1 molar ratio). The illustration of formyl peptide receptor-targeting probes is shown in Figure 3.1. The optical property of the formyl peptide receptor-targeting probe (cFLFLF-PEG-Oyster-800, 1.0 mg/ml) was measured using a fluorescence spectrometer (RF-5301PC; Shimadzu Corporation, Tokyo, Japan). The peptide to dye conjugation ratio was determined using an ultravioletvisible spectrometer (Lambda 19 Spectrometer; PerkinElmer, Waltham, MA) according to the manufacturer's instruction and a previous publication [121]. The cell toxicity assay will be tested using 3T3 fibroblasts as published in an earlier protocol [85].

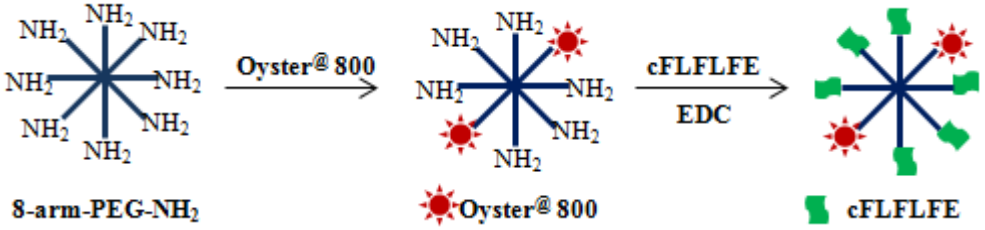


Figure 3.1 Schematic illustration of formyl peptide receptor-targeting.

3.2.2.2 *In vitro* analyses of cell binding affinity of formyl peptide receptor-targeting probes

To assess the ability of the formyl peptide receptor-targeting probe to detect activated neutrophils, activated mouse neutrophils ($9 \times 10^6$ cells/ml) isolated *via* peritoneal lavage from Balb/c mice were used, as described previously [66, 122]. Various numbers of neutrophils were seeded into each well of a 96-well plate prior to incubating with either the formyl peptide receptor-targeting probe or its control (PEG-Oyster-800) (40 µl at 0.4 mg/ml) at 37°C for 30 minutes. At the end of the study, each well was washed three times with phosphate buffered saline (50 mM, pH 7.4) to remove the unbound probes. Neutrophil-associated fluorescence intensities were then recorded using a microplate reader (InfiniteR M200; Tecan Group Ltd, Mannedorf, Switzerland) at an excitation wavelength of 760 nm and an emission wavelength of 830 nm (n = 3). Similar studies were also carried out on glass slides for microscopic optical

imaging. Following probe incubation, the adherent cells on glass slides were also incubated with the FITC-conjugated anti-neutrophil antibody (ab2557; Abcam, Cambridge, MA) at 37°C for 30 minutes prior to being washed three times with phosphate buffered saline. The adherent cells were then observed under an AxiovertR 200 microscope (Carl Zeiss MicroImaging, Thornwood, NY) with a Chroma Cy7™ filter cube (excitation filter HQ710/75×, dichroic Q750LP BS, and emission filter HQ810/90 m; Chroma Technology Corporation, Bellows Falls, VT) and a Zeiss filter set 10 (excitation filter BP 450-490, dichroic mirror FT 510, and emission filter BP 515–565; Carl Zeiss). Cell images were captured with a CCD camera (AxioCam MRm), and image analysis was performed with AxioVision R 3.1 imaging software (Carl Zeiss).

3.2.2.3 *In vivo* Inflammation and infection animal model

To induce localized inflammatory responses, LPS (100 μg/50 μl in saline) or saline (as control) was injected subcutaneously on the dorsal area of mice (n = 6). PLA microparticles (5-10 μm in diameter, 100 ml, 10% w/v) and PEG nanoparticles (100 nm in diameter, 100 ml, 10% w/v) were used to trigger various extents of foreign body reactions (n = 5). Another 100 μl of the particles or saline (as control) were injected into the subcutaneous space. Limited experiments were also carried out using neutrophil-depleted mice. Neutrophil depletion was performed based on a published protocol (n = 6) [123]. In brief, animals were injected intraperitoneally with 100 μl of neutrophil neutralizing antibody (rabbit anti-mouse neutrophil antibody; Accurate Chemical and Scientific Corporation, Westbury, NY) at 18 hours and additionally at 1 hour prior to the experiments. To study catheter-associated inflammatory responses and infection, PU catheters (1 cm in length) obtained from Sentry Medical Products (Green Bay, WI) were incubated with saline or luciferase-transgene *Staphylococcus aureus* Xen29 strain ($1.6 \times 10^8$ colony-forming units/ml; Caliper Life Sciences, Hopkinton, MA) at 37°C for 3 hours and then implanted subcutaneously in mice following an established protocol (n = 6) [124, 125]. After the implantation of particles, saline, or catheters for 24 hours, animals were intravenously administered with 60 μl of the formyl peptide receptor-targeting probe (0.4 mg/ml) 3 hours prior

to imaging analyses. Imaging analyses was then carried out on whole body and harvested organs. Whole body images of mice were taken using KODAK In vivo FX Pro (f-stop: 2.5, excitation filter: 760 nm, emissions filter: 830 nm, 4 × 4 binning; Carestream Health, Rochester, NY) and fluorescence intensities were calculated using Carestream Molecular Imaging Software, Network Edition 4.5 (Carestream Health). To assess the biodistribution of formyl peptide receptor-targeting probe in vivo, animals were sacrificed and tissues were rapidly dissected (n = 4). The isolated organs/tissues were then immediately imaged using the In Vivo FX Pro system.

3.2.2.4 Histological analysis of localized inflammatory responses

To assess the extent of neutrophil responses in various models, the implants and surrounding tissue were isolated for histological evaluation as described earlier [27, 126]. Hematoxylin and eosin staining was performed on all samples to assess the overall inflammatory reactions. To quantify the number of recruited neutrophils, some tissue sections were immunohistochemically stained with pan-neutrophil antibody (Santa Cruz Biotechnology, Santa Cruz, CA) and then with peroxidase-conjugated goat anti-rat secondary antibodies (Jackson ImmunoResearch Laboratories, West Grove, PA). All histological imaging analyses were performed on a Leica microscope (Leica Microsystems GmbH, Wetzlar, Germany) and processed using NIH ImageJ (National Institutes of Health, Bethesda, MD) [27]. To visualize the distribution of the formyl peptide receptor-targeting probe in inflamed tissues, fresh tissue sections were also imaged using an Axiovert 200 microscope with an NIR filter cube as FR-targeting probes [12].

3.2.2.5 Data Analyses

Neutrophil-associated fluorescence intensities were measured using a Tecan Infinite M 200 plate reader (San Jose, CA) at emission of 830nm (excitation at 760 nm). The fluorescence intensities of whole body imaging were calculated using Carestream Molecular Imaging Software, Network Edition 4.5 (Carestream Health). In brief, regions of interests (ROIs) were

drawn over the implantation locations after background correction, and the mean fluorescence intensities for all pixels in the fluorescent images. Quantitative histological analysis (H&E) of the total number of inflammatory cells and IHC analysis of the number of recruited neutrophils throughout the implantation sites were performed using NIH ImageJ (National Institutes of Health, Bethesda, MD) [12, 87, 88].

3.2.6 Statistical analyses

The statistical comparison between different treatment groups was carried out using Student's *t*-test. Differences were considered statistically significant when $p < 0.05$. Linear regression analyses and the correlation coefficient ($R^2$) were calculated to reflect the relationship between fluorescence intensities and neutrophil numbers *in vitro* and *in vivo*.

*3.2.3 Results*

3.2.3.1 Characterization of the formyl peptide receptor-targeting probe

Ultraviolet-visible spectrometer measurements show that, unlike the control probes, formyl peptide receptor-targeting probes have an absorbance peak at 280 nm, identical to the peak absorbance wavelength of the peptide (Figure 3.2a). These results demonstrate the successful conjugation of peptide ligands to formyl peptide receptor-targeting probes. On average, each mole of probe was found to contain 1.8 moles of dye and 6.0 moles of peptide. Furthermore, fluorescence spectroscopy demonstrated that the conjugation of NIR dye did not significantly alter the fluorescence spectra of free Oyster-800 dye with a maximum emission at 799 nm and excitation at 785 nm (Figure 3.2b). The cytotoxicity of the formyl peptide receptor-targeting probes was determined using 3T3 fibroblasts and MTS assay (Figure 3.3). We find that the formyl peptide receptor-targeting probes trigger no statistically significant cytotoxicity over the studied concentration range (0.012 – 0.2 mg/ml), which means that these probes possess adequate cell compatibility for further *in vivo* testing.

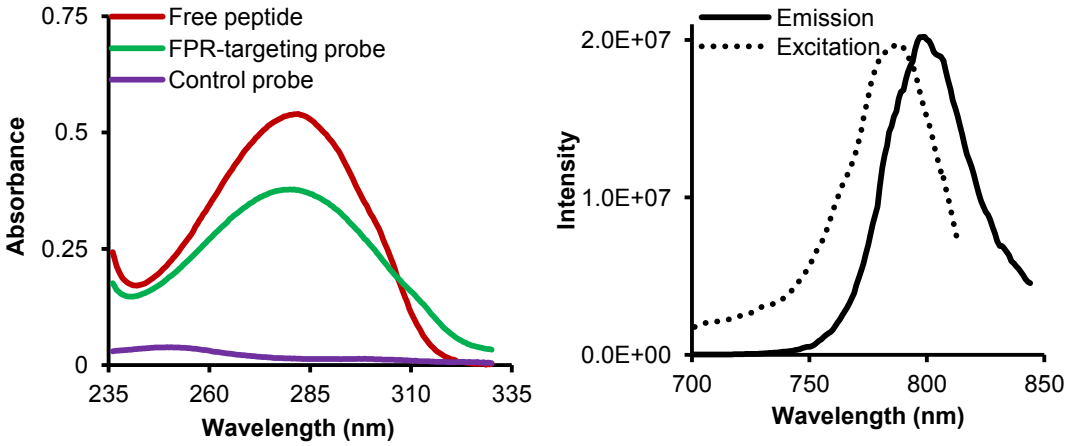


(a) (b)

Figure 3.2 Characterization of the optical property of formyl peptide receptor-targeting probes. (a) Absorbance measurements of peptides, formyl peptide receptor-targeting probes (FPR, formyl peptide receptor), and control probes were determined based on Ultraviolet-visible spectrometer. (b) Excitation and emission spectra of formyl peptide receptor-targeting probes were measured based on fluorescence spectrum.

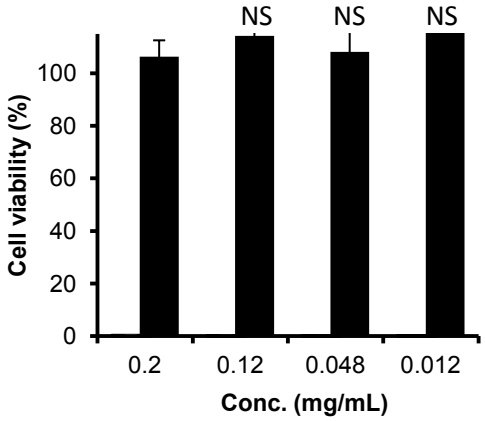


Figure 3.3 Cytotoxicity study of formyl peptide receptor-targeting probe (0.012-0.2 mg/ml) was carried out using 3T3 fibroblasts and MTS assay. Vertical lines denote ± 1SD (n= 5 in all cases). Significance vs. no treatment: NS – no statistical significance.

We therefore assessed whether formyl peptide receptor-targeting probes recognize activated neutrophils *in vitro*. To examine their ability to recognize activated neutrophils *in vitro*, formyl peptide receptor-targeting probes (cFLFLF-PEG-Oyster-800) or control probes (PEG-Oyster-800) were incubated with mouse neutrophils. The cells were also stained with a rat anti mouse monoclonal neutrophil antibody and a fluorescein isothiocyanate-conjugated goat anti-rat secondary antibody for neutrophil confirmation. The cells were then observed using an

optical microscope. As anticipated, it was found that only activated neutrophils (stained with the antibody, green color) were associated with the formyl peptide receptor-targeting probe (red color) (Figure 3.4). This finding supports the hypothesis that formyl peptide receptor-targeting probes may be used to specifically identify activated neutrophils. To further study whether the probes can be used to quantify the number of activated neutrophils *in vitro*, various concentrations of neutrophils were incubated with the probes and the neutrophil-associated fluorescence intensities were determined. In support of the hypothesis, it was found that there was a linear correlation between the fluorescence intensity and the number of neutrophils (Figure 3.5).

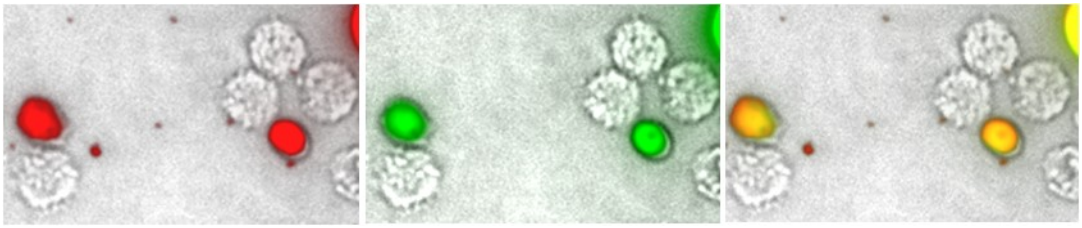

Figure 3.4 Investigation of the specificity of the formyl peptide receptor-targeting probes to target activated neutrophils (FPR, formyl peptide receptor) incubation *in vitro*. Fluorescence microscopy images of activated neutrophils incubated with formyl peptide receptor-targeting probe (left) and neutrophil-specific antibody (middle) and their superimposed image (right).

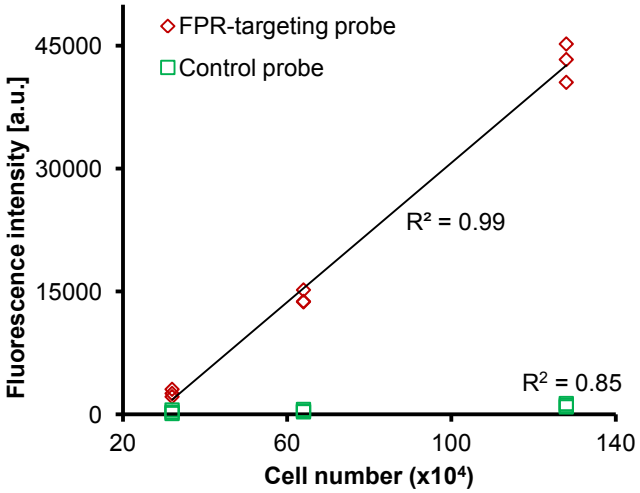


Figure 3.5 Correlation between neutrophil numbers and neutrophil-associated fluorescence intensities following incubation with either formyl peptide receptor-targeting probe or control probe for *in vitro* study. The linear regression has coefficient $R^2$= 0.92 in the group of formyl peptide receptor-targeting probe and $R^2$= 0.85 in the control probe. (FPR: formyl peptide receptor)

In contrast, the fluorescence intensity of neutrophils incubated with the control probes (PEG-Oyster-800) remained close to the background intensity regardless of the cell number. Overall, the *in vitro* results support that formyl peptide receptor-targeting probes can preferentially bind to neutrophils and may be used to quantify the number of neutrophils *in vitro*.

3.2.3.2 Detection of LPS-induced localized neutrophil responses using formyl peptide receptor-targeting probes

The effectiveness of formyl peptide receptor-targeting probes for detecting neutrophil accumulation in inflamed tissue was first tested *in vivo* using a LPS-induced inflammatory response model. After LPS subcutaneous administration for 24 hours, the formyl peptide receptor-targeting probe was injected intravenously and whole body images were recorded at different time points (Figure 3.6). A substantial increase in fluorescence intensity was found at the LPS injection site, in as short as 30 minutes following probe injection, in comparison to the control. The preferential accumulation of the formyl peptide receptor-targeting probe at the LPS site increased with time and reached a plateau at 2–3 hours, where the LPS treatment triggered 8.6 times higher fluorescence intensity than the control. To determine the biodistribution of the probes, the fluorescence images of the isolated organs or tissues were recorded and used to quantify the organ/tissue-associated fluorescence intensities (Figure 3.7). As anticipated, large quantities of the formyl peptide receptor-targeting probe were found in the liver and kidney. A substantial amount of fluorescence from the probes was also found in the lung, heart, and pancreas. In agreement with the whole body imaging results, it was found that the average fluorescence intensity at the LPS injection site was 4.5 times higher than the control tissues (saline injection) (Figure 3.7). Based on the *in vitro* results, we believe that the accumulation of formyl peptide receptor-targeting probes at the LPS injection site is likely associated with the accumulation of neutrophils in the tissue.

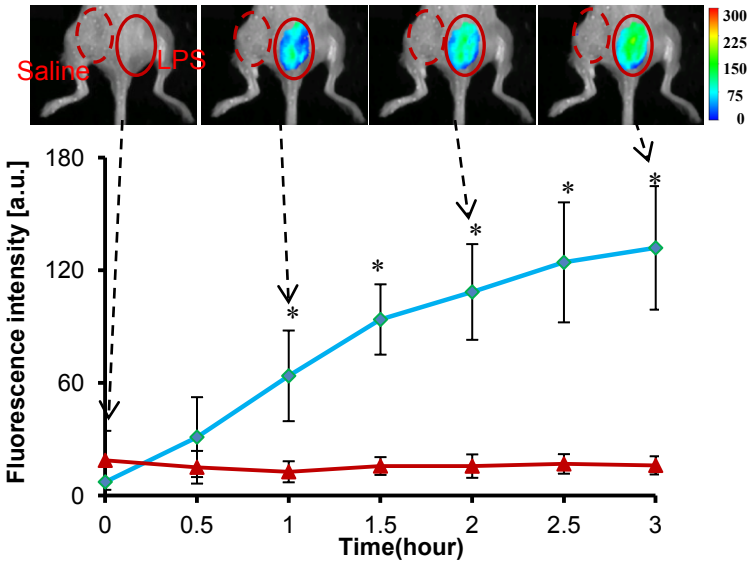


Figure 3.6 In the LPS-induced severe inflammation model, the formyl peptide receptor-targeting probe was administered intravenously 24 hours after a LPS subcutaneous injection. The representative merged fluorescence and white light image shows the accumulation of formyl peptide receptor-targeting at different injection sites, LPS and saline, and the averages of fluorescent intensities at the implantation sites were also quantified and compared. Vertical lines denote ± 1SD (n = 6 in all cases). Significance vs. saline treatment: * $p < 0.05$.

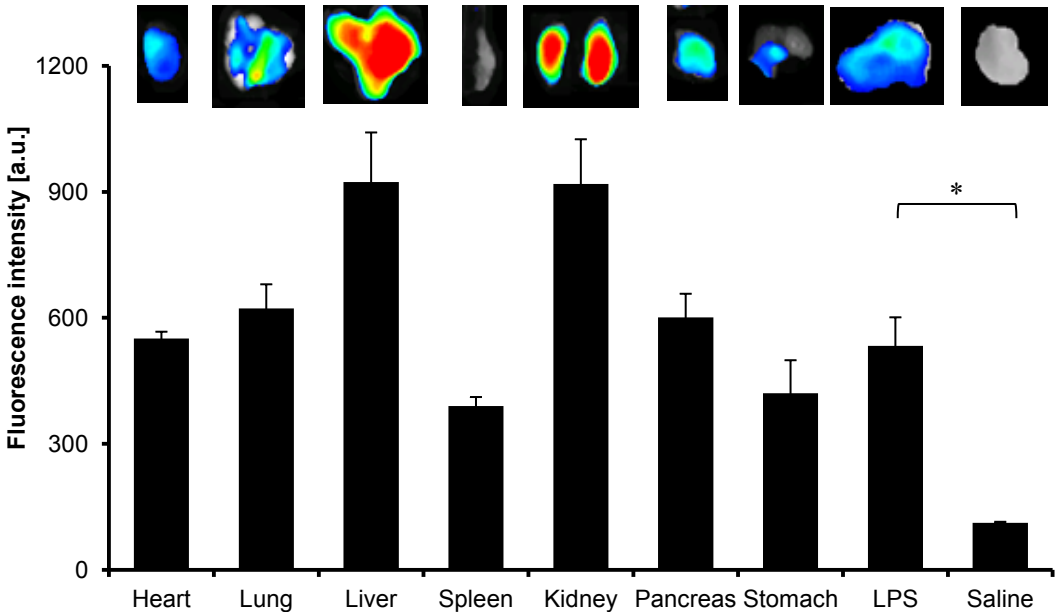


Figure 3.7 *Ex vivo* image and the average fluorescence intensity of isolated tissues and organs from LPS-induced severe inflammation model show the overall probe biodistribution and also confirm the preferential accumulation of formyl peptide receptor-targeting probes in the inflamed tissue. Vertical lines denote ± 1SD (n = 4 in all cases). Significance vs. saline treatment: * $p < 0.05$.

Indeed, using H&E staining and immuno-histochemical staining, it was found that LPS injection triggered an increase in inflammatory cells (10 times higher) and neutrophils (90 times higher) in comparison with the control tissue (Figure 3.8).

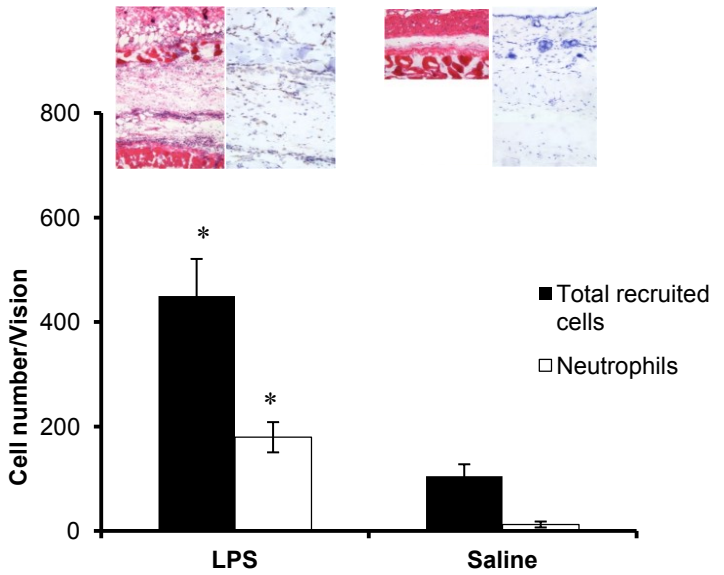


Figure 3.8 The subcutaneous recruitment of inflammatory cells and of inflammatory cells and neutrophils from LPS-induced severe inflammation model for 24 hours. Representative H&E (200×) and IHC neutrophil staining (400×) of LPS and saline sites and quantification of inflammatory cells and neutrophils were quantified based on the H&E stained and IHC stained slices, respectively. The cells counts per view field were quantified by ImageJ. Vertical lines denote ± 1SD (n = 6 in all cases). Significance vs. saline treatment: * $p < 0.05$.

3.2.3.3 Use of formyl peptide receptor-targeting probes to assess neutrophil accumulation at biomaterial implant sites

The results thus far support that the formyl peptide receptor-targeting probes can detect LPS-elicited severe inflammatory responses. It is not clear, however, whether the formyl peptide receptor-targeting probes can also determine mild or localized inflammatory responses, such as foreign body reactions and associated neutrophil reactions. To find the answer, mice were subcutaneously implanted with PLA microparticles for 24 hours to trigger foreign body reactions. The animals were subsequently administered intravenously with the formyl peptide receptor-targeting probes. As expected, PLA particle implantation triggered foreign body reactions which

were accompanied by a large number of inflammatory cells, including neutrophils (Figure 3.9a). The recruited neutrophils most likely play an essential role in the pathogenesis of the foreign body reactions. This is clearly observed through neutrophil depletion studies which show a substantial reduction in the extent of inflammatory cell (~50%) and neutrophil (~75%) recruitment to PLA implant sites when compared with normal mice (Figure 3.9b). To validate that the probe accumulation is primarily due to the infiltration of neutrophils, both normal and neutrophil depleted animals were subcutaneously implanted with PLA particles and then intravenously administered with the formyl peptide receptor-targeting probes. As expected, neutrophil depletion resulted in decreased fluorescence intensity from the PLA implant site at 1 hour (~100% intensity reduction) and 4 hours (82% intensity reduction) in comparison to the normal animals (Figure 3.10). These findings demonstrate the high efficiency of formyl peptide receptor-targeting probes in recognizing and targeting activated neutrophils at the inflamed sites. Furthermore, our results support that formyl peptide receptor-targeting probes can be used to detect implant-associated neutrophil accumulation.

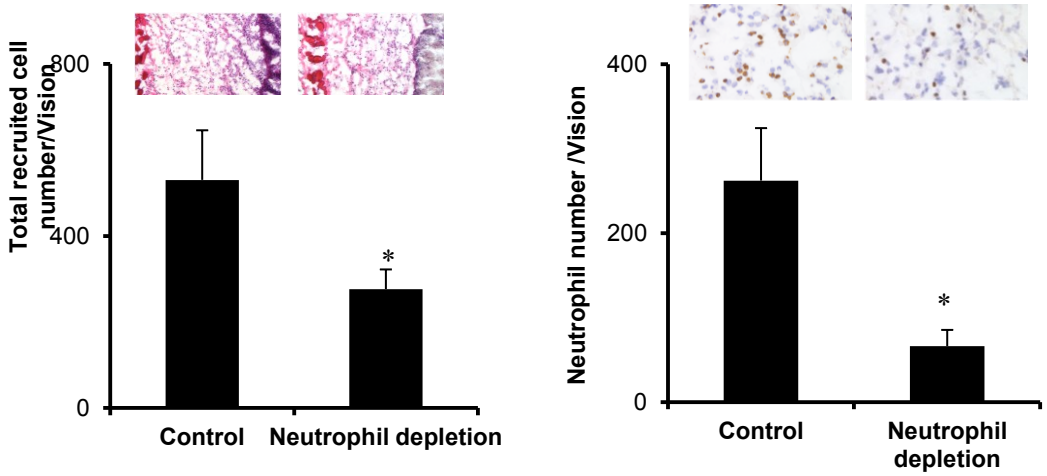


(a) (b)

Figure 3.9 The effect of neutrophil depletion in a foreign body response model. PLA particles were implanted in neutrophil-depleted versus control mice for 24 hours. (a) Representative H&E (200×) and quantification of inflammatory cell numbers at PLA implant sites either control or neutrophil depletion mice were quantified and compared. (b) Representative IHC (600×) and quantification of neutrophils numbers at PLA implant sites either control or neutrophil depletion mice. The cells counts per view field were quantified by ImageJ. Vertical lines denote ± 1SD (n = 6 in all cases). Significance vs. saline treatment: * $p < 0.05$.

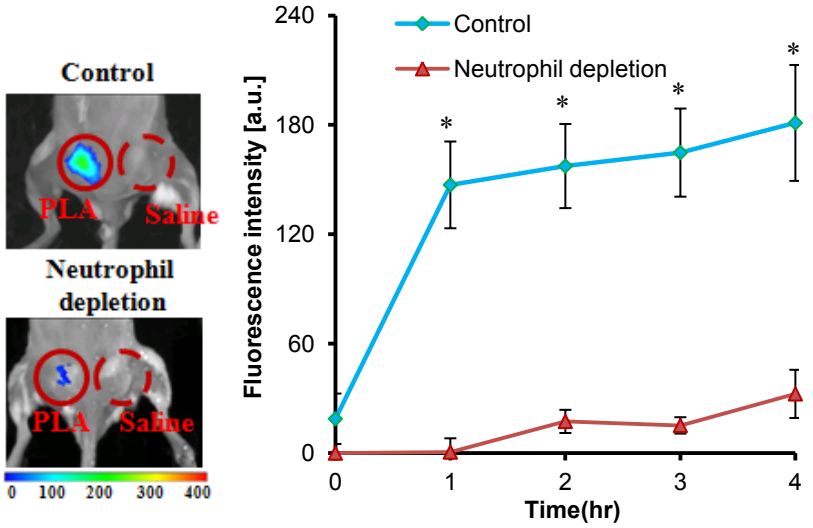


(a) (b)

Figure 3.10 The effect of neutrophil depletion in a foreign body response model. PLA particles were implanted in neutrophil-depleted versus control mice for 24 hours prior to formyl peptide receptor-targeting probe administration. (a) The merged fluorescence and white light images at 4 hours post injection of formyl peptide receptor-targeting probe. (b) Fluorescence intensities at different time points at different time (0-4 hours post injection). The mean fluorescence intensities at PLA and saline sites were quantified. The results illustrate the diminishing accumulation of formyl peptide receptor-targeting probes in neutrophil depleted animals in comparison with controls. Vertical lines denote ± 1SD (n = 6 in all cases). Significance vs. saline treatment: * $p < 0.05$.

3.2.3.4 Quantify the degree of foreign body reactions using formyl peptide receptor-targeting probes

It is well established that biomaterial implants trigger various extents of neutrophil responses. Additionally, there is a good relationship between neutrophil recruitment and the biomaterial-mediated acute inflammatory response [5, 66]. It may therefore be possible to use formyl peptide receptor-targeting probes to assess the extent of foreign body reactions and biomaterial tissue compatibility. To test this hypothesis, PLA and PEG particles were selected as model biomaterials. Previous studies have shown that PLA and PEG particles prompt mild and weak inflammatory responses, respectively [87, 127]. The particles were subcutaneously implanted in mice, with saline as a control, for 24 hours prior to administration of the imaging probe. Three hours after injection of the probe, whole body imaging was performed. The results show that the fluorescence signal at the PLA and PEG particle implant sites were much higher

than at the control saline site (Figure 3.11). Quantitative analysis shows that PLA and PEG particles trigger 9.5 X and 2.8X higher fluorescence intensity than the control, respectively. To determine the distribution of the probes within the implantation sites, tissue sections of the implants and surrounding tissues were observed under a fluorescence microscope (Figure 3.12). It was found that a high probe concentration was present in tissue near the PLA implants; while significantly lower amounts were detected surrounding the PEG implants.

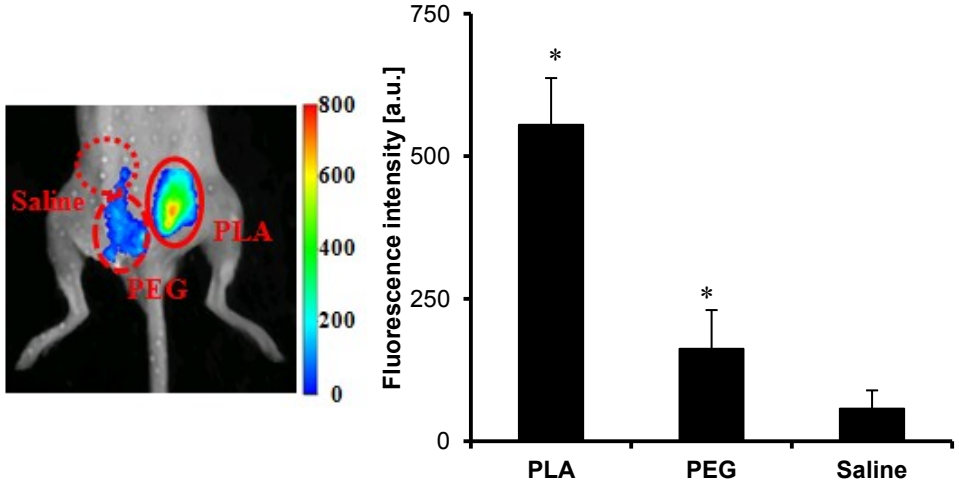


Figure 3.11 In a foreign body response mice model, PLA, PEG, and saline were implanted subcutaneously in the back of animals for 24 hours prior to formyl peptide receptor-targeting probe injection. The animal images were taken 3 hours after probe administration. Representative images and quantitative analysis of the fluorescence intensities at different implantation sites were quantified and compared. The averages of fluorescent intensities at the implantation sites were quantified. Vertical lines denote ± 1SD (n = 6 in all cases). Significance vs. saline treatment: * $p<0.05$

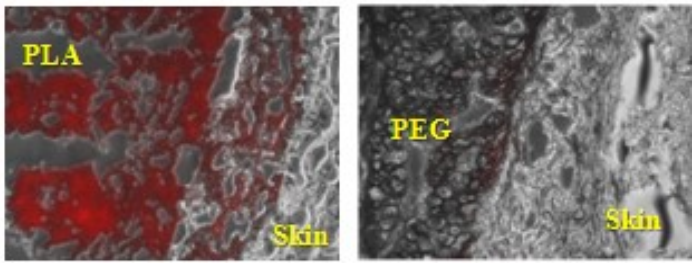


Figure 3.12 In a foreign body response mice model, PLA, PEG, and saline were implanted subcutaneously in the back of animals for 24 hours. Near-infrared fluorescence acquisition under fluorescence microscope (red) superimposed onto the correlative phase contrast microscopic image (20×) at PLA, PEG implants. The tissue section was unstained and unfixed to preserve the fluorescence signal.

Histological analysis shows that PLA particles prompt a greater extent of neutrophil accumulation at the implant site than PEG implants, while negligible numbers of neutrophils populated the control site (Figure 3.13a). Quantitative analysis revealed that 2.5 folds more neutrophils accumulated around the PLA particles than the PEG particles (Figure 3.13b).

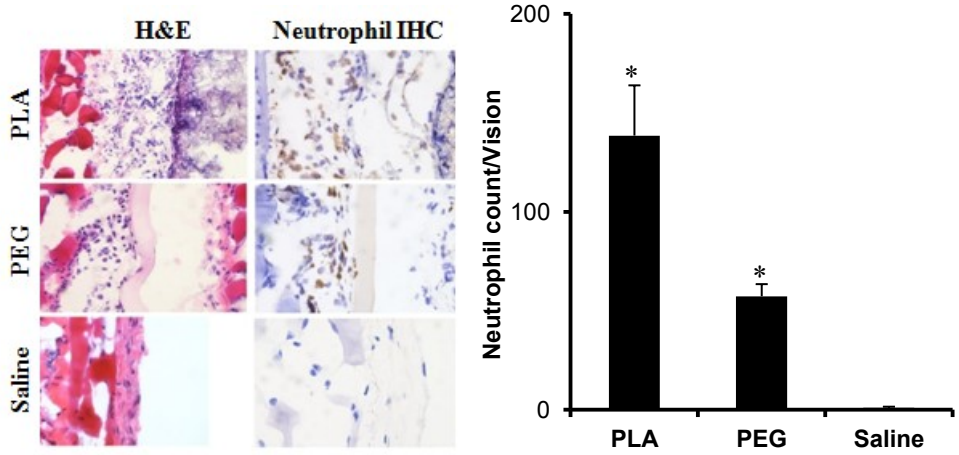


(a) (b)

Figure 3.13 In a foreign body response mice model, PLA, PEG, and saline were implanted subcutaneously in the back of animals for 24 hours. (a) Representative H&E (400x) and IHC (600×) stained slices and (b) quantification of neutrophils numbers at different implant sites were quantified and compared. The cells counts per view field were quantified by ImageJ. Vertical lines denote ± 1SD (n = 6 in all cases). Significance vs. saline treatment: * $p < 0.05$.

A comparison and correlation between fluorescence intensity and neutrophil counts was further performed to determine a potential relationship between the probe accumulation and implant-mediated neutrophil responses. The results show a near linear trend (correlation coefficient = 0.89) (Figure 3.14). These findings confirm that formyl peptide receptor-targeting probes can be employed as an effective imaging probe not only to mark the inflammation location but also to estimate the extent of biomaterial-mediated neutrophil recruitment and inflammatory responses *in vivo*.

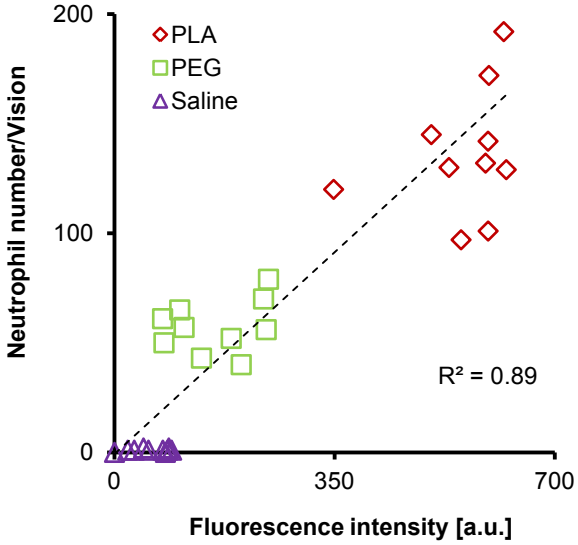


Figure 3.14 Correlation between formyl peptide receptor-associated fluorescence intensities (Figure 3.12) and recruited neutrophil numbers (Figure 3.13) at different implant sites of PLA, PEG, or saline. The linear regression has coefficient $R^2 = 0.89$.

3.2.3.5 Detection of infected catheters by means of formyl peptide receptor-targeting probes

Given the ability of the formyl peptide receptor-targeting probe to preferentially target neutrophils associated with particle implants *in vivo*, it was further investigated whether the probe could be used to detect inflammatory responses elicited by bacteria-colonized medical devices. For that, PU catheters were used as a model medical device. Some of the PU catheters were inoculated with the luciferase transgenic *S. aureus* for 24 hours prior to subcutaneous implantation. The formyl peptide receptor-targeting probes were then intravenously administered and images were captured 3 hours after the probe injection. Strong bioluminescent signals from the infected catheters were found, but not from the control catheters, demonstrating the colonization of bacteria on PU catheters *in vivo* (Figure 3.15a). In addition, bright fluorescence signals were found at the area of the infected catheters. Analysis and quantification of the fluorescence signal shows an 8.8 fold higher probe accumulation near the infected catheters versus the controls (Figure 3.15b). Further analysis was performed on tissue sections confirming a substantial increase in probe concentration in tissue surrounding

the infected PU catheter in comparison to the controls (sterile PU catheter implants) (Figure 3.16). Furthermore, histological analysis confirmed that the neutrophil population surrounding the infected tissue was 7.3X higher than the tissue surrounding the control PU catheters (Figure 3.17). These results suggest that formyl peptide receptor-targeting probes can be used to monitor neutrophil responses to catheter implants. In addition, the probe is able to distinguish infected catheters versus sterile catheters, based on the extent of neutrophil responses.

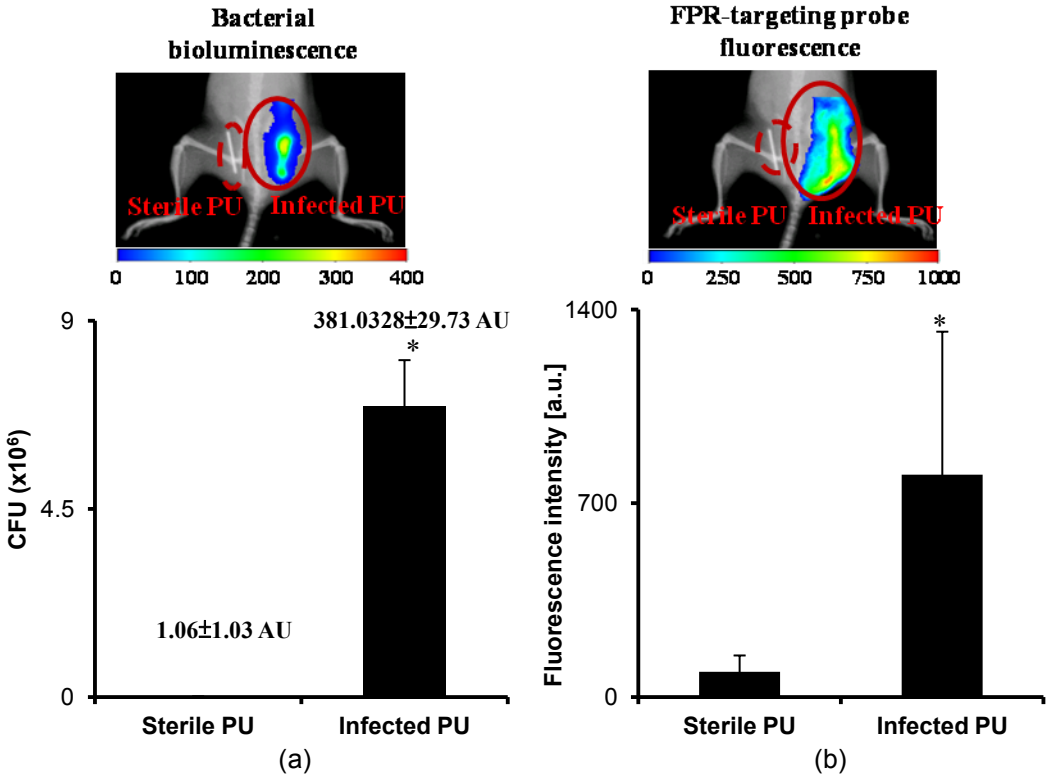


Figure 3.15 In an infected catheter inflammation model, PU catheters were colonized with luciferase transgene *Staphylococcus aureus* and then transplanted subcutaneously on the back of animals for 24 hours. The animals were then administered with formyl peptide receptor-targeting probes for 3 hours prior to imaging analyses. (a) Representative bioluminescence image and the average estimated bacterial colony-forming unit counts were quantified to depict bacterial colonization on implanted catheters. (b) Fluorescence image and quantification of average formyl peptide receptor-associated fluorescence intensities at the implantation sites of catheters were quantified. The results showed more accumulation of formyl peptide receptor-associated fluorescence intensities in the infected PU catheter implant site than sterile PU caheter. Vertical lines denote ± 1SD (n = 6 in all cases). Significance vs. sterile PU: * $p<0.05$

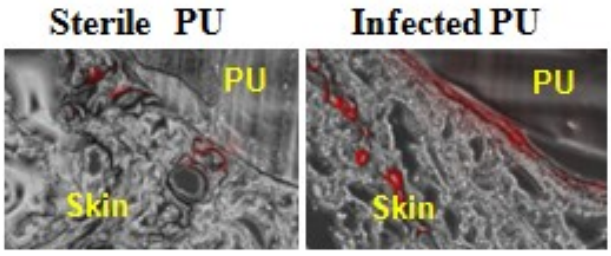


Figure 3.16 In an infected catheter inflammation model, PU catheters were colonized with luciferase transgene *Staphylococcus aureus* and then transplanted subcutaneously on the back of animals for 24 hours. NIR fluorescence acquisition under fluorescence microscope (red color) superimposed onto the correlative phase contrast microscopy image (20×) for tissues surrounding the PU catheters. The tissue section was unstained and unfixed to preserve the fluorescence signal.

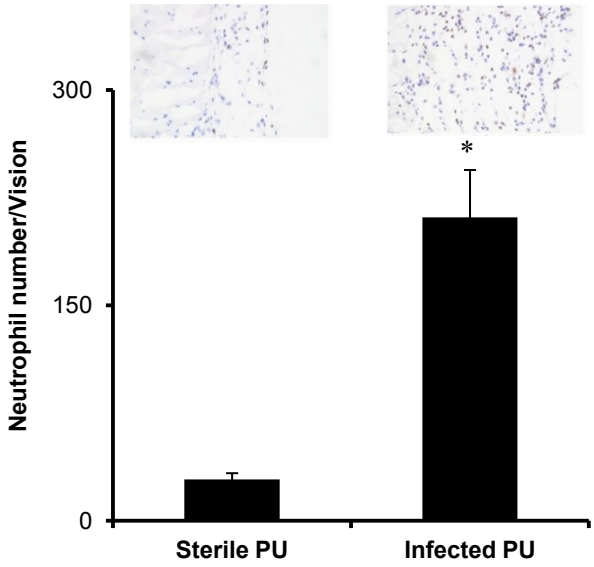


Figure 3.17 In an infected catheter inflammation model, PU catheters were colonized with luciferase transgene *Staphylococcus aureus* and then transplanted subcutaneously on the back of animals for 24 hours. Representative IHC staining of neutrophils (400×) and of neutrophils numbers at different implant sites were quantified and compared. The cells counts per view field were quantified by ImageJ. The neutrophil cell counts support the conclusion that substantially higher numbers of neutrophils were recruited to the infected polyurethane catheters than sterile ones. Vertical lines denote ± 1SD (n = 6 in all cases). Significance vs. saline treatment: ** $p < 0.05$.

*3.2.4 Discussion and Conclusion*

For the development of imaging probes in monitoring foreign body reactions, the peptide, cFLFLF, was selected as a targeting ligand based on the following advantages. First, several recent studies have shown that cFLFLF has a high binding affinity to the neutrophils' formyl peptide receptor [128, 129]. In addition, the cFLFLF peptide possesses antagonistic

properties and does not induce neutropenia as do other high-affinity chemotactic peptide analogs, such as formyl-methionyl-leucylphenylalanine (FMLF) peptide [128, 129]. In the present study, a formyl peptide receptor-targeting (cFLFLF-conjugated) probe was fabricated using an eight-arm PEG core as a multifunctional platform. The use of the eight-arm PEG core chosen in this study is due to the following reasons. First, the multifunctional platform allows us to optimize peptide density in a single probe, thus enhancing its targeting efficiency [121, 130]. Second, the modification of peptide by PEGylation may enhance probe hydrophilicity, reduce nonspecific binding, and thus improve bioavailability and clearance when used *in vivo* [131, 132]. For *in vivo* imaging, Oyster-800 dye was chosen for its biocompatibility and high wavelength (~800 nm) which has minimal tissue absorbance and background with improved fluorescent sensitivity [31, 103].

Our *in vitro* experiments demonstrate that the formyl peptide receptor-targeting probe can specifically bind to neutrophils with a high affinity. These observations are in line with the results reported for microscopy studies of other fluorescently labeled chemotactic peptides [129, 133-135]. The obtained linear correlation between the fluorescence intensity and the neutrophil number *in vitro* indicates that this probe has a high potential for quantitative assessment of neutrophils *in vivo* [87].

Subcutaneous injection of LPS is a well-established inflammation model prompting severe inflammatory responses, accompanied by the recruitment of neutrophils, macrophages and other immune cells [136, 137]. Indeed, immediately following intravenous injection, formyl peptide receptor-targeting probes accumulate in the area of LPS-induced inflamed tissue which is consistent with a previous finding using PMA to induced acute inflammation [128]. In addition, the substantial reduction of probe accumulation in neutrophil-depleted mice further supports the notion that the formyl peptide receptor-targeting probe is tightly associated with the recruitment of neutrophils. In addition, our results show that formyl peptide receptor-targeting probes can be used to detect mild inflammatory responses, such as foreign body reactions.

The mechanism of formyl peptide receptor-targeting probe accumulation at the inflamed tissue is not entirely understood. Our results suggest that the buildup of the formyl peptide receptor-targeting probe was likely caused by their interactions with formyl peptide receptor on the surfaces of activated neutrophils. This is supported by our observations that fluorescent intensities at the implant sites reduced ~72% following neutrophil depletion. The residual fluorescent intensities at the implantation sites of neutrophil-depleted animals may be caused by the following reasons. First, neutrophil depletion can only reduce ~80% of neutrophils from the circulation [138] and a small number of residual neutrophils was found to accumulate at the implant sites. Second, it is well established that biomaterial implants prompt histaminic reactions [81, 82]. The leakage blood vessel, or the "enhanced permeability and retention" effect, may permit the permeation of small amounts of the imaging probes to the tissue surrounding implants [87, 139].

The ability of the formyl peptide receptor-targeting probe to detect and quantify foreign body reactions was tested using different material subjects. By implanting different material particles, our studies have confirmed that the formyl peptide receptor-targeting probe can be used to image and assess the extent of neutrophil responses to different particle implants. Interestingly, optical images support that the majority of the probes accumulate inside or surrounding particle implants. Equally important, there is a good relationship between the extent of formyl peptide receptor-targeting probe signals and the number of recruited neutrophils at the implant sites. These results demonstrate that the formyl peptide receptor-targeting probes can be used not only to detect the severe inflammation sites as reported earlier [113, 129], but also to estimate the extent of the inflammatory responses to biomaterials. Using an infected catheter implantation model, we find that the bacterial-infected catheters significantly enhance formyl peptide receptor-targeting probe localized accumulation compared to the controls. Coincidentally, a large numbers of neutrophils are found nearby the catheter surfaces which are in agreement with previous findings [140]. The overall data support that the formyl peptide

receptor -targeting probe can be used to detect neutrophil responses in the event of foreign body reactions and device-centered infection in real time *in vivo*.

This study demonstrates that formyl peptide receptor-targeting probes can be fabricated to specifically detect activated neutrophils. Since neutrophils represent a major subset of inflammatory cells, and neutrophil responses play an important role in acute inflammatory responses, we anticipate formyl peptide receptor-targeting probes can be used as a powerful tool to provide a highly sensitive and reliable assessment of neutrophil reactions and associated inflammatory responses *in vivo*. Equally important, the formyl peptide receptor-targeting probe-based *in vivo* fluorescence imaging can provide an alternative method for analyzing a biomaterial's tissue compatibility in a rapid, non-invasive and real-time manner. This would greatly improve our understanding of the processes and factors governing foreign body responses to biomaterials while reducing the numbers of animals needed to carry out the *in vivo* testing. Furthermore, this fluorescence imaging technique may have a practical application in the evaluation and diagnosis of implant safety and performance.

Taking advantage of the high affinity of peptide cFLFLFE to the neutrophils' formyl peptide receptor, the formyl peptide receptor-targeting NIR probe has been developed to detect activated neutrophils. The probes were found to have high affinity for neutrophils *in vitro* and are able to detect and quantify the degree of LPS-induced inflammatory responses and foreign body reactions *in vivo.* Further study has uncovered that the formyl peptide receptor-targeting probe can be used to distinguish sterile vs. infected catheters. These results demonstrate that the developed formyl peptide receptor-targeting probe can be used as an *in vivo,* noninvasive, imaging tool for the real time evaluation of biomaterial safety and tissue compatibility.

## 3.3 Investigation of a folate receptor-targeting NIR probe for macrophage detection

### *3.3.1 Purpose*

Macrophages are well recognized as an important player in mediating chronic inflammatory responses. This study is aimed at developing a new imaging tool to detect

macrophage-associated inflammatory responses. For that, imaging probes targeting folate receptors on activated macrophage surfaces were tested for their ability to monitor inflammatory response-associated macrophage accumulation in *vivo*. Specifically, NIR dye-trapped PNIPAM-co-St nanoparticles were synthesized and then conjugated with folate. The efficacy of folate receptor-targeting probes in recognizing activated macrophages was studied *in vitro*. Using an *in vivo* imaging system, the effectiveness of folate receptor-targeting probes in determining macrophages recruitment to the biomaterial implantation site was assessed. Finally, by comparing probe fluorescence intensities and histological evaluations, we explore the possibility of using folate receptor-targeting probes to continuously monitor and quantity the extent of inflammatory responses to different biomaterial implants *in viv*o.

*3.3.2 Materials and Methods*

3.3.2.1 Preparation and characterization of folate receptor-targeting probes.

The folate receptor-targeting probe was fabricated as recently described [141]. Briefly, PNIPAM-co-St nanoparticles were synthesized by emulsion polymerization as described previously [142, 143] with the supplement of 5 mol% APMA to create -$NH_2$ bearing nanoparticles. The trapping of IR750 dye into PNIPAM-co-St nanoparticles was then carried out according to published procedures[144]. Absorbance and fluorescence spectra of free and loaded IR750 were determined by UV/vis spectrophotometer and fluorescence spectrometer. The photo stability of loaded IR750 vs free IR750 was evaluated by measuring the change in emission intensity before and after continuous exposure for 3.5 hours under an incandescent lamp (100W, GE lighting). Folate receptor-targeting probes were fabricated by coupling folate into the IR750-loaded nanoparticles (folate: NP = 2:5 weight ratio) using an established EDC procedure [67, 145]. The illustration of folate receptor-targeting probes is shown in Figure 3.18. Finally, coupling efficiency of folate was estimated to be 0.3 wt% (folate percentage of the probe) by using a UV spectroscopic method as described in previous publications [146-148].

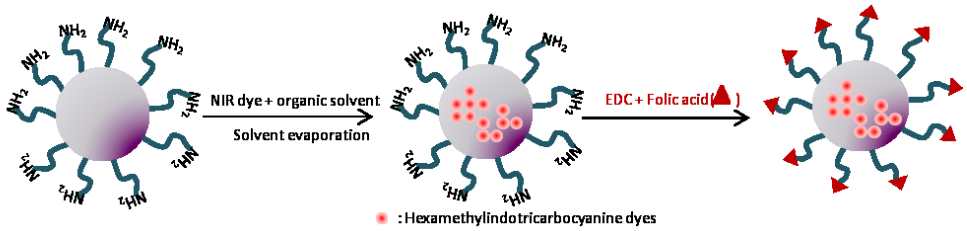


Figure 3.18 Schematic illustrations of folate receptor-targeting probes.

3.3.2.2 *In vitro* macrophage targeting of folate receptor-targeting probes

Prior to each experiment, murine Raw264.7 MFs (ATCC, Manassas, VA.) were plated at 300,000 cells/ 500 ml/well in 24 well plates and then cultured overnight. To up-regulate cell surface folate receptor expression, cultured Raw 264.7 macrophages were activated by the supplement of 1.0 mg/ml LPS (from E-coli, Sigma, St. Louis, MO) for 4 hours as described earlier [110]. After LPS incubation, cells were washed twice with HBSS to remove non-adherent cells. Variously treated probes were then incubated with adherent cells for different periods of time, followed by washing cells with PBS buffer three times to remove unlabeled probes. The extent of probe accumulation was then quantified by measuring fluorescence intensity at emission of 830 nm (excitation at 760 nm) using a Tecan Infinite M 200 plate reader (San Jose, CA). In addition, to verify whether probe accumulation is mediated by conjugated folate, a probe cell adhesion study was carried out in the presence of various concentrations (2.3-18 mM) of free folate as previously established [149].

3.3.2.3 *In vivo* imaging of inflammatory response-mediated macrophage recruitment

To test the efficacy of folate receptor-targeting probes in targeting distal inflammatory responses, LPS (100 mg/50 ml saline/animal) and saline (50 ml, as a control) were injected subcutaneously in the back of mice (n = 6) [150]. To investigate foreign body reactions to particle implants, PLA particles (~8 um in diameter, 100 ml, 10% w/v) and PEG particles (~150 nm in diameter, 100 ml, 10% w/v) and saline (100 ml) were injected subcutaneously in various dorsal regions of the mouse (n = 6). After injection for 24 hours, folate receptor-targeting probes (0.1 mg per mouse) were administered intravascularly and then imaged. Whole body images of

mice were taken using KODAK *In vivo* FX Pro (f-stop: 2.5, excitation filter: 760 nm, emissions filter: 830 nm, 4 × 4 binning; Carestream Health, Rochester, NY).

3.3.2.4 IHC evaluation of biomaterial-mediated tissue responses

To determine the extent of inflammatory responses to implants, at the end of the study, implants and surrounding tissues were isolated. IHC was performed to quantify the number of FR+ cells and CD11b+ cells using established procedures [65, 119, 126]. To evaluate inflammatory cells, some tissue sections were stained with inflammatory cell marker CD11b (rat anti-mouse MAC-1, Santa Cruz Biotechnology), and monocyte/macrophage marker (MOMA-1, Santa Cruz Biotechnology). All histological imaging analyses were performed on a Leica microscope (Leica,Wetzlar, Germany). To visualize the distribution of folate receptor-targeting probes in tissues, fresh tissue sections were imaged using Zeiss Axiovert 200 microscope (Carl Zeiss Inc., Thornwood, NY) with a cooled CCD camera as previously described [151, 152].

3.3.2.5 Data Analyses

For *in vitro* study, the fluorescence intensities folate receptor-targeting probe were measured using a Tecan Infinite M 200 plate reader (San Jose, CA) at emission of 830nm (excitation at 760 nm). The fluorescence intensities of whole body imaging were calculated using Carestream Molecular Imaging Software, Network Edition 4.5 (Carestream Health). In brief, regions of interests (ROIs) were drawn over the implantation locations after background correction, and the mean fluorescence intensities for all pixels in the fluorescent images. Quantitative histological analysis (H&E) of the total number of inflammatory cells and IHC analysis of the number of recruited inflammatory cells (including the results from CD11b+ and MOMA+) throughout the implantation sites were performed using NIH ImageJ (National Institutes of Health, Bethesda, MD) [119, 126].

3.3.2.5 Statistical analyses

All the results will be expressed as mean ± Standard error of the mean. One-way analysis of variance (ANOVA) and student t-test were performed to compare the difference

between groups. A value of $p < 0.05$ was considered to be significant. Linear regression analyses were used to determine the relationship between fluorescent intensities and cell numbers *in vitro*, as well as assessing the correlation between fluorescent intensities and macrophage cell numbers *in vivo*. The coefficient of determination ($R^2$) was calculated providing a measure of correlation.

*3.3.3* Results

3.3.3.1 Fabrication and characterization of folate receptor-targeting probes

PNIPAM-co-St nanoparticles had an average diameter of ~100 nm at 25 °C. IR750 is a hydrophobic dye with maximum absorbance at 731 nm and maximum emission at 758 nm (Figure 3.19). To label nanoparticles, IR750 was physically encapsulated into the polystyrene-rich domains of the nanoparticles by hydrophobic association. The IR750-nanoparticle loading efficiency was calculated to be about 3.5% (w/w) according to the calibration curve: $y = 36.252 - 0.0061$, $R^2 = 0.99$. As reported elsewhere [153], a red shift of ~24 nm and ~32 nm was observed for the absorbance and emission of the loaded IR750 (Figure 3.19a), respectively. This may be ascribed to the enhanced interactions between segments of the polystyrene chain, leading to a decrease of transition energy of chromophores of IR750 [145]. Additionally, as the hydrophobic microenvironment of polystyrenes was impermeable to solvent (water) and oxidative agents, such as dissolved oxygen, the photo stability of the physically-entrapped IR750 was substantially improved (Figure 3.19b) [145, 153]. After exposure to light for 3.5 hours, the emission intensity decreased by ~30% for free IR750 but only by ~3% for the loaded IR750. Folate receptor-targeting probes were obtained by conjugating folate into IR750- loaded nanoparticles using carbodiimide coupling methods. We find that the folate receptor-targeting probes trigger no statistically significant cytotoxicity over the studied concentration range (up to 0.2 mg/ml) (Figure 3.20), indicating that the above-prepared probes possess adequate cell compatibility for further *in vivo* testing.

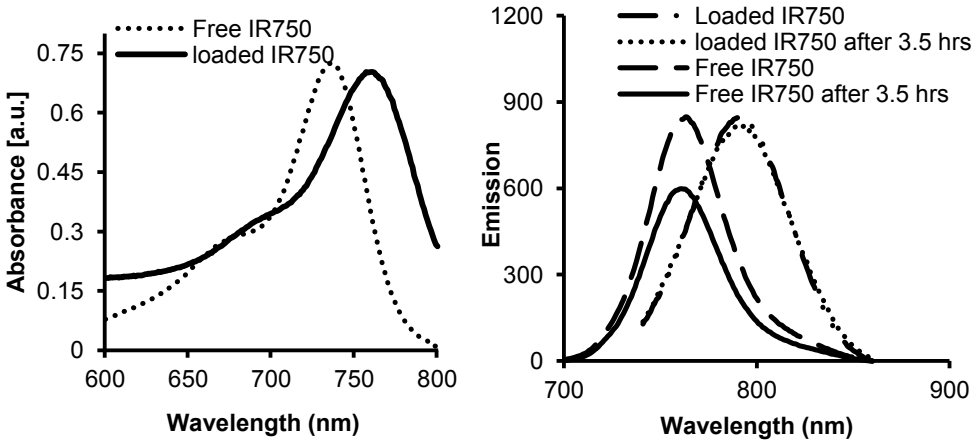


Figure 3.19 Characterizations of the optical property of folate receptor-targeting (FR-targeting) probes. (a) Absorbance spectra of free IR750 and loaded IR750 were determined based on UV-vis spectrophotometer. (b) Emission spectra of free and entrapped IR750 were determined based on fluorescence spectrometer.

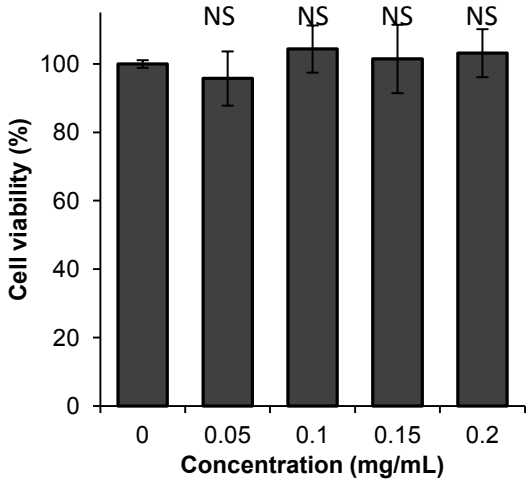


Figure 3.20 Cytotoxic study of folate receptor-targeting probe (0-0.2 μg/ml) was carried out using 3T3 fibroblasts and MTS assay. Vertical lines denote ± 1SD (n= 5 in all cases). Significance vs. no treatment: NS – no statistical significance

3.3.3.2 Effectiveness of folate receptor-targeting probes on targeting activated macrophages *in vitro*

To investigate the interaction between folate receptor-targeting probes and activated macrophages, LPS-treated rat Raw 264.7 macrophages were incubated with folate receptor-targeting probes or control probes for either 15 or 30 min. The results show that a substantial amount (~9 fold compared with controls) of folate receptor-targeting probes were associated

with activated macrophages after 15 min of exposure and that the uptake of folate receptor-targeting probes increased after 30 min of exposure (~10 fold compared with controls) (Figure 3.21a). To further confirm the specific interactions between probes and folate receptors on activated macrophage surfaces, we performed a competition binding test in which free folate molecules were introduced to the medium before the addition of folate receptor-targeting probes. As expected, fluorescence intensity is substantially decreased with increasing concentrations of free folate, suggesting that folate receptor-targeting probes have high affinity for activated macrophages (Figure 3.21b). Furthermore, by incubating folate receptor-targeting probes with different numbers of activated macrophages, we find that there is a linear relationship between the activated macrophage numbers and fluorescence intensities (Figure 3.22). This data supports our hypothesis that folate receptor-targeting probes may be used to quantify the number of activated macrophages *in vitro*.

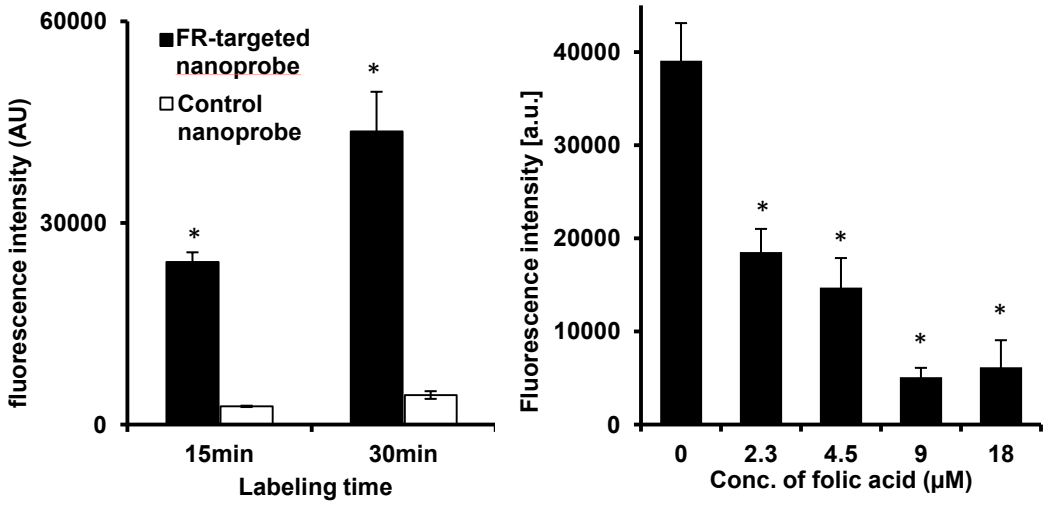


Figure 3.21 Investigation of the specificity of folate receptor-targeting probes to target activated macrophages *in vitro*. (a) Influence of incubation time on the accumulation of folate receptor-targeting probe and control probe onto activated macrophages. (FR: folate receptor) (b) Interference of different concentrations of free folate molecules on the binding of folate receptor-targeting probe to activated macrophages. The averages of fluorescence intensities were quantified. Vertical lines denote ± 1SD (n = 5 in all cases). Significance: * $p<0.05$.

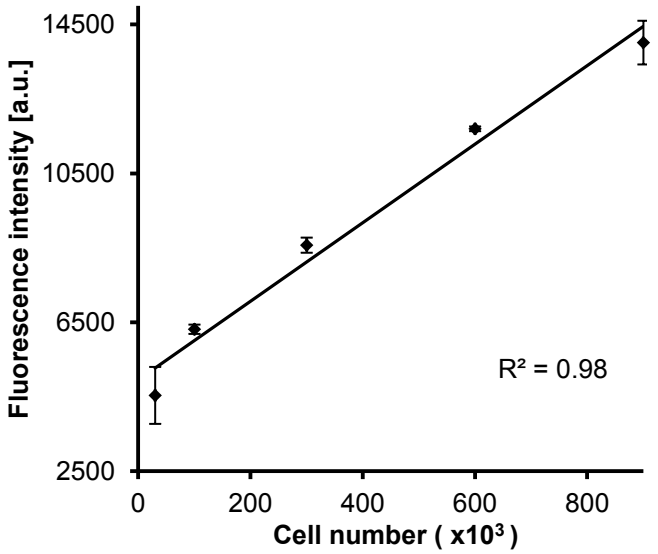


Figure 3.22 Correlation between activated macrophage numbers and folate receptor-targeting probes associated fluorescence intensities following incubation with folate receptor-targeting probe. The linear regression has $R^2 = 0.98$.

3.3.3.3 Detection of activated macrophages in vivo using folate receptor-targeting probes

To test whether folate receptor-targeting probes can be used to detect activated macrophage accumulation in inflamed tissue in vivo, an LPS-induced subcutaneous inflammation model was used. After 24 hours LPS challenge, folate receptor-targeting probes or control probes were administered intravenously. Our results reveal that the fluorescence intensities at the LPS injection site were substantially higher than saline controls regardless of the probe used (Figure 3.23). We also determined the ability of the probe to distinguish inflamed vs. control tissues by calculating their enhancement ratios (ratio of fluorescence intensity at LPS-site vs. saline-site). At 24 hours, our results show a substantially higher fluorescence enhancement ratio (~2.7 fold) in the folate receptor-targeting probes group than that in the control group (Figure 3.24). Histological evaluations also show that the LPS challenge resulted in tissue with ~6 fold higher folate receptor-positive inflammatory cells than the saline treatment (Figure 3.25a). As expected, we also found that the LPS challenge triggered ~6 times higher CD11+ inflammatory cell recruitment than the saline control (Figure 3.25b). These results

strongly support our hypothesis that folate receptor-targeting probes have the ability to non-invasively detect activated macrophages and may be used to monitor the biomaterial-mediated inflammatory processes in real time.

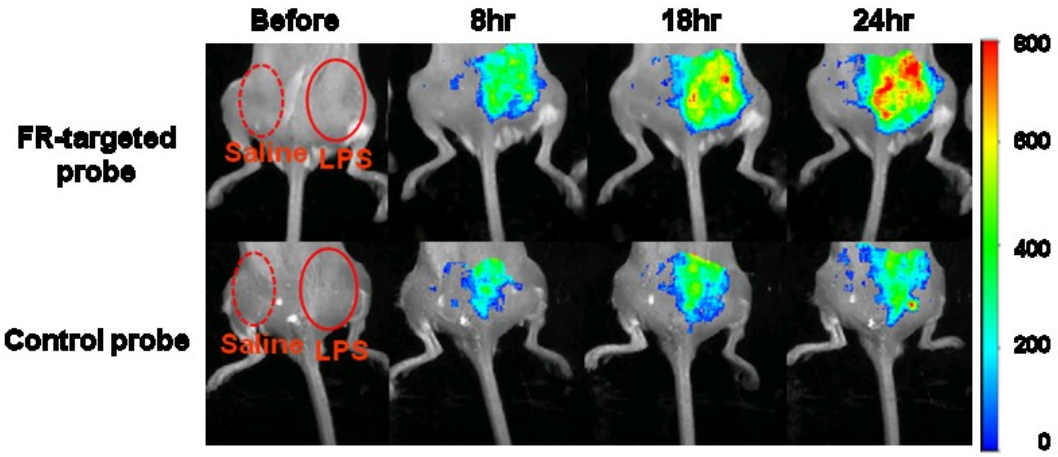


(a)

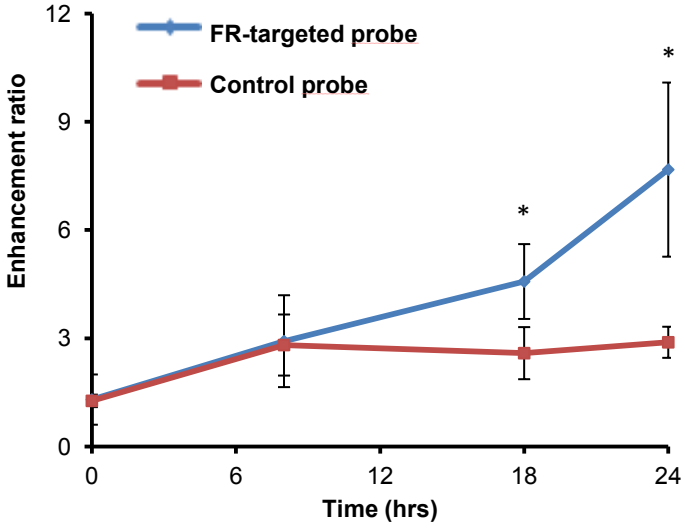


(b)

Figure 3.23 In the LPS-induced inflammation model, the folate receptor-targeting probe and its control probe were injected intravenously 24 hours after LPS subcutaneous administration. (a) The merged fluorescent signal with a white-light animal image for the folate receptor-targeting probe groups and the control probe groups at different time points following probe administration. (b) The average enhancement ratio of LPS-induced inflamed sites vs. saline control in the folate receptor-targeting probe and the control probe at different time points were quantified. Vertical lines denote ± 1SD (n = 6 in all cases). Significance vs. control probe: * $p<0.05$ (FR: folate receptor)

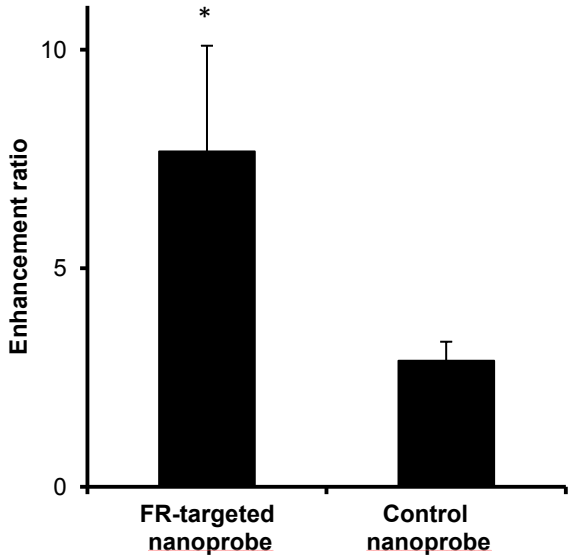


Figure 3.24 In the LPS-induced inflammation model, the folate receptor-targeting probe and its control probe were injected intravenously 24 hours after LPS subcutaneous administration. The average enhancement ratios of fluorescence intensities between folate receptor-targeting probe and control probe in LPS-treated inflamed sites at 24 hours were quantified. (FR: folate receptor)

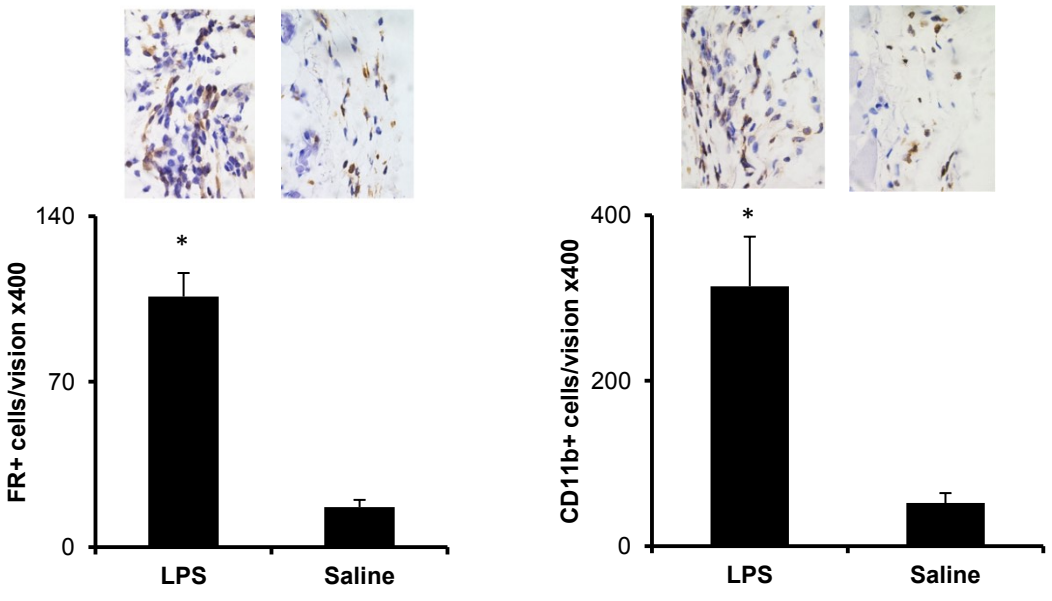


Figure 3.25 (a) Representative FR+ cell staining and FR+ cell number quantification in isolated tissue 24 hours following either LPS or saline treatment. (b) Representative CD11b+ cell staining and CD11b+ cell number quantification of LPS- and saline-treated tissues isolated 24 hours after probe injection. Significance vs. control probe: * $p<0.05$.

3.3.3.4 Quantification of foreign body reactions *in vivo* using folate receptor-targeting probes

Subsequent studies were carried out to explore the possibility of using folate receptor-targeting probes to assess inflammatory reactions to different biomaterial implants in vivo. PLA and PEG particles were chosen as model materials which have been shown to trigger strong and weak inflammatory responses, respectively [127, 154]. After prior injection (24 hours incubation) with different types of particles or saline as injection control, the folate receptor-targeting probes were introduced via tail vein injection and the animals were subjected to whole body imaging at various time points. In general, fluorescent signals in both PLA and PEG sites increased over time, and the signal intensities in the PLA implantation sites were consistently higher than those in PEG sites (Figure 3.26). Furthermore, saline controls had very low or no fluorescent signals during the same time periods. The varying trends of fluorescence intensities were consistent and statistically significant between different test materials 6 hours after folate receptor-targeting probe injection. To determine the distribution of the probe in the inflamed tissue, NIR microscopic images of sections of PLA implant sites were taken (Figure 3.27). The microscopic images show that folate receptor-targeting probes accumulate in tissue adjacent to the PLA implants and that substantially fewer probes are found in normal tissue. IHC analyses reveal that, after 24 hours implantation, saline injection prompts negligible CD11b+ inflammatory cell recruitment and conversely, PLA implants are consistently infiltrated by more CD11b+ inflammatory cells than the PEG implants (Figure 3.28). Similar trends were also found for monocyte/macrophages (MOMA+ cells) recruitment. Overall, it was found that the PLA implants recruited 3 fold higher CD11b+ inflammatory cells and MOMA+ macrophages than PEG implants (Fig. 3.28). To determine the relationship between the folate receptor-targeting probe accumulation and implant-mediated macrophage responses, we correlate both the CD11b+ inflammatory cells and MOMA+ macrophage count with the fluorescence intensity. Our results show good near linear trends in both cases ($R^2$ = 0.80 & 0.96) (Figure 3.29). These

results support our assumption that folate receptor-targeting probes can be employed as an effective imaging probe to detect and to assess the extent of biomaterial-mediated macrophage recruitment and inflammatory responses *in vivo*.

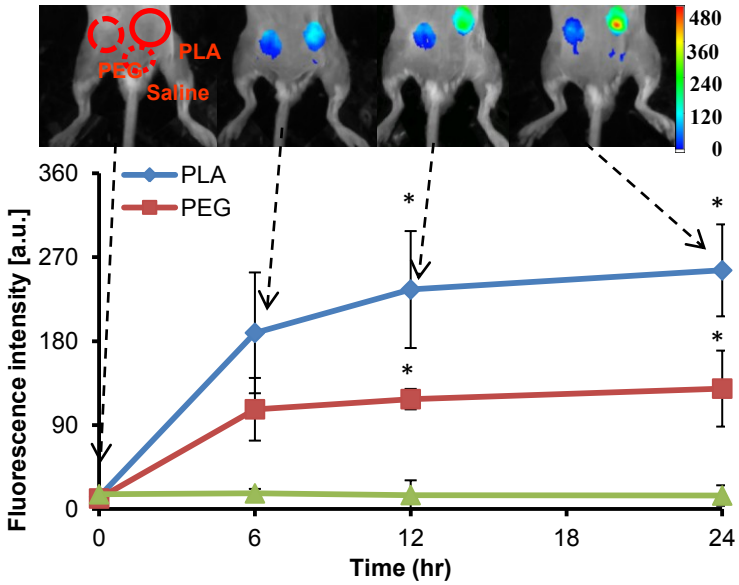


Figure 3.26 In a foreign body response mice model, PLA, PEG, and saline were implanted subcutaneously in the back of animals for 24 hours prior to folate receptor-targeting probe intravenous administration. The representative merged fluorescence and white light image shows the accumulation of folate receptor-targeting probes at different implantation sites of PLA, PEG and saline at different time points. The averages of fluorescent intensities at the implantation sites were quantified. Vertical lines denote ± 1SD (n = 6 in all cases). Significance vs. saline treatment: * $p<0.05$

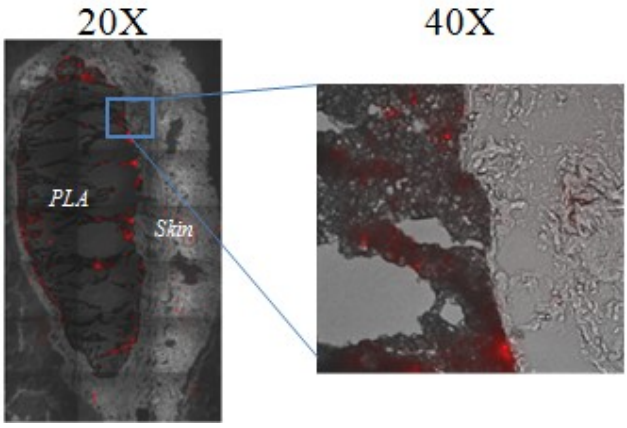


Figure 3.27 In a foreign body response mice model, PLA, PEG, and saline were implanted subcutaneously in the back of animals for 24 hours. After folate receptor-targeting probes probe injection for 24 hours, the tissues surrounding implant sites were isolated for NIR fluorescence (red) acquisition superimposed onto the correlative phase contrast microscopy image in the whole stitched image (20X) and enlarged view (40X). The tissue section was unstained and unfixed to preserve fluorescent signal.

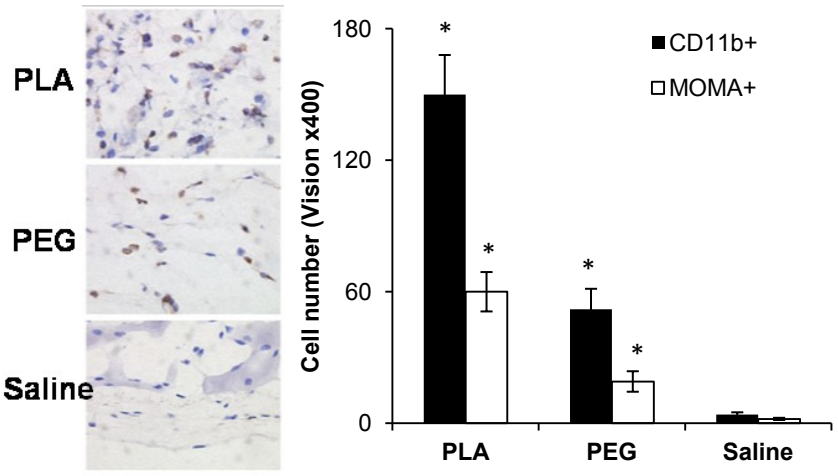


(a) (b)

Figure 3.28 In a foreign body response mice model, PLA, PEG, and saline were implanted subcutaneously in the back of animals for 48 hours. (a) Representative IHC staining Images, and (b) the averages of CD11b+ inflammatory cells and MOMA+ macrophages in tissue surrounding the implantation sites of PLA, PEG and saline. The inflammatory cells counts and MOMA+ macrophages counts per view field were quantified on IHC stained slides by Image J. Vertical and parallel lines denote ± 1SD (n = 6 in all cases). Significance vs. saline treatment: * $p<0.05$.

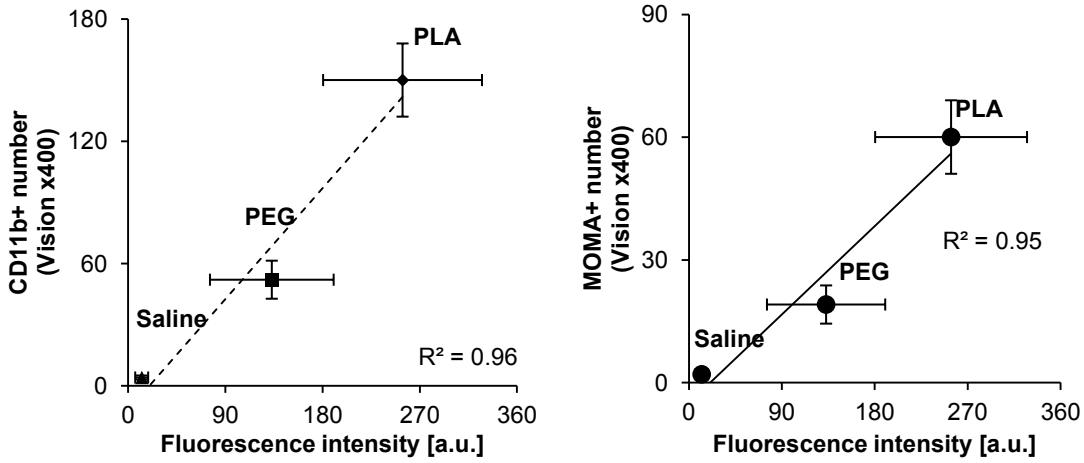


(a) (b)

Figure 3.29 Correlation between fluorescence intensity (Figure 3.27) and CD11b+ cell number/ MOMA+ macrophages numbers (Figure 3.28b) and at the different implantation sites of PLA, PEG and saline. Vertical and parallel lines denote ± 1SD (n = 6 in all cases). The linear regression has coefficient $R^2$= 0.92.

*3.3.4 Discussion and Conclusion*

In the present study, folate receptor-targeting probes based on PNIPAM-co-St nanoparticles were prepared to noninvasively evaluate inflammation by targeting activated

macrophages. The uniform nanoparticle with an average diameter of ~100 nm makes it a suitable vehicle for *in vivo* imaging. Previous studies suggest that particles ranging from 10 nm to 200 nm are optimal for prolonging blood circulating times. Furthermore, the presence of PNIPAM segments on the nanoparticles may greatly reduce the binding of plasma proteins to the particles, thus enhancing particle biodistribution [155-157]. Finally, it has been reported that PNIPAM and PNIPAM-based nanoparticles exhibit little or no cytotoxicity. Our *in vitro* studies demonstrate that the folate receptor-targeting probe can be used to assess the number of recruited and activated macropahges *in vivo*. The success of this strategy is supported by many previous findings. Specifically, activated macrophages have up-regulated folate receptor expression which has previously been used for targeting molecules [67, 158]. Interestingly, similar to our findings, prolonged incubation time was found to enhance uptake of folate receptor-targeting probes which may be ascribed to a folate-mediated endocytosis by macrophages [118]. It is possible that prolonged exposure to activated macrophages may lead to the endocytosis of initial adherent folate receptor-targeting probes while allowing additional probes to be bound to folate receptors on the cell surface. Such internalization may increase the resident time of folate receptor-targeting probes and increase the sensitivity of such probes for detection of activated macrophages at the implantation sites *in vivo*. Folate receptor-targeting probes were found to preferentially accumulate in the LPS-induced inflamed tissue. These results support the hypothesis that such probes can be used to detect activated macrophages and to indirectly assess the extent of inflammatory responses in tissue. This assumption is supported by many previous observations. First, it is well established that the administration of LPS prompts a localized inflammatory responses with the upregulation of many inflammatory cytokines [159, 160], and the accumulation of inflammatory cells, including activated macrophages [119, 154, 161]. Second, by targeting activated macrophages, several strategies have been developed to deliver therapeutic and imaging agents [118, 120, 158, 161]. Finally, folate receptor-targeting probes have been developed to noninvasively analyze inflammatory

activity in atherosclerosis and arthritis in situ [67, 120, 149, 158]. Interestingly, our study has also uncovered that, despite of a lack of folate, some control probes were found in the inflammatory tissue (~30% of folate receptor-targeting probe). The cause of non-specific accumulation has yet to be determined. However, it has been suggested that particle accumulation in tissue could be mediated by non-specific phagocytosis in activated macrophages or entrapment in the interstitial space due to the “enhanced permeability and retention” effect (EPR effect) within the inflamed tissues [33, 161, 162]. Using polymer particles as model implants, our studies have preliminarily explored the possibility of using folate receptor-targeting probes to detect activated macrophages in the biomaterial implantation sites. Further analyses revealed that there is a good relationship between folate receptor-targeting probe accumulation and CD11b+ inflammatory cell/macrophage recruitment in the implantation sites. These results demonstrate that the folate receptor-targeting probes can be used not only to determine the inflammation location as reported earlier [55, 119, 158], but also to estimate the extent of biomaterial-mediated macrophage recruitment and associated inflammatory responses. We believe that folate receptor-targeting probes can also be used to quantify the degree of inflammatory responses to other types of biomaterial implants. Since the folate receptor-targeting probes are designed to target activated macrophages, representing the major subset of the inflammatory cells, we believe that folate receptor-targeting probes would provide heightened sensitivity and reliability in the assessment of cellular responses to biomaterial implants, as opposed to other imaging probes currently testing foreign body reactions. Equally important, we anticipate that the folate receptor-targeting probe-based *in vivo* fluorescence imaging can provide an alternative method for analyzing biomaterial biocompatibility in a rapid, noninvasive and real time manner. This would greatly improve our understanding of the processes and factors governing foreign body responses to biomaterials. Furthermore, this fluorescence imaging technique may have a practical application in the evaluation and diagnosis of implant safety and performance.

# CHAPTER 4

# INVESTIGATION OF OPTICAL IMAGING TOOLS FOR DETECTING PHYSICAL PROPERTIES

## 4.1 Introduction

Upon arrival at injured or inflamed sites, inflammatory cells release a variety of products, such as free radicals, ROS, proteases, cytokines and growth factors [3, 13]. It is well established that the amount of inflammatory cell released products reflect the extent of the inflammatory response. Therefore, real time monitoring of inflammatory cell products may provide a good indication of the extent of inflammatory responses. To test this hypothesis, we are specifically interested in Reactive Oxygen Species (ROS) - products mostly produced by neutrophils [163]. Many methods, including spectrophotometric measurements, electron spin resonance spectroscopy, ELISA, chemiluminescence, etc, have been used to assess the release of ROS by inflammatory cells [164]. Although many of these methods can be used to measure ROS activities, several chemiluminescence probes have been developed for noninvasive real time imaging *in vivo*. For instance, peroxalate nanoparticles were fabricated and used as a chemiluminescence probe to detect $H_2O_2$ *in vivo* [165, 166]. Oxazine conjugated nanoparticles have been synthesized and used to detect *ex vivo* hypochlorous acid and peroxynitrite generation in mouse hearts after myocardial infarction [167]. A chemiluminescence probe, luminol, has been used in studies to detect myeloperoxidase activity, the pathogenesis of arthritis, and biomaterial-induced ROS activities *in vivo* [168-170]. Although these chemiluminescence probes (peroxalate nanoparticles and luminol) have shown great promise for *in vivo* monitoring of ROS activities following severe inflammatory responses, the limited sensitivity of these probes substantially limits their use in measuring and especially quantifying localized inflammatory responses.

Tissue acidosis is another well characterized phenomenon which usually occurs in and surrounding inflamed tissue [2, 20]. Traditionally, tissue damage can be measured by the use of pH microelectrodes [171]. However, pH microelectrodes cannot be used to carry out reliable measurements in tight spaces around biomaterial implants. Many pH sensitive fluorescence dyes have been synthesized to respond to pH changes, but only very few of these dyes can be used to reliably detect acidic pH (pH 4 - 7.4) [50, 172-174]. Unfortunately, most of these probes are also concentration-dependent. They therefore cannot be used to quantify the pH changes in a dynamic environment such as real tissue *in vivo*. To address such deficiencies, several recent investigations have evaluated pH imaging in isolated cells and tissues using 2',7'-bis(carboxyethyl)-5,6-carboxyfluorescein (BCECF) fluorescence ratio techniques. The drawbacks of BCECF are that the fluorescent wavelengths remain in the visible-range with strong auto-fluorescent background and very limited penetration depth and cannot be used for *in vivo* imaging [175, 176]. Recently, some research has demonstrated the design and synthesis of a ratiometric near infrared probe for evaluating pH changes [50, 177]. Nevertheless, their applications are still limited to the intracellular levels [50].

## 4.2 Noninvasive assessment of localized inflammatory responses

### *4.2.1 Purpose*

Recruited macrophages and neutrophils have been found to release a wide variety of inflammatory products, including ROS, to eradicate foreign bodies and microorganisms [163, 178]. Recently, a chemiluminescence probe L-012 has been shown to have increased sensitivity toward ROS than previous probes such as luminol and lucigenin [68, 69]. A series of studies were carried out to assess the ability of L-012 to detect inflammatory response-mediated ROS activities *in vitro* and *in vivo.* The general assumption of a good relationship between the amount of inflammatory product release and the extent of inflammatory responses was then tested using imaging probes, whereby the production of ROS was detected in real time.

*4.2.2 Materials and methods*

4.2.2.1 *In vitro* chemiluminescence imaging of the ROS probe

ROS measurements were carried out using both L-012 (Wako, Osaka, Japan) and luminol (Sigma–Aldrich, St. Louis, MO) as chemiluminescent probes. *In vitro* imaging was carried out in black-bottom 96-well plates: 200 µl of $H_2O_2$ solution of various concentrations was mixed with 10 µl of L-012 (50 mM). Neutrophils were isolated from mouse peritonea after casein administration as described earlier [179]. The chemiluminescence images were taken 1 min later using a KODAK *In Vivo* FX Pro system (f/stop, 2.5; no optical filter, 4×4 binning, Carestream Health, Rochester, NY). *In vitro*, various numbers of neutrophils (in Hanks' buffered solution) were incubated with L-012 (2mM) or luminol (4mM) for 4 min at room temperature. The ROS production was then initiated by adding 10 µl of phorbol 12-myristate 13-acetate (PMA, 6.5 nM). In some experiments, Tempol, a superoxide scavenger, was used to neutralize ROS products in solution. For that, cells were incubated with various concentrations of Tempol before PMA activation.

4.2.2.2 *In vivo* Inflammation and infection animal models

To detect $H_2O_2$-mediated chemiluminescence activities, 200 µl of $H_2O_2$ solution (0.5mM) and 100 µl of L-012 (15 mg/ml) were mixed at room temperature. Various volumes of solutions (20, 40, 60, and 80µl) were injected subcutaneously into the back of anesthetized mice (n = 6). Chemiluminescence images were captured with a 5-min acquisition time using a KODAK In Vivo FX Pro system (f/stop, 2.5; no optical filter, 4×4 binning). To induce localized inflammatory responses, PLA microspheres (50 µl, 10% wt in saline), or saline as a control, were implanted subcutaneously into various locations on the back of mice (n = 6). L-012 solution (100 µl, 15 mg/ml) was then administered intraperitoneally at various time points. It should be noted that L-012 has very good biocompatibility and low toxicity [58]. Previous studies showed that L-012 has no apparent effect on the immune responses of animals up to 150 mg/kg (n = 2) [91]. The nontoxic or low toxic nature of L-012 permits its use in cell culture

studies and animal work. Chemiluminescence images were captured sequentially every 5 minutes up to 1 hour. Similar experiments were carried out using neutrophil-depleted mice, which were produced based on a modified published protocol (n = 6) [123]. In brief, 100 µl of neutrophil neutralizing antibody (rabbit anti-mouse PMN; Accurate Chemical & Scientific Corp.) was injected intraperitoneally and 18 hours later a second injection of 100 µl antibody was given intraperitoneally 4 hours after the second injection, 50 µl of PLA particles (10% wt/vol) were implanted subcutaneously on the back of the PMN-depleted mouse and a control mouse. The chemiluminescence images were taken 24 hours after PLA implantation. To investigate the effects of either catalase (a scavenger of $H_2O_2$) or Diethylene triamine pentaacetic acid (DTPA, a metal chelator) on implant-mediated chemiluminescence, 50 µl of PLA particles (10% wt) were mixed with catalase (500units/ml), DTPA (1 mM), or saline (as control) before subcutaneous implantation (n = 3). To trigger varying extents of inflammatory responses in the same animals, PNIPAM-$NH_2$, PLA, PEG particles (50 µl, 10% wt/vol), and saline (control) were injected subcutaneously into different locations on the backs of mice (n = 6). To mimic infection-mediated inflammatory responses, 100 µg/50 µl of LPS was administered subcutaneously on the backs of Balb/c mice, whereas treatment with saline alone was used as control. To elicit skin allergenic responses, some animals were subcutaneously injected with 100 µg of compound 48/80 or saline (n = 6). To monitor the extent of foreign body reactions, PU catheters and heparinized PU (H-PU) catheters (1-cm length) from Sentry Medical Products (Green Bay, WI, USA) were implanted subcutaneously on the backs of mice (n = 6). The extent of the chemiluminescence signal was detected and quantified at 24 hours after the treatment with inflammatory stimuli.

4.2.2.3 Histochemical analysis and inflammatory cell quantification

At the end of the study, the test animals were sacrificed and the implantation sites/inflamed tissues were isolated for histological analyses. All tissue sections were subjected to H&E or IHC staining for PMNs based on established protocols [27, 180].

4.2.2.4 Data Analyses

For *in vitro* study, the chemiluminescence intensities were recorded continuously for 60 min using a luminescence reader (Infinite M200; Tecan, Männedorf, Switzerland) with a 10 s acquisition time. The chemiluminescence intensities of *in vitro* imaging ($H_2O_2$-mediated effects) and whole body imaging were performed using Carestream Molecular Imaging Software, Network Edition 4.5 (Carestream Health, CT, USA). In brief, regions of interests (ROIs) were drawn over the implantation locations after background correction, and the mean intensities for all pixels in the chemiluminescence images. Quantitative histological analysis (H&E) of the total number of inflammatory cells and IHC analysis of the number of recruited neutrophils throughout the implantation sites were performed using NIH ImageJ (National Institutes of Health, Bethesda, MD) [12, 87, 88].

4.2.2.5 Statistical analysis

Statistical comparison between treatment groups was carried out using Student's t test. Differences were considered statistically significant when $p<0.05$. Linear regression analyses were also used to determine the correlation coefficient between PMN densities and chemiluminescence signal intensities.

*4.2.3 Results*

4.2.3.1 *In vitro* chemiluminescence imaging of the ROS probe

To search for a sensitive chemiluminescence probe, we compared the ROS detection sensitivity of L-012 vs luminol. Mouse peritoneal PMNs were incubated with L-012 in the presence of the potent protein kinase C activator PMA. We found that with PMA activation, both luminol and L-012 emitted chemiluminescence in a time dependent manner. Chemiluminescence of L-012 (Figure 4.1) initially increased with time and peaked at ~30 min after stimulation, whereas the maximal chemiluminescence of luminol appeared at ~15 min. Based on the peak values of the two probes, the results showed that the signal intensity

generated by the L-012 was approximately 900-fold greater than that generated by luminol (Figure 4.1). To further determine the ROS sensitivity, L-012 was exposed to increasing numbers of PMNs. As expected, ROS prompted a strong emission of chemiluminescence and chemiluminescence intensities were cell number dependent (Figure 4.2a). In addition, there was a linear relationship between the chemiluminescence intensity and the activated PMN number ( = 0.95; Figure 4.2b). To verify whether the chemiluminescence signals resulted from ROS generated by activated PMNs, similar PMN-mediated chemiluminescence measurements were carried out in the presence or absence of a superoxide dismutase mimetic/ROS neutralizer—Tempol. As anticipated, the chemiluminescence intensity was substantially reduced in the presence of as low as 5 mM Tempol (Figure 4.3). Collectively, these data indicate that L-012 can be used to estimate the numbers of activated PMN based on their ROS-mediated chemiluminescence signals. These results support the notion that L-012 chemiluminescent probes may be used to quantify the extent of neutrophil-associated ROS production.

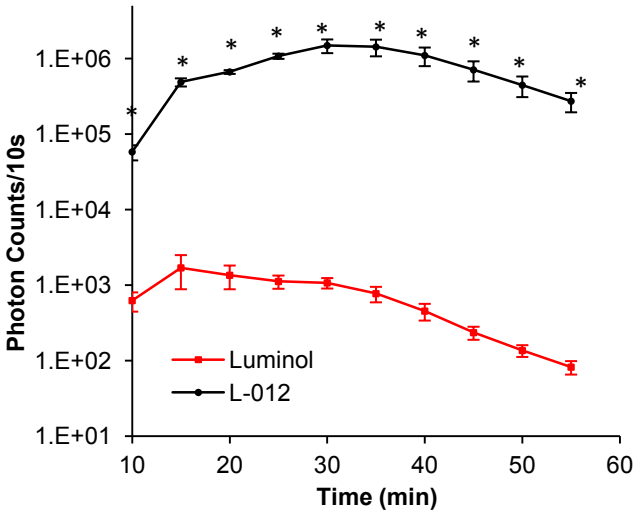


Figure 4.1 Time-dependent chemiluminescence signals for L-012 and luminol. Reaction mixtures (250 µl) contained $1\times10^6$ PMNs and 2 mM L-012 or 4 mM luminol. The ROS measurements were initiated by adding 10 µl of PMA (6.5 nM) at room temperature. Vertical lines denote ± 1SD (n = 6 in all cases). Significance vs. luminol treatment: * $p<0.05$.

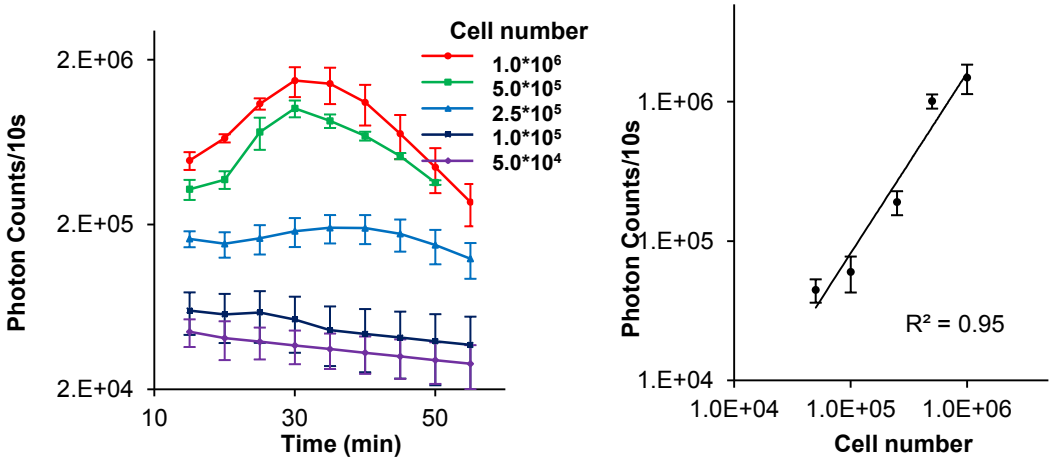


Figure 4.2 Investigation of the sensitivities of L-012 to ROS production *in vitro*. (a) Interference of different cell numbers to the ROS detection. Different numbers of neutrophils were mixed with 2 mM L-012, and ROS measurements were initiated by adding 10 µl of PMA. The average of Chemiluminescence intensities were quantified for 60min. Vertical lines denote ± 1SD (n = 5 in all cases). (b) Correlation between PMN numbers and chemiluminescence intensities at 30 minute. Vertical lines denote ± 1SD (n = 5 in all cases). The linear regression has $R^2 = 0.95$.

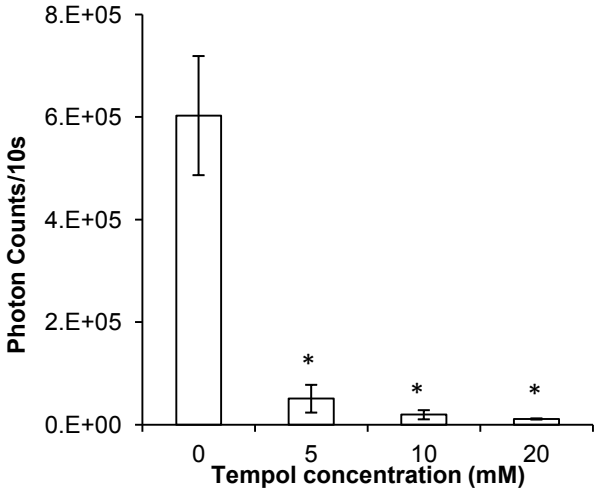


Figure 4.3 Interference of different concentrations of Tempol inhibits L-012 chemiluminescence emitted by PMA-stimulated neutrophils ($1\times10^6$). The averages of chemiluminescence intensities were quantified. Vertical lines denote ± 1SD (n = 5 in all cases). Significance vs. without Tempol treatment: * $p<0.05$.

Subsequent studies were carried out to evaluate the feasibility of L-012 for *in vivo* whole-body imaging. L-012 was used to detect $H_2O_2$ *in vitro* with a KODAK *In Vivo* FX imaging system. As expected, chemiluminescence intensity of L-012 increased with the increase in $H_2O_2$

concentration from 0.05 to 0.5 mM (Figure 4.4), and there was a linear correlation between chemiluminescence intensity and the concentration of $H_2O_2$ (Figure 4.4).

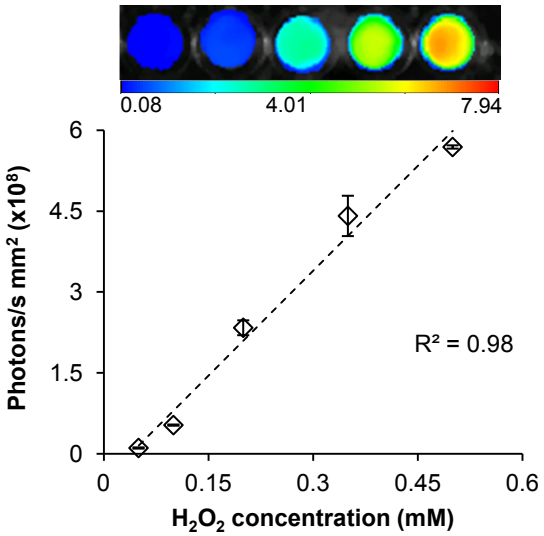


Figure 4.4 Investigation of the sensitivities of L-012 to detect ROS production *in vitro*. Different concentration of $H_2O_2$ (0.1-0.5 mM) and L-012 were mixed. Representative *in vitro* imaging and the average of L-012-mediated chemiluminescence signals at various concentrations of $H_2O_2$ were quantified. Correlation between various concentrations of $H_2O_2$ and chemiluminescence signals following L-012 incubation. Vertical lines denote ± 1SD (n = 5 in all cases). The linear regression has $R^2 = 0.98$.

4.2.3.2 *In vivo* Inflammation and infection animal models

To determine whether L-012-mediated chemiluminescence signals might be used to measure ROS release *in vivo*, various volumes (20, 40, 60, 80 µl) of $H_2O_2$ (0.5 mM) mixed with L-012 (15 mg/ml) were injected subcutaneously into animals and then imaged. As anticipated, L-012 could detect subcutaneous $H_2O_2$, which was also found to have a linear correlation between $H_2O_2$ quantity and chemiluminescence intensity (Figure 4.5). Finally, to assess whether L-012-mediated chemiluminescence can be used to assess ROS production arising *in vivo* from a known proinflammatory agent, PLA microspheres (50 µl in 10% wt), or saline as a control, were administered subcutaneously on the back of live mice. Implants were followed by intraperitoneal administration of a 15 mg/ml L-012 solution at various time points. Our results show that a prominent chemiluminescence signal could be detected at the PLA implant site, whereas only minimal signal was detected at the saline-injected site (Figure 4.6).

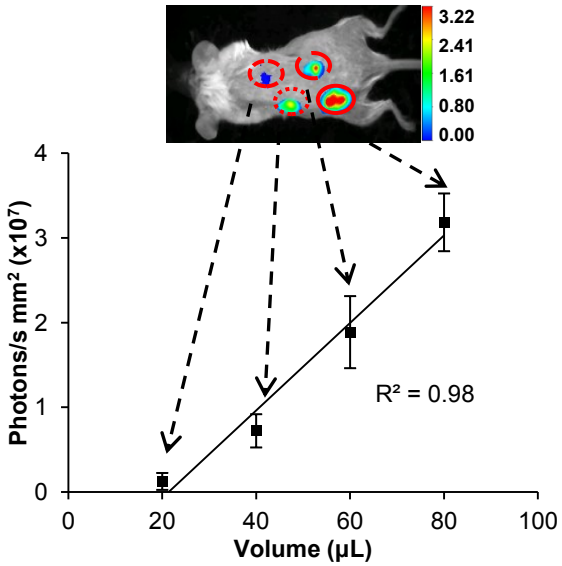


Figure 4.5 Interference of various volumes of solutions ($H_2O_2$ mixed with L-012, 20-80 µl). Solutions were injected subcutaneously into the back of mice. Representative whole body imaging and the average of L-012-mediated chemiluminescence signals at various volumes of solutions of $H_2O_2$ were quantified. Correlation between different dosages of $H_2O_2$ and *in vivo* L-012-mediated chemiluminescence signals. Vertical lines denote ± 1SD (n = 6 in all cases). The linear regression has $R^2 = 0.98$.

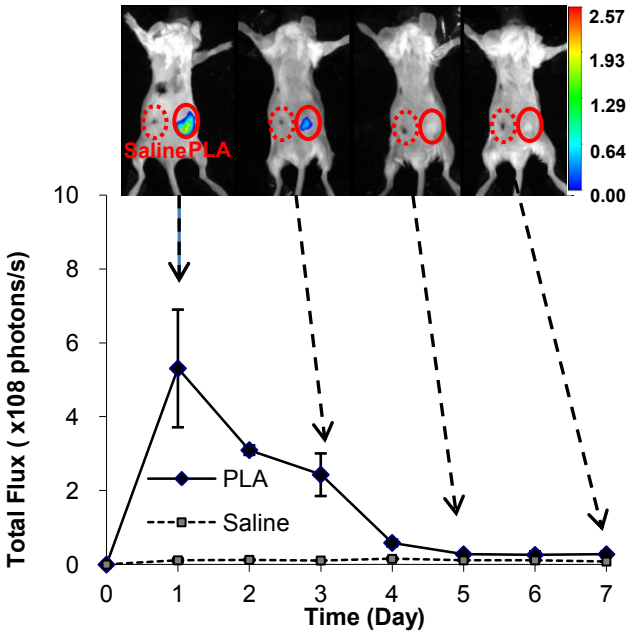


Figure 4.6 The effect of ROS production at various time points. PLA and saline (as control), were implanted subcutaneously on the back of mice. L-012 solution was then administered intraperitoneally at various time points. Representative whole body chemiluminescence imaging and the average of chemiluminescence signals (bottom) of animal subcutaneously implanted with PLA and saline (as control) for various periods of time were quantified and compared. Vertical lines denote ± 1SD (n = 6 in all cases).

As expected, histological analyses confirm that there are substantially more PMNs in tissues surrounding 1-day implants than in tissue surrounding 7-day implants (Figure 4.7). In addition, there was a good linear relationship between chemiluminescence intensity (ROS activity) and the infiltrating PMNs ($R^2$ = 0.94, Figure 4.8). These results reveal that L-012 can be used to noninvasively monitor real-time inflammation-induced ROS generation *in vivo*. Because it has been well established that neutrophils are one of the most potent types of ROS-producing cells, we assumed that neutrophil-mediated ROS would be responsible for L-012-dependent chemiluminescence signals. To test this, similar studies were carried out in neutropenic mice. Pretreatment of mice with anti-neutrophil antibodies reduced chemiluminescence by approximately 70% at the PLA implantation site compared to control mice (Figure 4.9). Interestingly, histological evaluation also revealed a ~60% reduction in infiltrating PMNs at the implantation site in neutrophil-depleted mice compared to control mice (Figure 4.10).

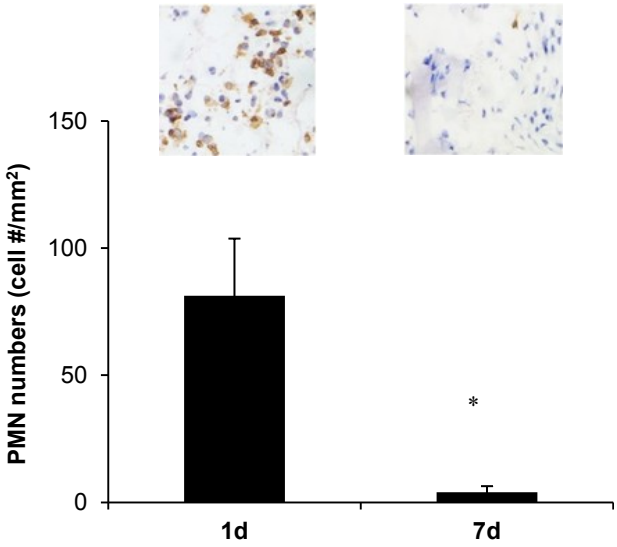


Figure 4.7 The subcutaneous recruitment of neutrophils from PLA-mediated inflammation model. PLA were implanted subcutaneously on the back of mice for 1 day and 7 days. Representative IHC neutrophil staining (400×) of PLA sites at 1 day and 7 days and quantification of neutrophils on PLA surrounding tissues were quantified based on IHC stained slices. The cells counts per view field were quantified by ImageJ. Vertical lines denote ± 1SD (n = 6 in all cases). Significance vs. saline treatment: * $p < 0.05$

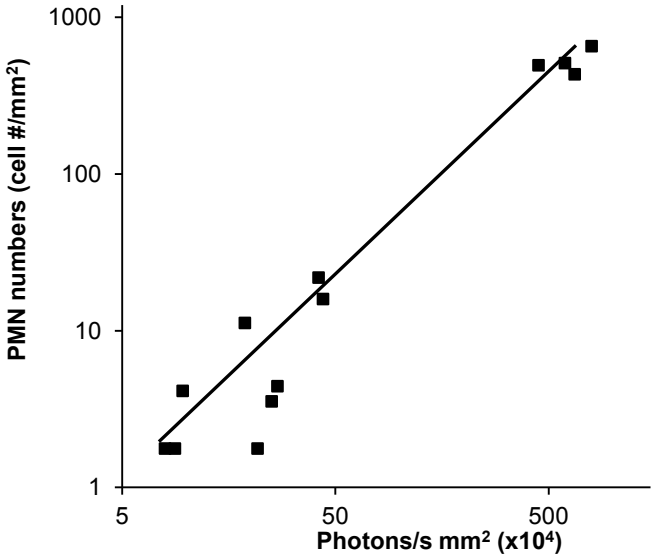


Figure 4.8 Correlation between L-012-mediated chemiluminescence signals (Figure 4.6) and PMN numbers (Figure 4.7) on PLA surrounding tissues at various time points.

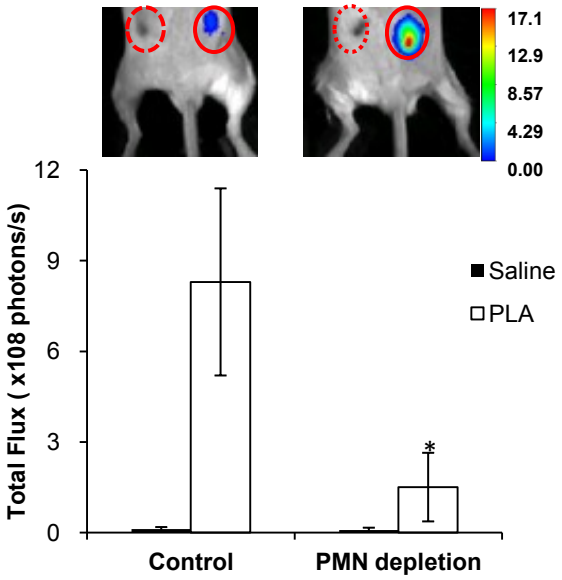


Figure 4.9 The effect of neutrophil depletion in a foreign body response model. PLA particles were implanted in neutrophil-depleted versus control mice for 24 hours prior to formyl peptide receptor-targeting probe administration. Representative whole body imaging and the average of L-012-mediated chemiluminescence signals at 30 minutes post intraperitoneal injection of L-012. The results illustrate the diminishing signals of L-012 administration in neutrophil depleted animals in comparison with controls. Vertical lines denote ± 1SD (n = 6 in all cases). Significance vs. control treatment: * $p < 0.05$.

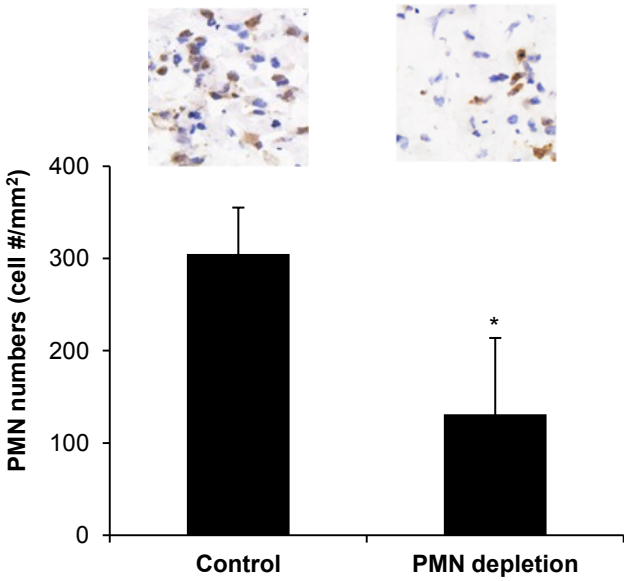


Figure 4.10 The effect of neutrophil depletion in a foreign body response model. PLA particles were implanted in neutrophil-depleted versus control mice for 24 hours. Representative IHC (600×) and quantification of neutrophils numbers at PLA implant sites either control or neutrophil depletion mice. The cells counts per view field were quantified by ImageJ. Vertical lines denote ± 1SD (n = 6 in all cases). Significance vs. control treatment: * $p < 0.05$.

Correlation analysis suggests a linear relationship between chemiluminescence intensity and number of recruited PMNs (Figure 4.11), supporting the idea that PMN-generated ROS are primarily responsible for L-012-depedent chemiluminescence signals. To determine the type of ROS detected with the L-012 probe, catalase, a potent enzyme for neutralizing $H_2O_2$, was injected into the implant sites before L-012 administration. Indeed, the treatment of catalase substantially reduced (~65%) the chemiluminescence intensity (Figure 4.12) Further studies were conducted to investigate whether metal ions participate in ROS responses, using an iron chelator—DTPA. As expected, the presence of DTPA had no significant impact on chemiluminescence intensity compared to control, suggesting that $H_2O_2$ is a major type of ROS product generated as part of foreign body reactions (Figure 4.13).

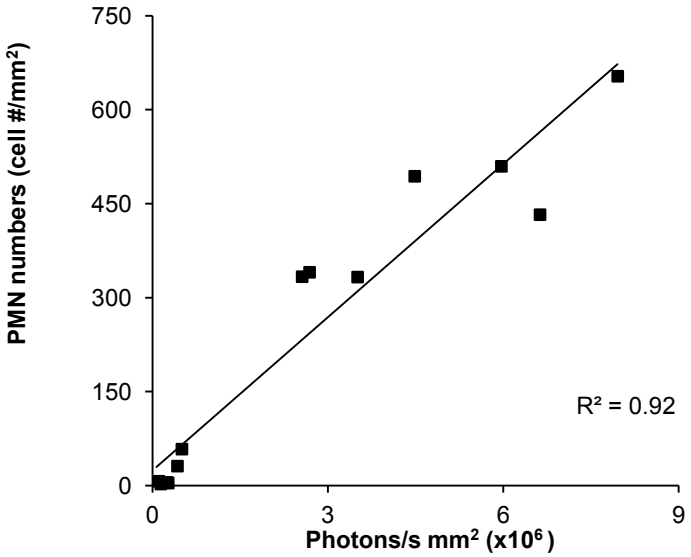


Figure 4.11 Correlation between L-012-mediated chemiluminescence signals (Figure 4.9) and recruited neutrophil numbers (Figure 4.10) in PLA surrounding tissue isolated from variously treated animals. The linear regression has coefficient $R^2 = 0.92$.

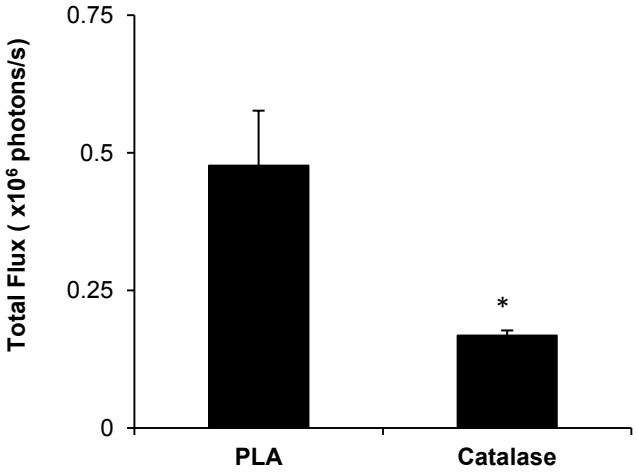


Figure 4.12 The effect of catalase on chemiluminescent signals of PLA-mediated inflammatory response. PLA were mixed with catalase or saline (as control) before subcutaneous implantation. Vertical lines denote ± 1SD (n = 3 in all cases). Significance vs. PLA: * $p < 0.05$.

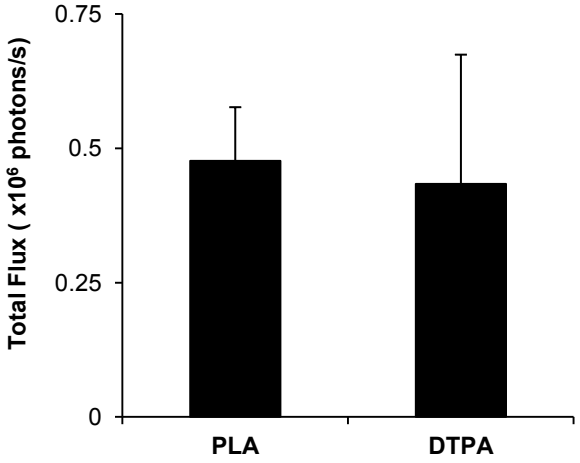


Figure 4.13 The effect of DTPA on chemiluminescent signals of PLA-mediated inflammatory response. PLA were mixed with DTPA or saline (as control) before subcutaneous implantation (n = 3). Vertical lines denote ± 1SD (n = 3 in all cases).

Despite the above results, it remained unclear whether other proinflammatory stimuli might have similar effects on L-012- mediated chemiluminescence. To test this, three different types of inflammatory models—LPS-mediated inflammation, histamine-induced inflammation, and medical device-associated tissue responses—were used. First, an LPS-mediated inflammation model was established as previously described [12, 87]. Briefly, LPS and saline, as a control, were injected subcutaneously, and then 100 µl of L-012 (15 mg/ml) was administrated intraperitoneally 24 hours after LPS/saline injection. It is well known that LPS administration can elicit acute inflammation and therefore increase ROS and reactive nitrogen species production by immune cells [181, 182]. Indeed, substantial L-012-mediated chemiluminescence signals were found at the site of LPS injection (Figure 4.14). The site with LPS treatment had a chemiluminescence intensity of $5.8\times10^8$ photons/s, whereas the control site with saline injection had an intensity of $8.8\times10^6$ photons/s. In a different model, dermal inflammation was induced by injection of compound 48/80, which causes histamine release from mast cells [183, 184] and the subsequent recruitment of PMNs [185, 186]. A substantial increase in the chemiluminescence signal (~8 times) was found in the region of compound 48/80 administration compared to controls (areas with saline injection; Figure 4.15).

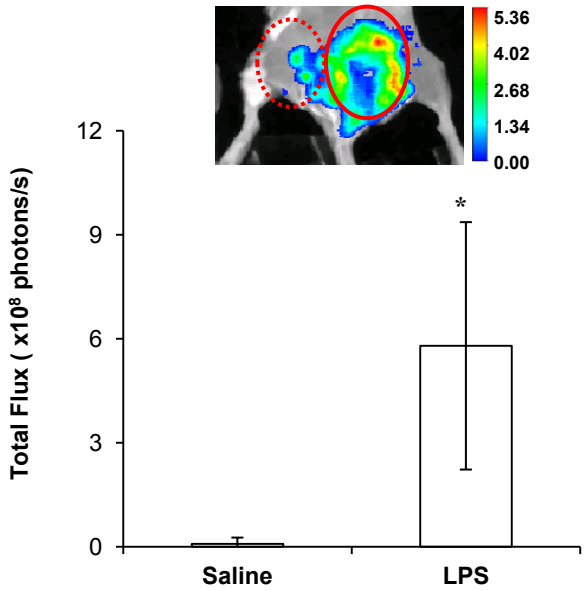


Figure 4.14 In the LPS-induced severe inflammation model, the L-012 was administered intraperitoneally 24 hours after a LPS subcutaneous injection. Representative whole body L-012-mediated chemiluminescence imaging and the average of L-012-mediated chemiluminescence signals were quantified and compared. Vertical lines denote ± 1SD (n = 6 in all cases). Significance vs. saline treatment: * p < 0.05.

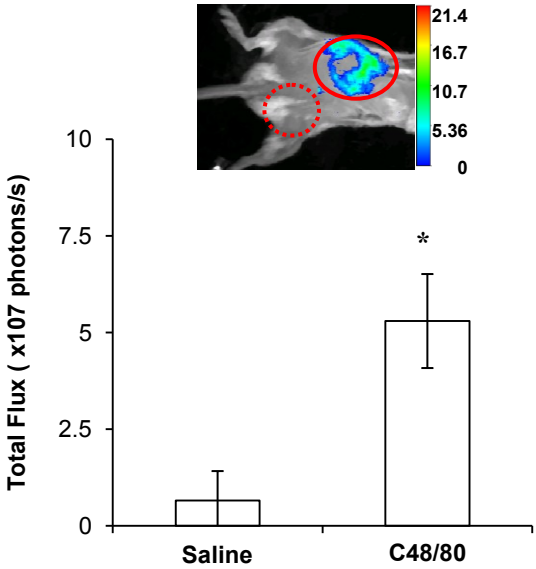


Figure 4.15 In the skin allergic response model, the L-012 was administered intraperitoneally 24 hours after subcutaneous injections of compound 48/80. Representative whole body L-012-mediated chemiluminescence imaging and the average of chemiluminescence signals were quantified and compared. Vertical lines denote ± 1SD (n = 6 in all cases). Significance vs. saline treatment: * P < 0.05.

To mimic foreign body reactions to medical devices, PU and H-PU catheters were implanted on the backs of Balb/c mice. Twenty-four hours after implantation, we measured L-012-mediated chemiluminescence. As expected, a relatively (3 times) strong signal was emitted from the PU implantation site compared to that from the H-PU catheter site, whereas sites of similar wounds (without implant placement) exhibited very weak chemiluminescence (Figure 4.16). Histological analysis of all three inflammatory models tested indicated that there was a good linear relationship between inflammatory responses (i.e., PMN recruitment) and L012-dependent chemiluminescence signals ($R^2$ =0.87, Figure 4.17).

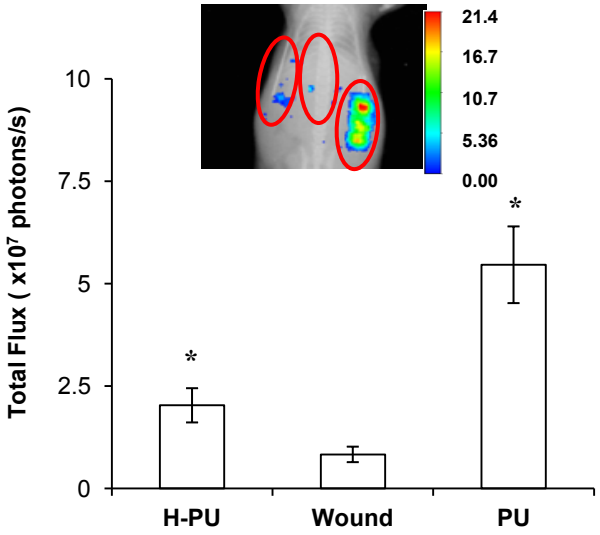


Figure 4.16 In catheter inflammation model, PU catheters and heparinized PU (H-PU) catheters were implanted subcutaneously on the backs of mice. L-012 was administered intraperitoneally 24 hours after catheter implantation. Representative whole body L-012-mediated chemiluminescence imaging and the average of chemiluminescence signals at different implant sites were quantified and compared. Vertical lines denote ± 1SD (n = 6 in all cases). Significance vs. wound treatment: * $p < 0.05$.

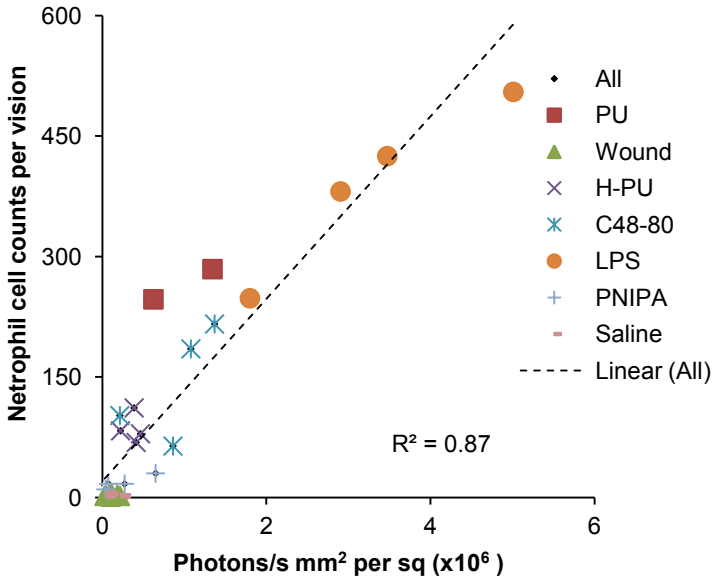


Figure 4.17 Correlation between L-012 mediated chemiluminescence signals (Figure 4.15) and neutrophil numbers at the inflamed sites induced by different types of inflammatory stimuli to subcutaneous space in the mouse back. The inflammatory cells counts per view field were quantified on H&E stained slides. The linear regression has coefficient $R^2 = 0.87$.

Subsequent studies were designed to test whether L-012- mediated ROS measurements might be used to assess the extent of inflammatory responses to materials known to have varying proinflammatory effects in vivo. Biomaterial implants trigger an array of foreign body reactions and recruited neutrophils play an important role in biomaterial-mediated acute inflammatory responses [73, 81, 108]. Three different types of polymeric particles made of PLA, PEG, and PNIPAM-$NH_2$ were used. Solutions (50 µl) of various implants (10% wt/vol), and saline as a control, were injected subcutaneously into the dorsal region of mice. One day after implantation, L-012- dependent chemiluminescence intensities at various implant sites were determined. Chemiluminescence varied in the following order: PNIPAM-$NH_2$ > PLA > PEG > saline control (Figure 4.18). Specifically, chemiluminescence intensities generated from PNIPAM-$NH_2$, PLA, and PEG implant sites were ~52, 16, and 4 times higher than that caused by saline injection alone. Histological evaluations also revealed that the trends of phagocyte (H&E staining) and PMN (IHC staining) recruitment are similar to those of the chemiluminescence intensities (Figure 4.19). The density of PMNs in tissue surrounding

PNIPAM-$NH_2$ implants were 3 and 6 times higher than those surrounding PLA and PEG particle implants, respectively.

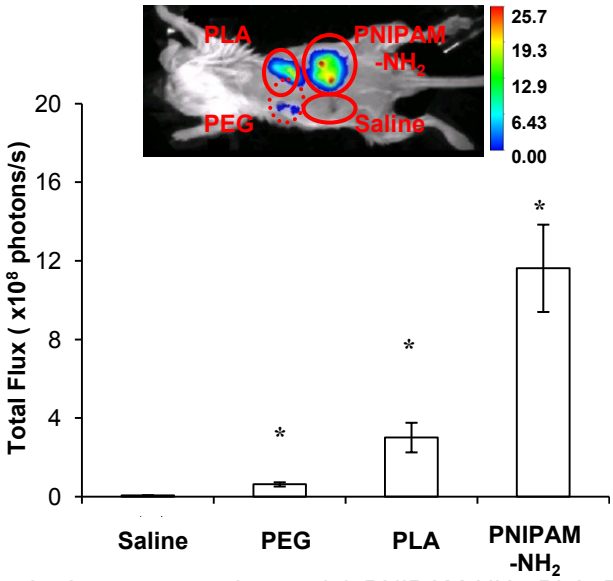


Figure 4.18 In a foreign body response mice model, PNIPAM-$NH_2$, PLA, PEG, and saline were implanted subcutaneously in the back of animals for 24 hours prior to L-012 intraperitoneal injection. The animal images were taken 30 minutes after L-012 administration. Representative whole body L-012 mediated chemiluminescence imaging and average of the chemiluminescence signals at different implantation sites were quantified and compared. Vertical lines denote ± 1SD (n = 6 in all cases). Significance vs. saline treatment: * $p<0.05$

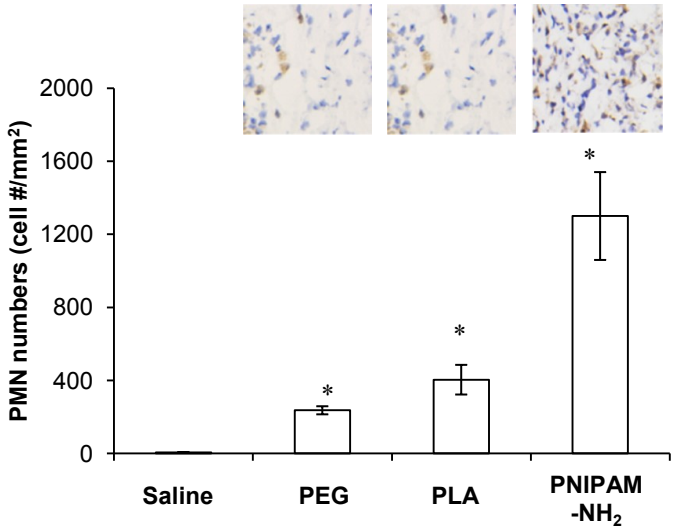


Figure 4.19 In a foreign body response mice model, PNIPAM-$NH_2$, PLA, PEG, and saline were implanted subcutaneously in the back of animals for 24 hours. Representative IHC (600×) stained slices and quantification of neutrophils numbers at different implant sites were quantified and compared. The cells counts per view field were quantified by ImageJ. Vertical lines denote ± 1SD (n = 6 in all cases). Significance vs. saline treatment: * $p < 0.05$.

There was a linear relationship between PMN number and L-012 chemiluminescence intensity (Figure 4.20). These results verify that L-012 chemiluminescence signal monitoring may be used to determine the extent of inflammatory responses to various inflammatory mediators in the same animal.

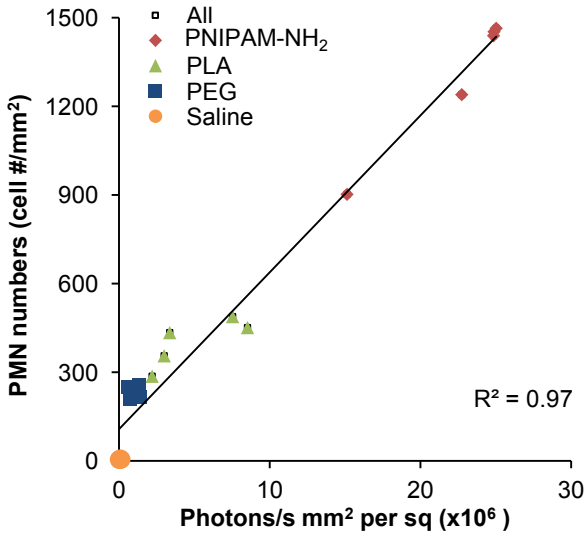


Figure 4.20 Correlation between L-012 mediated chemiluminescence signals (Figure 4.18) and neutrophil numbers (Figure 4.19) at various implant sites. The linear regression has coefficient $R^2 = 0.97$.

*4.2.4 Discussion and Conclusion*

Many ROS probes, including luminophores, chromogenic probes and fluorescent probes, have been developed to detect ROS activities in vitro and in vivo. In agreement with several recent findings, our results show that L-012 is a highly-sensitive ROS probe with a superior signal to noise ratio [68, 69], and is a reliable probe for noninvasive detection of ROS responses *in vivo* [58]. By comparison with luminol, a commonly-used chemiluminescence probe [168, 169], we find that L-012 emits a considerably stronger signal (~500 times higher), in agreement with a previous in vitro study [187]. The comparatively low chemiluminescence emission of luminol may be partially caused by the fact that the luminol signal is pH dependent showing a reduction at low pH, which often occurs at sites of inflammation [188].

L-012-dependent chemiluminescence signals have been used in an earlier study to detect inflammation-mediated ROS release *in vivo* [58]. However, it was not clear whether L-012-associated chemiluminescence signals might be used to monitor, and especially to quantify, the extent of inflammatory responses. Our *in vitro* cell culture and *in vivo* cell depletion studies have confirmed that activated PMNs are responsible for L-012-dependent chemiluminescence signals. These findings are in agreement with many previous observations. First, the accumulation of PMNs in tissue is a hallmark of inflammatory responses [8, 9, 189, 190]. Second, as part of the immune defense system's response to inflammation, recruited PMNs release a variety of ROS in response to inflammatory stimuli, including bacteria, infection, trauma, and implant-mediated inflammation [191]. Finally, PMN-derived myeloperoxidase is responsible for ROS production, since myeloperoxidase-knockout mice were found to cause reduced luminol-dependent chemiluminescence signals [169].

Our results show that L-012-dependent chemiluminescence signals can be used to detect and to assess the extent and kinetics of inflammatory reactions over time. Such real-time measurements cannot be achieved using conventional methods, including histological analyses and inflammatory marker measurements [192, 193]. Our results with biomaterial implants indicate that the strongest chemiluminescence signal appears at day 1 in agreement with earlier reports that PMN accumulation peaks 1-2 days after biomaterial implantation [26]. In addition, real time measurements allow us to assess the kinetics of inflammatory responses with a minimal number of animals. For example, while several groups of animals are needed for histological analyses for different time points, the use of L-012-dependent chemiluminescence measurements permits the measurement of inflammatory responses for all time points with one group of animals.

This study also explored the possibility of using L012-associated ROS measurements to quantify various other types of inflammatory responses. For that, infection- and allergy-mediated inflammatory responses were induced by subcutaneous injection of LPS (bacterial

toxin) and compound 48/80 (mast cell activator) [58, 119, 185, 186]. We find a significant increase of L-012-depedent chemiluminescence intensities at the injection sites of both types of inflammatory stimuli. These findings are supported by previous observations that PMNs quickly produce and secrete ROS after exposure to bacterial endotoxin, LPS, or compound 48/80 [182, 194]. In another model, we assessed ROS activities surrounding various intravenous catheters. Polyurethane (PU) catheters have been widely used in biomedical practice for drug administration, parenteral nutrition, fluid replacement and IV bags due to their excellent mechanical properties and low cell toxicity [195]. To improve their blood compatibility, heparinized PU catheters have been produced which have been shown to trigger substantially less inflammatory responses than uncoated catheters [196, 197]. Indeed, our results show that heparinized PU catheters prompt reduced ROS activities compared to uncoated catheters. Furthermore, rather importantly, we find that there is a good relationship between chemiluminescence signals and different types of inflammatory responses in vivo. Overall, these results support the conclusion that L012-associated ROS measurements can be used to continuously monitor the kinetics of acute inflammatory reactions in various inflammatory disease models.

Finally, it is well documented that biomaterial implants prompt varying inflammatory responses [108]. By testing three different types of polymeric particles (PLA, PNIPAM-$NH_2$ and PEG) with different biocompatibilities [127, 198], our studies show that there is a very good linear relationship between chemiluminescence intensities and histological inflammatory measurements. As expected, the stronger inflammatory reactions are accompanied with higher L-012-dependent chemiluminescence intensities. These results demonstrate that L-012 can be utilized as a powerful tool to assess the biocompatibility of various biomaterials. By measuring the *in vivo* generation of ROS, it may be possible to assess multiple implants in a single mouse, thereby eliminating the variation in immune reactions between animals. These quantitative measurements may not be possible using less sensitive ROS probes, such as luminol [170].

In conclusion, our studies have established that L-012-mediated chemiluminescence imaging can serve as a promising tool for *in vivo* examination of ROS mediated activities. The advantages of this method over traditional techniques include simplicity, low cost, continuous measurements, and reduced animal numbers. Finally, this novel technique could provide in-depth and quantitatively perceptive insights on different treatments for altering immune reactions in vivo.

## 4.3 Real-time monitoring of *in vivo* inflammatory responses using pH ratiometric fluorescence imaging probe

### *4.3.1 Purpose*

Inflammatory cellular responses and the associated products will lead to tissue acidosis and cell death in the surrounding tissue in most inflammatory diseases. High hydrogen ion concentrations have been found in inflamed tissue (down to pH 5.4), in fracture-related hematomas (down to pH 4.7), in cardiac ischemia (down to pH 5.7) and in and around malignant tumors [19, 20]. Many papers suggest that the acidification of diseased tissues is likely caused by cell death and inflammatory cell products such as ROS, hypochloric acid (HOCl), and $H_2O_2$ [21, 199, 200]. However, very few studies have been developed to determine tissue acidosis in order to assess the inflammatory response. Although several pH sensitive dyes have been developed [201, 202], these dyes cannot be used *in vivo* due to the diffusion of the dyes in and out of cells and tissues at different rates. The study proposed here is aimed at developing new methods to determine and quantify the pH changes in and surrounding inflamed tissues.

### *4.3.2 Material and Methods*

#### 4.3.2.1 Materials

N-isopropylmethyacrylamide (NIPAM) and 2,2'-azobis (2-methylpropionamidine) dihydrochloride (V50) were purchased from Aldrich Co. *N,N'*-Methylenebisacrylamide (BIS) was obtained from Bio-Rad Laboratories. *N*-(3-aminopropyl) methacrylamide hydrochloride (APMA) was purchased from Polysciences Co. CypHer 5E NHS ester was purchased from GE

Healthcare Life Sciences. Oyster®-800 dye was purchased from Boca Scientific Inc., FL and silicon oxide nanospheres ($SiO_2$, 30 nm diameter) were purchased from Sun Innovations Inc.(Fremont, USA). All chemicals were used without purification.

4.3.2.2 Preparation of PNIPAM-CypHer5E-Oyster800 probes

PNIPAM particles were prepared using a precipitation polymerization method [23]. The sample was lyophilized and stored at 4-8 °C for further use. PNIPAM spheres (4 mg/ml) were then suspended in sterilized PBS/0.5M sodium carbonate solution (pH 8.3) and then mixed with CypHer 5E NHS ester (1 mg/ml). Following overnight reactions at room temperature, the CypHer5E-labled PNIPAM spheres were dialyzed against sterilized DI water, lyophilized and then re-suspended in PBS buffer (10ml, pH 7.4). Oyster800 TFP ester (0. 5 mg/ml) was added and reacted with CypHer5E-labled PNIPAM spheres in the dark at room temperature. Following dialysis with DI water in the dark, PNIPAM-CypHer5E-Oyster800 pH probes were lyophilized and stored at 4-8 °C for further use. Following the dye manufacturer's instructions, we determine that the concentration of both CypHer5E and Oyster800 dyes in pH probes were $4.49x10^{-10}$ and $1.79x10^{-10}$ mole/mg particle, respectively. The illustration of PNIPAM-CypHer5E-Oyster800 is shown in Figure 4.21.

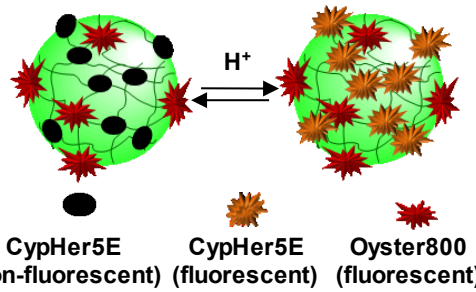


Figure 4.21 Schematic illustration of PNIPAM-CypHer5E-Oyster800 pH probes.

4.3.2.4 Ratiometric pH measurements and imaging *in vitro*

The pH-dependent response of the PNIPAM-CypHer5E-Oyster800 probes was determined based on the ratio of the fluorescence emission bands of the Oyster800 (830 nm) and CypHer5E fluorophores (700 nm) in a series of phosphate/citric acid buffer solutions

ranging from pH 4.4 to 9.0 using a fluorescence spectrometer (Shimadzu RF-5301PC, Japan). Similar calibration was also done using KODAK in vivo FX Pro (Kodak, USA). For the imaging analyses, CypHer5E was excited at 630nm and the fluorescence emission wavelength was 700nm, whereas Oyster800 was excited at 760nm and the fluorescence emission wavelength was 830nm (f/stop, 2.5; 4 × 4 binning).

4.3.2.5 Measurement of pH by microelectrode

To observe the relationship between our ratiometric imaging and the pH measurements in the phantom surface of different depths, the pH measurements were performed after each *in vitro* experiment using an Accumet pH meter (Fisher Scientific, Basic model) equipped with a glass microelectrode probe, MI-431 (Microelectrodes, Inc., Londonderry, NH) [172]. The microelectrode probe was inserted into the phantom surface to record the corresponding pHs. The tissue pHs were also measured interstitially with a pH microelectrode (M1-431) connected to a Accumet pH meter.

4.3.2.6 Ratiometric pH imaging of inflammatory responses *in vivo*

All animal inflammatory and kidney ischemic studies were performed on Balb/c mice while cancer work was carried out using C57 mice. All animals (Female, 20-25 gram body weight) were purchased from Taconic Farms, Inc. (Germantown, NY) and housed in the Animal Care Facility, University of Texas at Arlington. All studies were performed in accordance with the approved animal protocol. To assess the extent of inflammatory responses following $SiO_2$ implantation, $SiO_2$ nanoparticle dispersions (1.5 mg to 8 mg of 10% w/v) were injected subcutaneously via 21 gauge needles on the back of Balb/C mice (n = 6). For the anti-inflammatory response study, $SiO_2$ dispersion (8mg, 10% w/v) was injected subcutaneously with and without dexamethason (2mg/80µl/site). To test the extent of inflammatory responses to different nano- and micro-materials, saline (75 µl) or nano- and microspheres (75 µl, 10% w/v), including $SiO_2$ nanospheres, polystyrene microspheres (200 nm diameter) [203], and polyethylene glycol (200 nm diameter) [204] were subcutaneously injected (n = 6). For all

testing, PNIPAM-CypHer5E-Oyster800 probes (0.1mg, 2% w/v) were mixed with test materials prior to implantation. Our control studies have shown that the small amount of the pH probes used in this work would have insignificant effect on the overall inflammatory responses to material implants. For the kidney ischemia model, Balb/C mice underwent surgical procedures as previously described (n = 3) [205]. Briefly, one kidney per animal was cross-clamped for 30 minutes prior to reperfusion. Thirty minutes after the completion of the surgical procedure, the animals were injected PNIPAM-CypHer5E-Oyster800 probes (100μl) intravascularly. To induce tumorigenesis, C57 mice were subcutaneously implanted with mouse B16F10 tumor cells ($10^6$ cells + 0.1 mg pH probe/0.1 ml per site) and saline (0.1 mg pH probes/0.1 ml saline per site) (n = 3). For imaging analyses, animals were anesthetized by isoflurane inhalation and then imaged by the KODAK In vivo FX Pro (Kodak, USA). Mice were imaged for the CypHer5E and Oyster800 channels (f/stop, 2.5; 4 × 4 binning) at the specified time points.

4.3.2.7 Histological analysis and inflammatory cell quantifications

At the end of the studies, the test animals were sacrificed and the implantation sites/inflamed tissues were isolated for histological analyses. All tissues underwent cryosection and H&E staining and also CD11b+ staining. All histological sections were imaged under a Leica DMLP microscope (Leica, Wetzlar, Germany) equipped with a Qimaging RetigaExi 1394 digital camera (Qimaging, Surrey, British Columbia, Canada).

4.3.2.8 Data Analyses

For *In vitro* study, the fluorescence spectra are recorded using a fluorescence spectrometer (Shimadzu RF-5301PC, Japan). The ratios of the average fluorescence intensities between CypHer5E (pH-sensitive dye, with average fluorescence intensities from 670 nm to 730 nm) and Oyster800 (pH-insensitive dye, with average fluorescence intensities from 800 nm to 860 nm) were also calculated to provide quantitative measurement of pH. To investigate the correlation between pH and values, these two values were correlated using linear regression

analysis. The same *in vitro* studies and *in vivo* are imaged by KODAK in vivo FX Pro (Kodak, USA). The fluorescence intensities were measured at both channels at emission of 700nm (excitation at 630 nm) and 830nm (excitation at 760 nm). The ratiometric images, CypHer5E/Oyster800, were calculated after background correction. Polygon ROIs were drawn over the inflammatory locations in the fluorescence images at both channels and also ratiometric images. The mean fluorescence intensities or ratios for all pixels in the fluorescence images or pH ratiometric images were calculated using Carestream Molecular Imaging Software, Network Edition 4.5 (Carestream Health). The ratio data were then converted into estimated pH values for *in vivo* calibrations [206].

Quantitative histological analysis of the total number of inflammatory cells throughout the implantation site was performed using ImageJ. The estimated total inflammatory cells were calculated using an algorithm modified from literature [206]. All the areas of interests were counted in one section every 288μm and the volume calculated using the following formula:

$$\hat{\mathrm{V}} = T \cdot \frac{a}{p} \cdot \sum_{i=1}^{\mathrm{m}} \mathrm{P_i} \qquad (1)$$

Where $\mathbf{P}_i$ is the number of points landing within the object on the *i*th section, ***T*** is the distance between analyzed sections and ***a/p*** is the area associated with each point. To determine the amount of cells per volume, the same sections were used. A physical dissector was made with two subsequent sections. A counting frame and meander sampling were used to estimate the numerical density of cells using the following formula:

$$\widehat{\mathrm{N_v}} = \frac{1}{a/f \cdot h} \cdot \frac{\sum Q^-}{\sum P} \qquad (2)$$

Where $\widehat{\mathbf{N}_\mathbf{v}}$ is the estimate of numerical density, ***a/f*** the area of the frame, ***h*** the dissector height, **ΣQ** the total amount of cells counted and **ΣP** the sum of frame-associated points hitting the reference volume. The estimate of the total number of cells in the inflammation site was the product of the volume $\hat{\mathbf{V}}$ and the amount of cells per volume, $\widehat{\mathrm{N_v}}$.

Finally, to investigate whether *in situ* pH values can be used to assess the extent of inflammatory responses *in vivo*, the *in vivo* pH values and estimated total inflammatory cell numbers were correlated using linear regression analysis.

4.3.2.9 Statistical analysis

Results were expressed as mean ± standard deviations**.** Two-way analysis of variance (ANOVA) and Student's t-test was performed to compare the differences between groups and $p \leq 0.05$ is considered as significant.

*4.3.3 Results*

4.3.3.1 Optical properties of the dual fluorochrome pH-probes

The dye-conjugated pH probes were subsequently tested for their pH sensitivities *in vitro*. By scanning the fluorescence spectrum of the probes at pH values between 5.20 and 7.55, we find two distinct and separate peaks. The lower-wavelength peak shared an identical spectrum with CypHer5E (maximal at ~670 nm) and the higher-wavelength peak is derived from Oyster800 (maximal at ~794 nm) (Figure 4.22a). The spectra were recorded at different pH values. By varying pH from 4.4 to 9.0, the average fluorescence intensities from 670 nm to 730 nm were substantially decreased whereas the average fluorescence intensities from 800 nm to 860 nm were unchanged throughout the pH range (the wavelengths were chosen in order to compare the results from the KODAK *in vivo* machine) (Figure 4.22b). The ratios of the average fluorescence intensities between CypHer5E (pH-sensitive dye, with average fluorescence intensities from 670 nm to 730 nm) and Oyster800 (pH-insensitive dye, with average fluorescence intensities from 800 nm to 860 nm) were also calculated to provide quantitative measurement of pH in an aqueous environment. Interestingly, the ratios of the average fluorescence intensities had a strong correlation with pH values from 5.53 to 7.55 (Ratio = -0.692 x pH + 5.439, $R^2$ = 0.99). These two wavelength ranges were used to generate the quantitative data in the following studies.

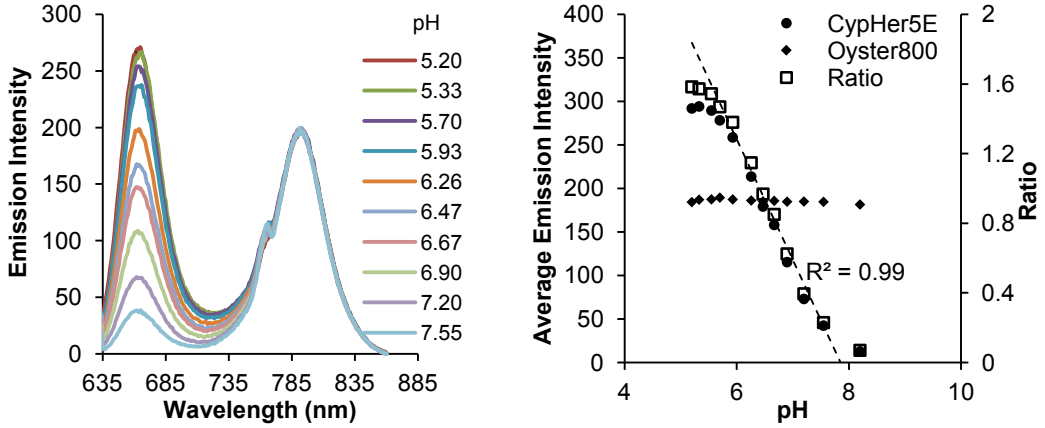


(a) (b)

Figure 4.22 Characterization of the optical property of pH probes based on fluorescence spectrometer. (a) Emission spectra of dye-labeled particles at different pHs were measured based on fluorescent spectrum. (b) Average emission intensities CypHer5E (from 670 nm to 730 nm) and Oyster800 (from 800 nm to 860 nm) were calculated. The ratios of CypHer5E vs. Oyster800 from pH probes at different pHs were also quantified. The correlation of pHs and ratios was also applied, the linear regression has coefficient $R^2$ = 0.99.

4.3.3.2 Ratiometric imaging and quantification data with pH probes *in vitro*

The pH probes were subsequently tested for their ratiometric imaging capability. Using pH probes to measure various pH levels in solution, we observed drastic changes in pH ratiometric imaging *in vitro* correlating with the change of pH from 4.40 to 9.00 (Figure 4.23a). There was an almost linear relationship between the florescence intensity ratios and pH values from 5.78 to 7.65 (Ratio = -3.629* pH + 28.103, $R^2$ = 0.97) (Figure 4.23b).

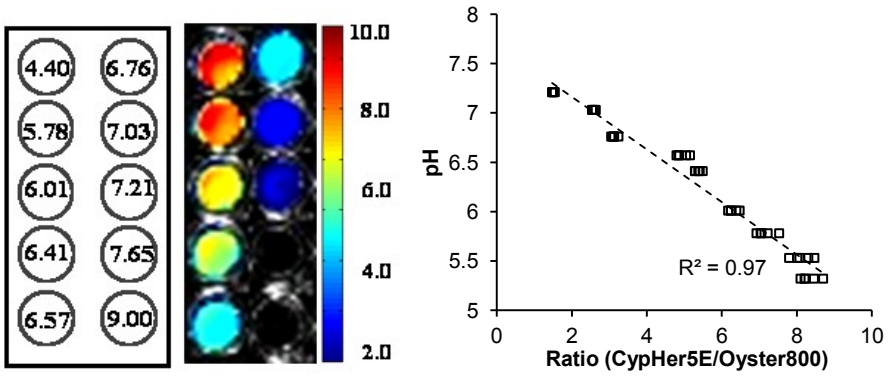


(a) (b)

Figure 4.23 Characterization of the optical property of pH probes based on KODAK in vivo FX. (a) The representative merged ratiometric and white light images of pH probes at different known pHs; (b) Correlation between fluorescence ratios of CypHer5E/Oyster800 recorded in the images and different known pHs. All experiments were carried out with 0.5 mg/ml pH probes.

A series of experiments were then carried out to test the sensitivity and accuracy of the pH probes both *in vitro* and *in vivo*. By adding different concentrations (0.8 - 2.0% w/v) of the pH probes into pH 6.76 solutions, we observed an increase in fluorescent intensities at both wavelengths (Figure 4.24a). However, the ratios of both fluorescent peaks were nearly constant at ~4.58 fold, independent to the probe concentrations *in vitro* (Figure 4.24b). We next assessed whether the ratio of CypHer5E and Oyster800 fluorescence could correctly measure the pH at different depths in skin phantoms. For that, different thicknesses (2-8 mm) of the skin phantoms were placed between the same amount (1.0% w/v) of pH probes and the light source. Indeed, the fluorescence intensities decreased with increasing skin phantom thickness. Nevertheless, the ratio of both fluorescent intensities at different pHs was nearly constant regardless of skin phantom thickness (2 to 8 mm) (the CypHer5E/Oyster800 ratio is 5.32 at pH = 5.53, 4.15 at pH = 6.01, 3.16 at pH = 6.76, Figure 4.25a, b). Moreover, similar experiments were carried out by comparing the pH values, measured using a microelectrode probe and ratiometric imaging techniques (Table 4.1).

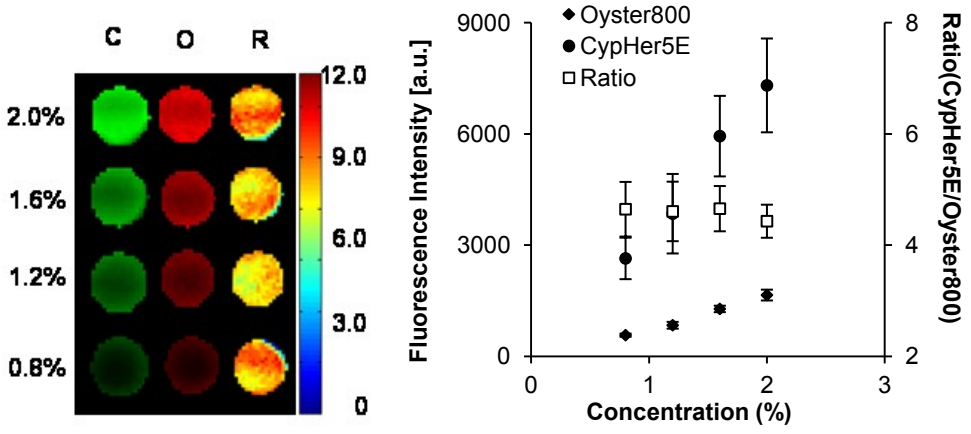


(a) (b)

Figure 4.24 Interference of different concentrations of pH probes for fluorescence images from CypHer5E (700±30 nm) and Oyster800 (830±30 nm) channels, and pH ratiometric imaging *in vitro.* (a) The NIR fluorescence images of the CypHer5E (C, green-coded) and Oyster800 channels (O, red-coded) and resulting ratio of CypHer5E/Oyster800 (R, color-coded) of wells containing different concentrations (0.8% to 2%) of pH probes; (b) The average fluorescence intensities and ratios of fluorescence intensities at different concentrations performed by region of interest from images from (a). Vertical lines denote ± 1SD (n = 5 in all cases).

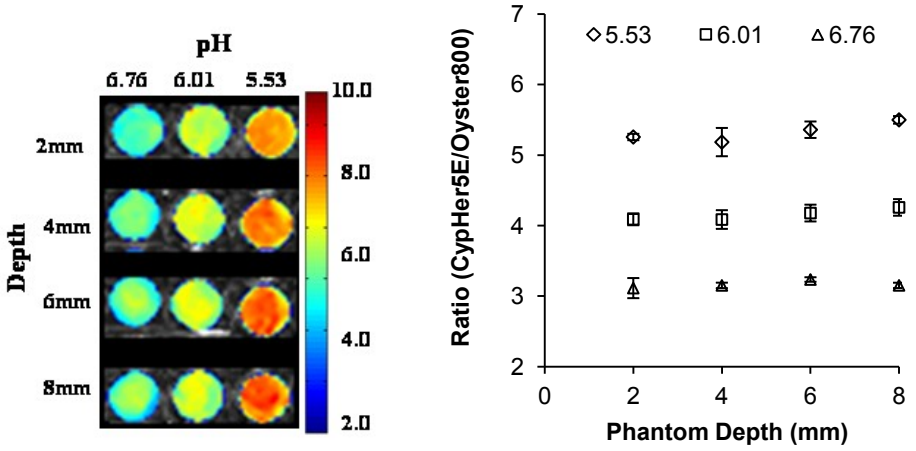


(a) (b)

Figure 4.25 Interference of tissue depth of pH probes for fluorescence images from CypHer5E (700±30 nm) and Oyster800 (830±30 nm) channels, and pH ratiometric imaging *in vitro.* (a) The NIR fluorescence images of the CypHer5E (C, green-coded) and Oyster800 channels (O, red-coded) and resulting ratio of CypHer5E/Oyster800 (R, color-coded) of wells containing different phantom depths (2mm to 8mm) at different pHs, (b) The average ratios of fluorescence intensities at performed by region of interest from images from (a). Vertical lines denote ± 1SD (n = 5 in all cases).

Table 4.1 Comparison of the ratiometric imaging data, estimated pHs and the pH measurements by microelectrode

| Different pH | Different depth (mm) | Ratio | Estimated pH | Microelectrode probe |
|---|---|---|---|---|
| #1 (~6.00) | 2 | 6.16 ±0.23 | 5.98 ±0.05 | 5.95 ±0.05 |
| | 4 | 6.48±0.27 | 5.91 ±0.08 | 5.91±0.01 |
| | 6 | 6.47±0.16 | 5.92 ±0.05 | 5.93±0.03 |
| | 8 | 6.54±0.27 | 5.89±0.08 | 5.92 ±0.04 |
| #2 (~6.50) | 2 | 5.85±0.13 | 6.26±0.04 | 6.34±0.08 |
| | 4 | 5.58±0.20 | 6.36 ±0.06 | 6.45±0.02 |
| | 6 | 5.43 ±0.19 | 6.41 ±0.06 | 6.47 ±0.01 |
| | 8 | 5.34 ±0.25 | 6.42 ±0.08 | 6.52±0.06 |
| #3 (~7.00) | 2 | 3.38 ±0.17 | 6.87 ±0.05 | 6.95 ±0.01 |
| | 4 | 3.53 ±0.10 | 6.83 ±0.03 | 6.98 ±0.03 |
| | 6 | 3.56±0.20 | 6.82±0.06 | 6.96 ±0.02 |
| | 8 | 3.85±0.11 | 6.73±0.03 | 6.84±0.03 |

The correlation coefficient between the pH levels measured by the microelectrode probe and the estimated pH from the ratiometric imaging was 0.89 (Figure 4.26). Furthermore, by subcutaneously injecting different amounts of the pH probes, we found that the ratio of CypHer5E/Oyster800 is nearly constant at ~2.40 *in vivo* at pH = 7.4 (Figure 4.27).

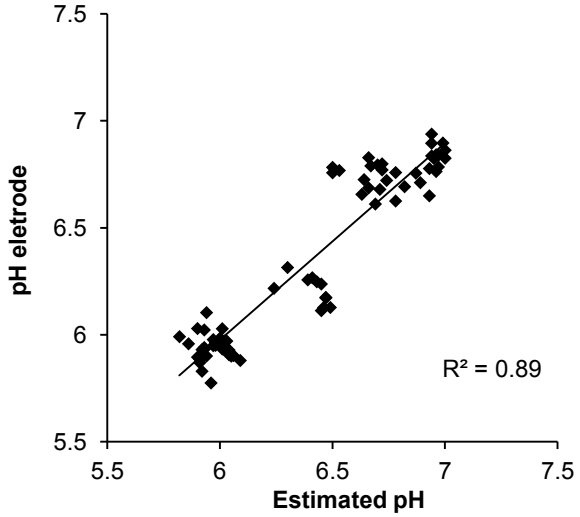


Figure 4.26 Correlation between pH measured by electrode and the estimated pHs from the ratiometric imaging at different pH.

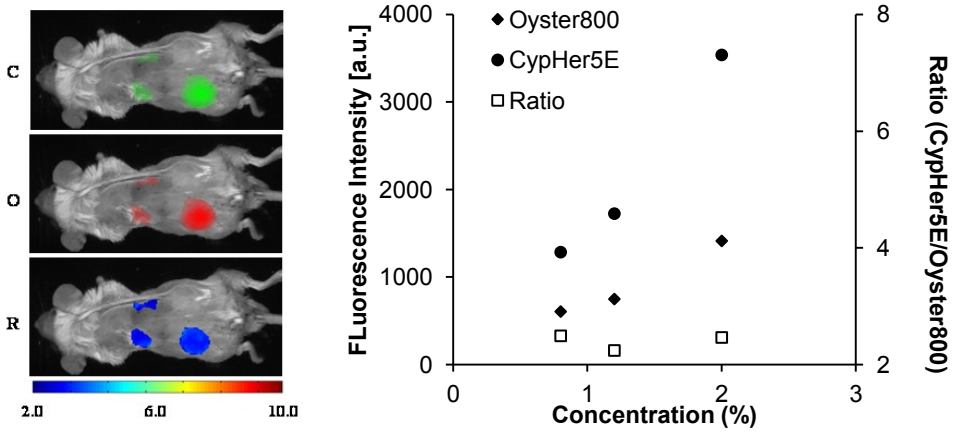


(a) (b)

Figure 4.27 Interference of containing different concentrations of pH probes for fluorescence images from CypHer5E (700±30 nm) and Oyster800 (830±30 nm) channels, and pH ratiometric imaging *in vivo.* Different concentration of pH probes were injected subcutaneously at pH = 7.4. (a) The NIR fluorescence images of the CypHer5E (C, green-coded) and Oyster800 channels (O, red-coded) and resulting ratio of CypHer5E/Oyster800 (R, color-coded) at different concentrations (0.8% to 2%) of pH probes, (b) The average fluorescence intensities and ratios of fluorescence intensities at different concentrations.

4.3.3.3 Ratiometric imaging and quantification of pH changes *in vivo* and correlations with histological results

The pH probes, PNIPAM-CypHer5E-Oyser800, were tested for their ability to monitor pH changes and associated inflammatory responses *in vivo* using a biomaterial implantation model [207, 208]. Briefly, different amounts of $SiO_2$ (30 nm diameters), ranging from 1.5 to 8.0 mg, were mixed with 0.1 mg PNIPAM-CypHer5E-Oyser800 and were then implanted subcutaneously via 21 gauge needles in the dorsal region of mice. Ratiometric images of the animals following implantation were taken at different time points from 15 minutes to 24 hours as shown in Figure 4.28a. As expected, the fluorescence intensity ratio increased with increasing concentrations of nanoparticles. Interestingly, the ratiometric values associated with 8.0 mg and 4.0 mg of $SiO_2$ implants achieve a plateau within 6 hours while the ratiometric values obtained with 1.5 mg $SiO_2$ implants continuosly increased for at least 24 hours (Figure 4.28b). Following 24 hour implantation, our results show that the implantation site of 8.0 mg $SiO_2$ (pH 6.49 ± 0.03) had substantially lower pH than the tissues implanted with 4.0 mg and 1.5 mg $SiO_2$ (pH 6.55 ± 0.04 and 6.85 ± 0.09, respectively) ($p < 0.05$).

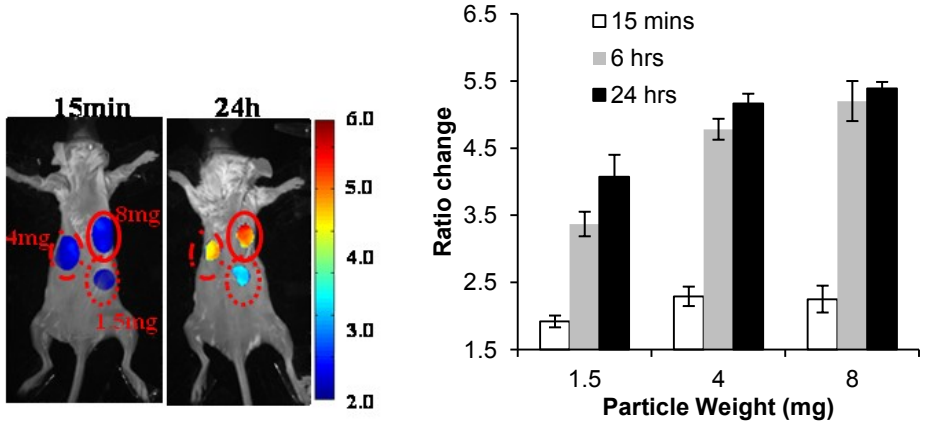


(a) (b)

Figure 4.28 In a foreign body response mice model, different amounts of $SiO_2$ (30 nm diameters, 1.5 - 8.0 mg) were mixed with pH probes and implanted subcutaneously in the back of animals. (a) The representative merged ratiometric images and white light images shows the ratio changes in the $SiO_2$ implanted sites at different time points. (b) the averages associated ratio changes in areas implanted with different amounts 1.5, 4, 8 mg of $SiO_2$ nanospheres were quantified after implantation from 15 minutes to 24 hours. Vertical lines denote ± 1SD (n = 6 in all cases).

Furthermore, we quantified the total number of implant-associated inflammatory cells by compiling different tissue sections throughout the implant sites using MATLAB® software. We find that, as expected, increasing doses of $SiO_2$ led to increasing numbers of inflammatory cells. Most importantly, by correlating the number of inflammatory cells with the ratiometric imaging data, we find that there is a near perfect linear relationship ($R^2$ =0.96 in H&E versus pH change) (Figure 4.29).

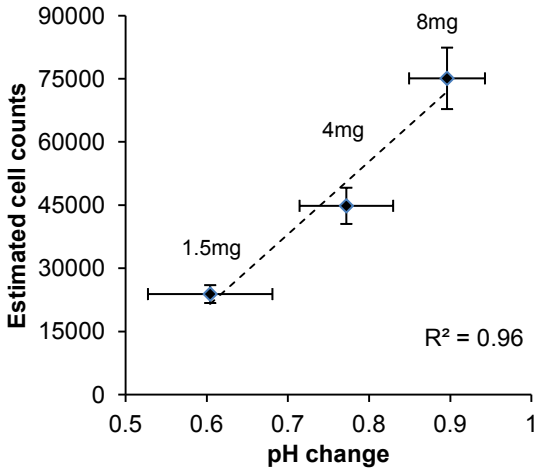


Figure 4.29 Correlation between associated pH changes calculated from Figure 4.30 by calibration curve and inflammatory cell counts from H&E stained slices at different amounts (1.5 – 8 mg) of $SiO_2$ implant sites. Quantitative histological analysis of the total number of inflammatory cells throughout the implantation site was performed using ImageJ. Vertical and parallel lines denote ± 1SD (n = 6 in all cases). The linear regression has coefficient $R^2$= 0.92 and is statistical significant at $p<0.05$.

4.3.3.4 Effect of anti-inflammatory agents on pH change at the implant site

To investigate whether pH ratiometric images can be used to monitor changes in the inflammatory process in real time, measurements were carried out on $SiO_2$ nanosphere implants in animals with or without anti-inflammatory agent - Dexamethasone (DEX) treatment. DEX has been shown to reduce a wide variety of the inflammation response *in vivo* [209, 210]. In this experiment, mice were implanted with 8.0 mg $SiO_2$ suspended in either saline or saline with DEX (2.0mg/site) as shown in Figure 4.30a. Treatment with DEX reduced the pH changes at all time points tested. The tissue pH values were 6.72 ± 0.05 without DEX treatment and 7.05 ± 0.04 with DEX treatment at day 3 (Figure 4.30b).

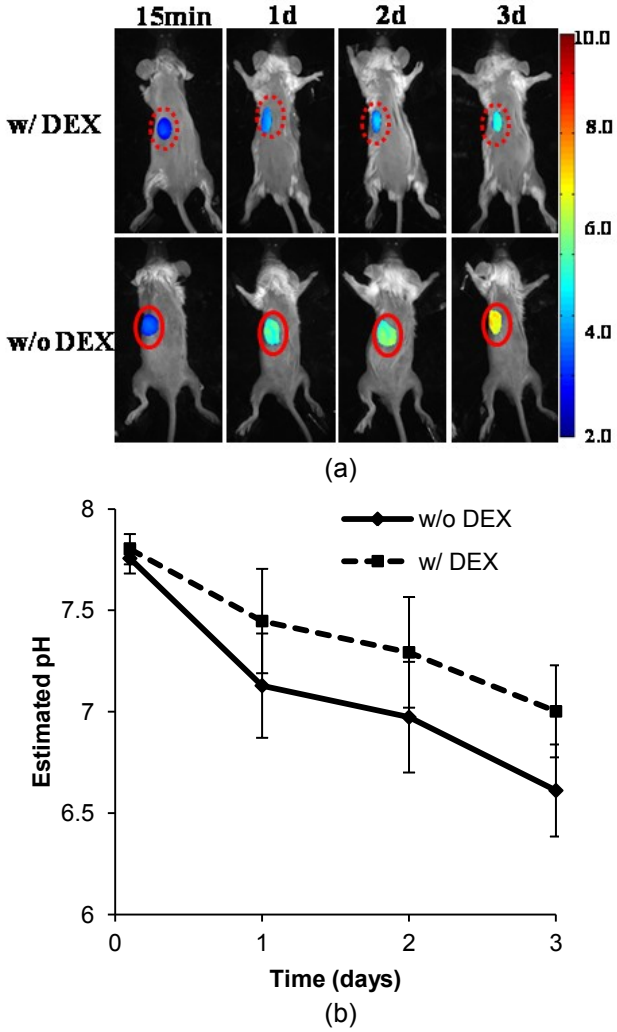


Figure 4.30 The effect of DEX treatment on the ratiometric imaging at different time points. 8.0 mg of $SiO_2$ were mixed with pH probes and implanted subcutaneously in the back of animals with and without DEX treatment. (a) The representative merge ratiometric image and white light images showed the ratio changes, and (b) the average estimated pH were calulated from the ratio by applying the calibration curve at different treatment at different time points. Vertical lines denote ± 1SD (n = 6 in all cases)

Histological analyses shows increased inflammatory cell accumulation at the implantation site in control animals in comparison to DEX treatment (Figure 4.31a). Finally, as above, there was a close correlation between pH values and inflammatory cell numbers in the tissues (Figure 4.31b).

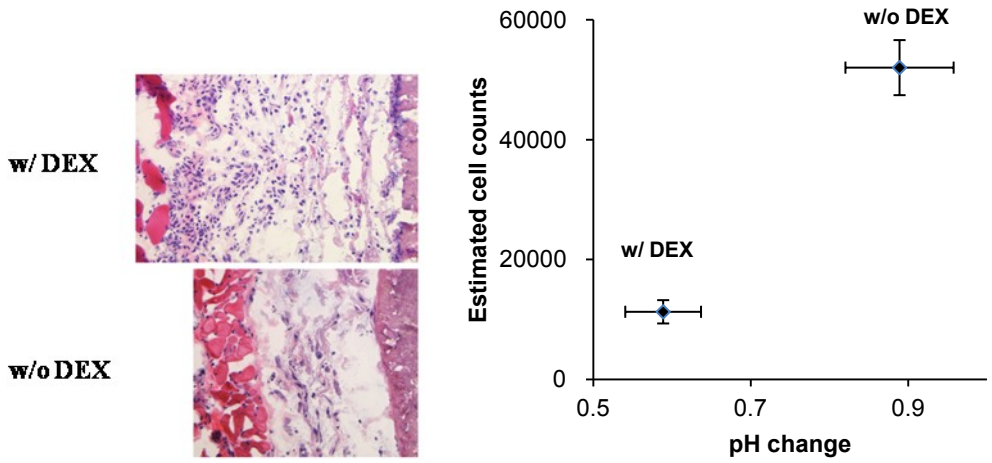


(a) (b)

Figure 4.31 The effect of DEX treatment in the foreign body responses. 8.0 mg of $SiO_2$ were mixed with pH probes and implanted subcutaneously in the back of animals with and without DEX treatment. (a) Representative H&E (200×) stained slices with and without DEX treatment, and (b) correlation between associated pH changes (Figure 4.30b) and inflammatory cell counts from H&E stained slices at $SiO_2$ implant sites with and without DEX tratment. Quantitative histological analysis of the total number of inflammatory cells throughout the implantation site was performed using ImageJ. Vertical and parallel lines denote ± 1SD (n = 6 in all cases).

4.3.3.5 Quantification of inflammatory reactions induced by different types of implants

It is well established that various types of biomaterials prompt different localized inflammatory responses or foreign body reactions [203, 207]. To determine whether pH probes might be used to monitor the extent of foreign body reactions, spheres made of different materials were implanted subcutaneously with pH probes on the back of animals. Ratiometric images of various implants (8 mg materials/site) were taken at different time points from 15 minutes to 7 days (Figure 4.32a). The mean ratiometric change for all implantation sites at each time point was measured. Among all test materials, $SiO_2$ triggered the strongest ratiometric change 15 minutes after implantation and continued to increase with time. On the other hand, saline injected sites exhibited minimal or no significant ratiometric changes (Figure 4.32b). At day 7, all four materials triggered varying ratiometric changes in the order: silicon dioxide nanospheres ($SiO_2$) > polystyrene nanospheres (PS) > polyethylene glycol nanospheres (PEG) > saline. Specifically, we find that the $SiO_2$ implantation site has a pH of 5.77 ± 0.07, polystyrene has a pH of 6.72 ± 0.05, PEG nanospheres have a pH of 7.11 ± 0.05 and the

saline-injected control tissue has a pH of 7.30 ± 0.13 (Figure 4.32c). The extent of the inflammatory response associated with 7-day implants and controls was also examined by H&E staining (Figure 4.33a). The total inflammatory cell numbers of the four materials after 7-day implantation from H&E (Figure 4.36a) and CD11b+ staining (Figure 4.33b) were also calculated. In agreement with previous findings, we find a good positive linear relationship between pH and total cell numbers from H&E staining ($R^2$ = 0.97) (Figure 4.34a) and CD11b+ staining ($R^2$ = 0.91) (Figure 4.34b).

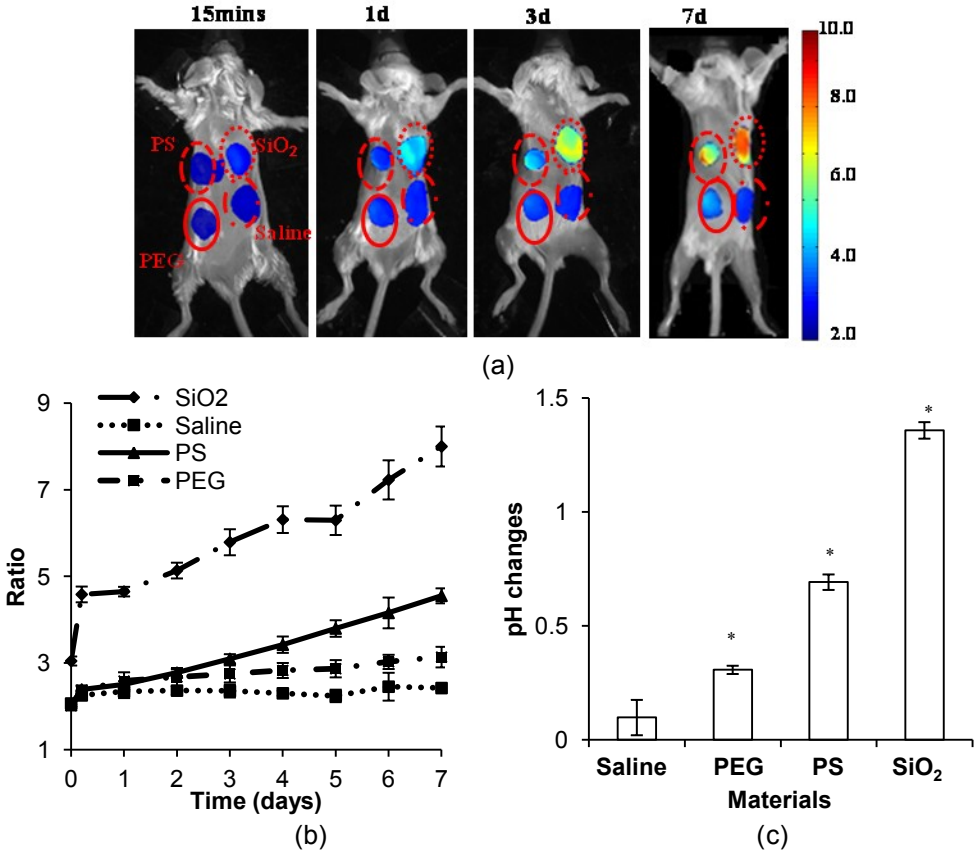


Figure 4.32 In a foreign body response mice model, $SiO_2$, PLA, PEG, and saline were mixed with pH probes and implanted subcutaneously in the back of animals. (a) The merged ratiometric imaging of mice implanted with different implantation sites of $SiO_2$, PS, PEG or saline (as control) at different time points (15 minutes, 1, 3, 7 days after implantation). (b) The average ratiometric changes of the different implantation sites at different time points were quantified and compared. (c) Values of *in situ* pH change at different implantation sites on day 7 were quantified and compared. Vertical lines denote ± 1SD (n = 6 in all cases). Significance vs. saline treatment: * $p < 0.05$.

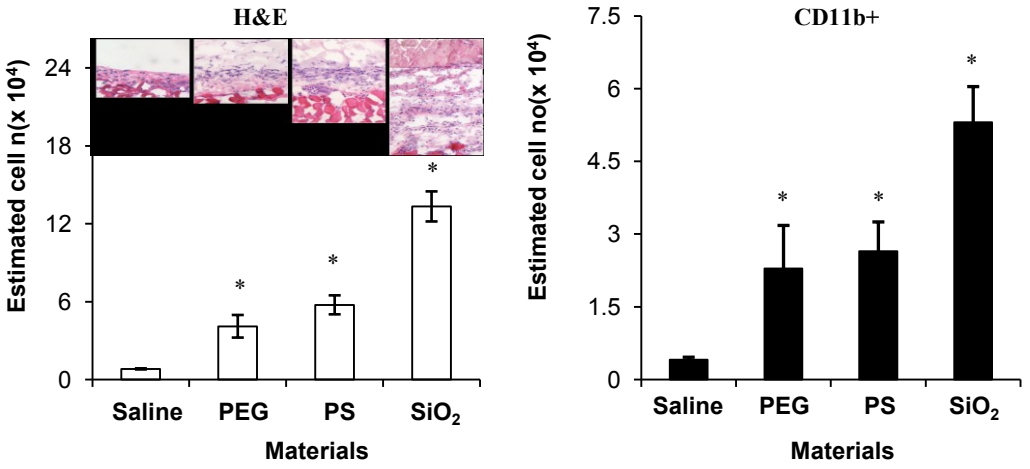


(a) (b)

Figure 4.33 In a foreign body response mice model, $SiO_2$, PLA, PEG, and saline were mixed with pH probes and implanted subcutaneously in the back of animals following 7 days implantation. (a) Representative H&E images and numbers of inflammatory cells based on H&E staining at the implant sites, (b) numbers of CD11b+ inflammatory cells at the implant sites. Quantitative histological analysis of the total number of inflammatory cells throughout the implantation site was performed using ImageJ. Vertical lines denote ± 1SD (n = 6 in all cases). Significance vs. saline treatment: * $p < 0.05$.

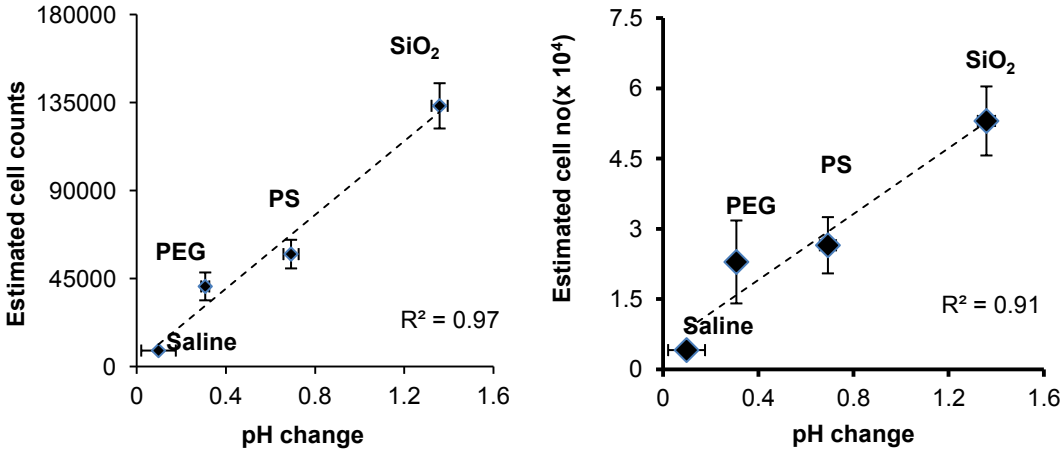


(a) (b)

Figure 4.34 Correlation between associated pH changes (Figure 4.32b) and estimated H&E inflammatory cell counts (a, from Figure 4.33a) and estimated CD11b+ inflammatory cell (b, from Figure 4.33b) at different implantation site of $SiO_2$, PLA, PEG, and saline. Vertical and parallel lines denote ± 1SD (n = 6 in all cases).

4.3.3.6 Monitoring of ischemia-induced kidney injury and tumorigenesis in vivo

The effectiveness of pH probes in monitoring inflammatory responses *in vivo* was also

tested using a kidney ischemia model using Balb/C mice. The ratiometric images of kidneys with and without circulatory defect were taken at 1 day after ischemic injury. The results show that following ischemic injury the pH decreased. However, in the control kidney (side without defect) the pH remained high (Figure 4.35).

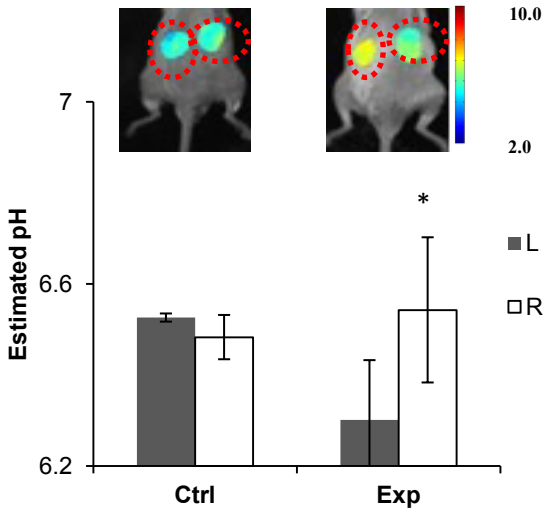


Figure 4.35 The effect of pH changes of the mice with and without ischemic kidney injury. The ischemic kidney injury were performed 30minutes prior to pH sensors administration intracascularly. The whole body images were taken at 1 day after ischemic injury. The merged ratiometric images and white light images showed the ratio changes, and the averages of associted pH values were quantified from the calibration curve and compared. Vertical lines denote ± 1SD (n = 3 in all cases). (Exp: the left kidney with ischemia injury; Ctrl: Control animal without treatment).

The pH probes are also tested in monitoring tumor generation (B16F10, melanoma in C57 mice) *in vivo*. Following subcutaneous implantation of B16F10 cells and saline (as control) in the presence of pH probes, the ratiometric images of cells and saline administration sites were taken daily for a period of 14 days. The results show that pH reduced (7.4 -> ~7.0) at the subcutaneous sites following the implantation of either saline or B16F10 cells. The pH reduced to pH 6.75 at 14 days in the corresponding tumorigenesis model (Figure 4.36). On the other hand, the pH at the saline injection sites increased with time and returned to ~pH 7.28 at day 14. These results are consistent with the microelectrode pH measurements in which pHs in the tumor and saline injection sites were 6.74 ± 0.05 and 7.25 ± 0.07, respectively.

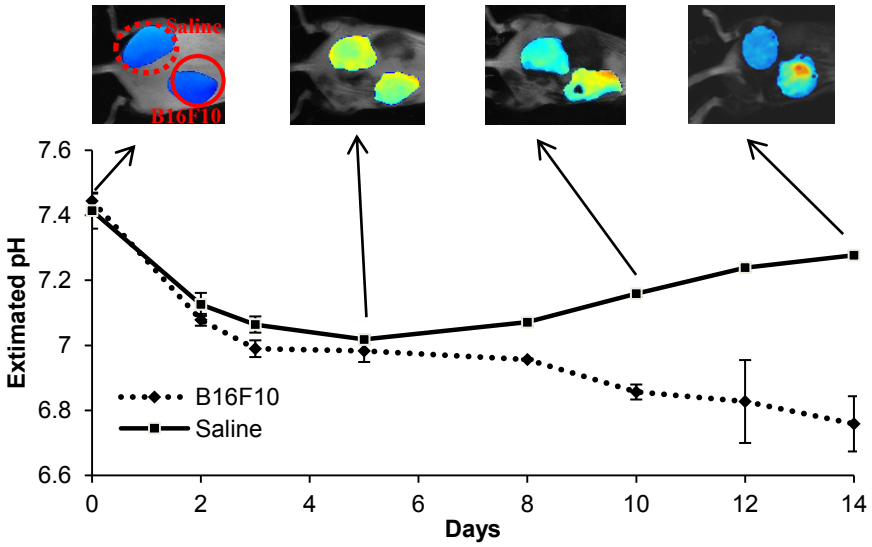


Figure 4.36 The effect of pH changes of tumor generation (B16F10) models. B16F10 cells and saline (as control) mixed with pH probes were implanted subcutaneously in the back of mouse skin. The meraged ratiometric images and white light images showed the ratio changes from 1 to 14 days at different implantation areas. The averages of associted pH values were also quantified from the calibration curve and compared. Vertical lines denote ± 1SD (n = 3 in all cases).

*4.3.4 Discussion and conclusion*

CypHer5E is a pH-sensitive cyanine dye which has minimal fluorescence at neutral pH but becomes highly fluorescent with an emission peak at ~670 nm in an acidic environment. On the other hand, Oyster800 has a constant fluorescence with an emission peak at ~794 nm regardless of pH. Both CypHer5E and Oyser800 dyes were found to be biocompatible and suitable as a dual fluorochrome probe, due largely to their optical properties. PNIPAM spheres with amino groups were synthesized using the precipitation polymerization method [87, 211]. Similar dual fluorochrome probe approaches have been carried out to monitor oxygen and enzyme activities (e.g., proteases) *in vitro* and *in vivo* [50, 179, 212, 213]. These techniques have the advantage of generating reproducible results independent of size and depth [214]. However, applications of ratiometric imaging have been mostly limited to the cellular level or to tumor growth. Little is known about whether pH ratiometric imaging probes can be fabricated to monitor tissue injury/inflammatory responses *in vivo*. Despite the fact that inflammatory responses play a pivotal role in many deadly diseases, there is a lack of noninvasive tools for

real time monitoring of inflammatory reactions. Although histological or IHC staining of immune cells, such as macrophages and lymphocytes, have been used to provide semi-quantitative assessment of the degree of inflammatory reactions [215-218], multiple-time-point studies are often not feasible. This is due to the large number of animals needed and time consuming histological process that are required in order to obtain reliable and reproducible results.

Our results show that *in situ* pH changes appear to be good indicators and determinants of inflammatory responses. These findings are indirectly supported by several earlier reports. Specifically, using pH-sensitive membrane peptides (pHLIP) by intraperitoneal injection [201] or pH-sensitive liposomes via i.v injection [219], studies have shown a good relationship between pH reduction (acidosis) and tissue injury/inflammatory responses. Interestingly, studies have also shown that acidic environments specifically may prompt inflammatory cell accumulation as well as nitric-oxide production [220, 221]. Unfortunately, these concentration-dependent probes cannot be used to quantify the pH changes in a dynamic environment such as real tissue *in vivo*. To address such deficiencies, several recent investigations have evaluated pH imaging in isolated cells and tissues using 2',7'-bis(carboxyethyl)-5,6-carboxyfluorescein (BCECF) fluorescence ratio techniques. However, these probes cannot be used for *in vivo* imaging since the fluorescent wavelengths remain in the visible-range with strong auto-fluorescent background and very limited penetration depth [175, 176]. Recently, some research has demonstrated the design and synthesis of a ratiometric near infrared probe for evaluating pH changes [50, 177]. Nevertheless, their applications are still limited to the intracellular levels [50]. For an *in vivo* imaging application, our pH probes are composed of both CypHer5E and Oyser800 dyes which have individual and distinct NIR spectra and can easily penetrate into tissue for up to several centimeters. Such tissue penetration capability allows us to investigate reactions inside the internal organs, such as kidneys and liver.

PNIPAM nanospheres were selected as the backbone of the pH probes for several

reasons. First, our own studies and many others have shown that PNIPAM spheres prompt minimal tissue responses [203, 222]. Second, amine-bearing PNIPAM spheres provide ample numbers of free amine groups for dye conjugation without the potential of auto-quenching due to overcrowded dye conjugation [223]. Finally, submicron-sized (217nm diameter) PNIPAM spheres allow increased tissue retention rates and reduce nanosphere diffusion into blood circulation without altering tissue responses to the implants [224, 225]. Nonetheless, for different applications, pH probes can also be synthesized using other carriers, such as silica nanoparticles, polystyrene particles, and phospholipid-coated polystyrene particles [51, 213, 226].

It is well established that biomaterial implants prompt varying degrees of foreign body reactions, inflammation, infection and fibrosis [11, 108]. The foreign body responses are often associated with recruitment and activation of inflammatory cells, including macrophages and neutrophils [81, 203, 208]. Our recent publications have also shown a good relationship between the extent of inflammatory cell recruitment/activation and associated tissue reactions [180, 208]. The results from the present study show that pH probes can be synthesized to continuously monitor pH changes *in situ* and *in vivo*. Such measurements can accurately reflect the extent of inflammatory responses in real time and *in vivo*. This new information provides a unique opportunity to study the molecular and cellular processes of inflammatory reactions with the benefit of using fewer animals while providing fast and accurate assessments of the response. The probe can be administered into tissue/organs to determine localized pH changes. When administered via intravenous injection, blood pH would have some effect on fluorescence signals. However, blood pH influence would be substantially reduced when the probe enters the tissues/organs. As an example, the results of kidney ischemic injury model showed that, with the same blood supply, probe signals show significant pH reduction at the ischemic kidney but not controls. We are also aware of the fact that low tissue penetration ability presents a challenge for the measurement of some internal organs (e.g., lungs and hearts) in

larger animals (rats or larger) [212, 227]. In these scenarios, topical adminstration would be needed. The results thus far suggest that pH probes and ratiometric imaging techniques may be further developed for improving our current understanding of many inflammatory diseases and also expediting the development of next generation treatments for inflammation-associated diseases.

By combining near infrared pH-sensitive and pH-insensitive fluorescence dyes into nanoparticles, a new nano-sized optical pH probe is developed to measure *in situ* pH changes using the ratiometric imaging technique. *In vitro* tests demonstrate that there is a linear correlation between the florescence intensity ratios and pH values ranging from 5.78 to 7.65. Using the pH probe in three different inflammation models for *in vivo* tests, a strong positive correlation was found between ratiometric pH changes and inflammatory responses measured by histological analyses. These results suggest that the pH probe can be employed to detect tissue acidosis in real time, reflecting the severity of inflammatory responses. Therefore, this presents an alternative method to determine pH ratio changes *in vivo* in a noninvasive, rapid, and highly sensitive manner and to monitor the real-time dynamics of inflammatory processes.

# CHAPTER 5

# DEVELOPMENT OF APPARATUS FOR THREE-DIMENSIONAL OPTICAL IMAGING ANALYSIS

## 5.1 Introduction

Many optical methods, including fluorescent and bioluminescent imaging, are widely used for drug development, disease research, and drug delivery. Unfortunately, most of these methods generate a planar image, flattening the animal into a two-dimensional (2D) projection. Although 2D optical imaging could provide the quantitative results for evaluation of the fluorescence probes, it may lose the depth and spatial relationships of a three-dimensional (3D) structure. To improve these issues, several optical 3D fluorescence models have been built to generate the quantification and visualization information of fluorescence probes [60-63]. Fluorescence molecular tomography (FMT) technology enables quantitative imaging of the fluorescent probe, or marker concentration to the pico-molar level with no tissue depth limitation [64]. However, the field of view of FMT was smaller and costs are much higher than traditional fluorescence reflection imaging (FRI). Some commercial products, such as MARS (Multimodal Animal Rotation System) from Carestream, can generate or at least approximate a 3D dataset at different angles (30º increment). However, they are often inadequate and unsuitable for producing specimens that retain their 3D structure, including 3D shape and locations.

Although 3D optical tomography systems could help determine the spatial relationships, they still cannot provide anatomical structure. Some researchers co-registered optical methods with microCT or MRI methods. However, it always cause location unmatched and is difficult to achieve simultaneously. Even though a new system could combine micro-CT and FMT in the same machine, the hybrid system is expensive and both modalities have different levels of achievable accuracy and details in the captured geometric models. To fill the gap, a robust,

simple, cost effective, and flexible 3D modeling apparatus was developed for a variety of different biomedical applications.

## 5.2 Three-dimensional distribution models for inflammatory models

### *5.2.1 Purpose*

3D fluorescence reconstruction models have been built to generate the visualization information (localization) of fluorescence probes [60-63]. Current optical tomography can not provide the information of anatomical structure [60, 62, 71, 72, 228]. This study was therefore aimed at developing a cost effective, and flexible multi-modality 3D reconstruction modeling system, including both X-ray and optical imaging, based on KODAK *In-Vivo* FX system (Carestream Health, Inc., Rochester, NY).

### *5.2.2 Methods*

The 3D X-ray and optical projection tomography (OPT) in small animals automatic motor setup is based in KODAK *in vivo* FX system. The schematic representation of the experimental setup is shown in Figure 5.1. In brief, mice were placed into the animal rotation tube that was fixed on the step motor (TECO 4H5618, with step angle 1.8°) and controlled by MATLAB (The Mathworks, Inc., Natick, MA) software. The animal was not in an upright position but is instead recumbent to minimize positional stress. After each angular rotation, a series of white light (X-ray) and fluorescent projection (shadow) images were captured. Following the captures, 3D reconstruction modeling was implemented to generate the distribution representation.

#### 5.2.2.2 3D reconstruction modeling

There are two 3D reconstruction models in this study. The first model is the 3D reconstruction model from white light (*in vitro*) or X-ray projection (*in vivo*) images which can provide the surface details or anatomy structure, respectively. The second model is the 3D reconstruction from fluorescent projection images which can be used to determine the bio-distribution of fluorescence probes. .

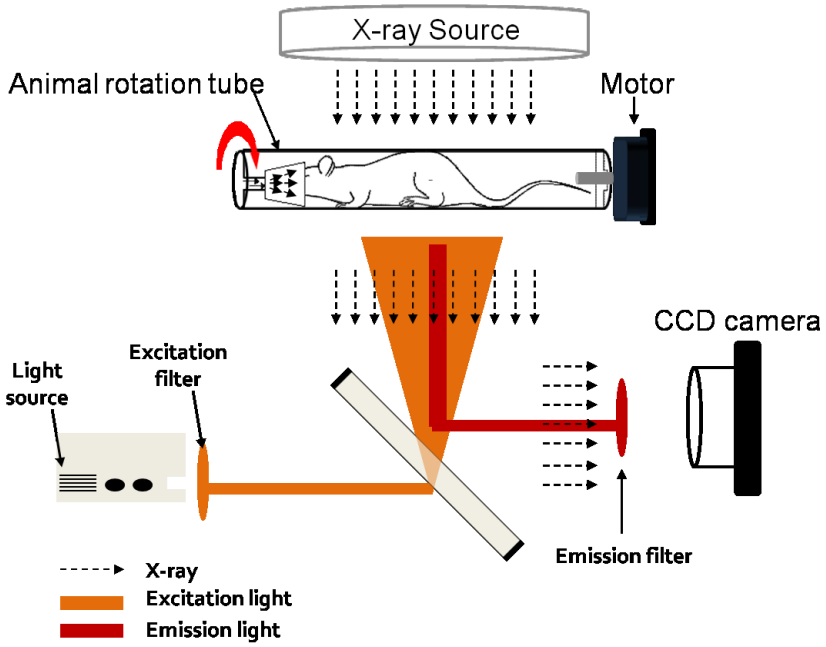


Figure 5.1 Illustration of 3-D motor setup based on KODAK in vivo FX system

The 3D reconstruction method is based on back-projection algorithm either white light (X-ray) or fluorescent images. [60-62] The flowchart of the 3D reconstruction algorithm is shown in Figure 5.2.

In brief, the reconstruction model was obtained using the simple approach of adding all the projections (shadows) of the specimen, equivalent to the radon transform method with a constant filter [60]. In order to solve the effect of small changes in position, the most reliable approach for finding the position of the axis of rotation is to determine the position as the one that minimizes the error between each projection and its mirrored 180° counterpart, using the following formula:

$$x_{center}^{(i)} = \min\left\{\left|\bar{I}\left(x - x_{center}^{(i)}, y, \theta_i\right) - \bar{I}\left(-\left(x - x_{center}^{(i)}\right), y, \theta_i + \pi\right)\right|\right\} \quad (5.1)$$

Equation (5.1) is used for each ($\theta_i$, $\theta_{i+\pi}$) pair, and the final axial position is found as the average. We emphasize that Equation (5.1) has proven to be very useful *in vivo* where slight changes in position over time are observed. The out surface could be reconstructed if we perform inverse radon transform on each image slice at different angles. The projected data from different angles for one single slice are accumulated to form the sinogram in order to

operate the inverse radon transform. After the inverse radon transform, a series of two dimensional (2D) reconstructed images are obtained. 2D reconstructed images are then smoothed by 3x3 Gaussian kernels. Finally, the smoothed 2D reconstructed images are stacked together to form the 3D volumetric image and 3D surface rendering is generated by MATLAB's isosurface extraction algorithm [62].

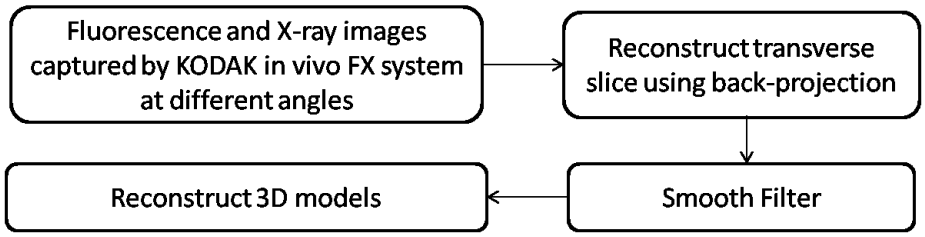


Figure 5.2 The flowchart of the 3D reconstruction algorithm

5.2.2.3 Prototype performance evaluation using rat head phantom

The phantom of the rat's head (Figure 5.3a) was used to:

(1) Evaluate the motor system and 3D reconstruction method.

(2) Optimize the projection number for 3D reconstruction. Although increase in the number of projections can benefit the quality and spatial resolution of reconstructed images, time for each measurement increases accordingly. Increase in the measurement time may affect the outcome for *in vivo* study and appropriate selection of projection number should be taken into consideration.

To perform the measurement, the rat's head phantom was fixed on the step motor. The head phantom was rotated around an axis perpendicular to the beam over 360° and a series of white light images were captured with the step angle of 1.8°. After acquisition of projection images, 3D reconstruction method was implemented and 3D surface rendering can be generated. To optimize the projection numbers, the accuracy of surface reconstruction by different projection numbers was evaluated by comparing the error of radius versus projection number. The optimized projection number was used throughout all studies.

5.2.2.4 Prototype performance evaluation with tissue-mimicking phantom (*in vitro*)

For further validation of the proposed methodology, we performed the *in vitro*

measurement by using the tissue-mimicking phantom. The tissue-mimicking phantom was made by gelatin mixed with intralipid solution (scattering agent) and diluted India ink (absorbing agent), and was filled in the rotation tube (Figure 5.3b). As commonly used, a set of absorption and reduced scattering coefficients of $\mu_a$= 0.1 $cm^{-1}$ and $\mu_s'$ = 10 $cm^{-1}$ were selected to simulate the background tissue. Three spherical gelatin inclusions of 8mm in diameter were embedded 3 mm below the surface of phantom (from center of sphere to the surface), mixed with the background tissue phantom and three different concentrations (0.01%, 0.03%, 0.1%) of pH probes, as described in Chapter 4. The schematic illustration of phantom setup is depicted in Figure 5.3c. Following the steps in section 5.2.2.3, the tissue-mimicking phantom was fixed on the motor driver and a series of white light and fluorescence projection images at both wavelengths (pH-sensitive and reference) were captured over 360° with an interval of optimized angle which rotates around an axis perpendicular to the beam. After acquisition of projection images, the 3D reconstruction models from white light and fluorescence images at both wavelengths were generated. The 3D white light reconstruction models can be used to generate the outer surface of object. The 3D reference reconstruction models can be used provide the information of the pH probes location. Finally, by taking the ratio of 3D pH-sensitive and reference reconstruction models, the ratiometric 3D models can provide the information of estimated pHs.


(a) (b) (c)

Figure 5.3 Photograph of phantoms. (a) rat head phantom. (b) tissue- mimicking phantom. (c) the schematic illustration of tissue-mimicking phantom with three spherical gelatin inclusions.

5.2.2.4 Prototype performance evaluation with *in vivo* animal test

To evaluate the potential of this system for small animal imaging, we implemented the above methodology into an *in vivo* experiment. Two different animal models were used for this study. First, PNIPAM-Oyster800 probes (3 sites, in reference channel) were injected subcutaneously on the back of Balb/c mice. Second, $TiO_2$ microspheres and saline (as a control) were implanted into various locations on the back of mice. After implantation of $TiO_2$ microspheres, pH probes were administrated intravenously. During the data acquisition, the mice were anesthetized using isoflurane inhalation. A set of multimodal images, including X-ray, multispectral fluorescence images, were captured at every craniocaudal rotation angle (optimized angle from 5.2.2.3). After acquisition of projection images, the 3D reconstruction models from X-ray and fluorescence projection images from reference channel were generated to provide anatomical structure information and localization of fluorescent probes, respectively. Moreover, by taking the ratio of 3D pH-sensitive and reference reconstruction models, the ratiometric 3D models can be used to provide the information of estimated pHs in the second model.

*5.2.3 Results*

5.2.3.1 Prototype performance evaluation using rat head phantom

The test subject used in this study was a phantom of a rat's head (Figure 5.3a). A series of white light images were generated by our setup every 1.8° (precision of the motor). For the geometry extraction algorithm, the raw data for two projections at 45º and 135º angular positions is present (Figure 5.4). The out surface of the phantom was reconstructed using inverse radon transformation on each projection image slice at different angles. The projected data from different angles for one single slice (slice 270) are accumulated to form the sinogram in order to operate the inverse radon transform (Figure 5.5). After applying the inverse radon transform, the surface reconstructed image is smoothed and the edge is extracted as the surface of the phantom. Three lines represent the three layers of the phantom (Figure 5.6a).

The corresponding transverse slice results in back-projection reconstruction from gray-scale projection images (Figure 5.6b).

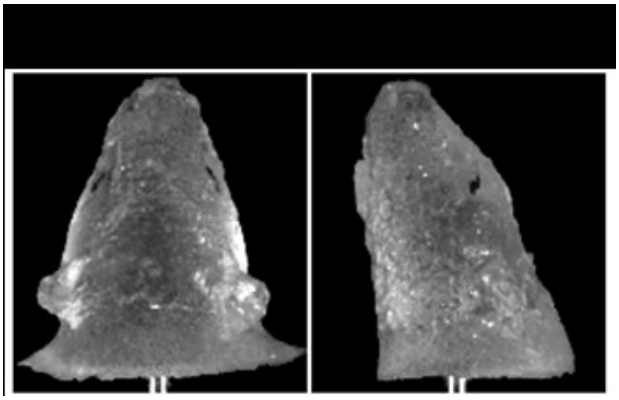

Figure 5.4 The white-light image acquired from the system at 45º and 135º angular positions.

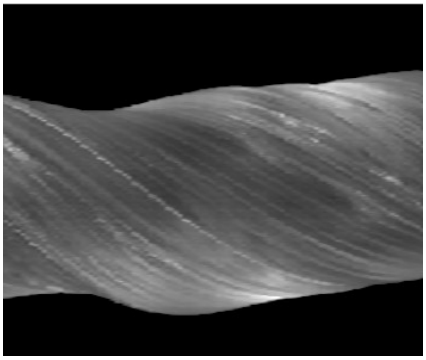

Figure 5.5 The sinogram produced by applying the Radon Transform.

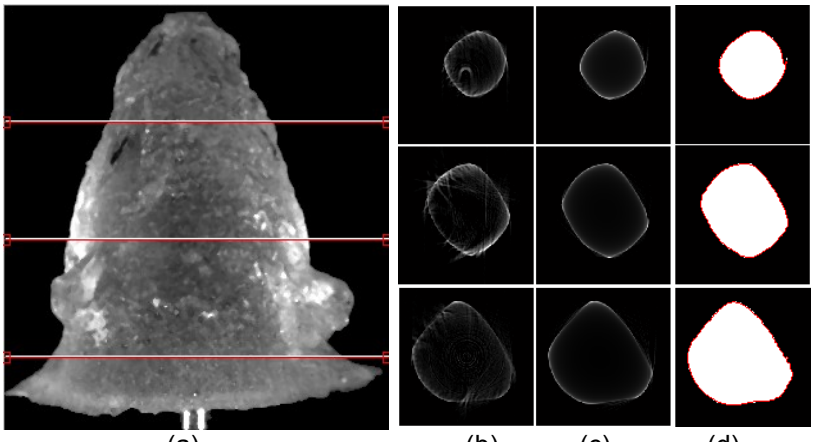

(a) (b) (c) (d)

Figure 5.6 Results of slice reconstruction and image processing. (a) The white image, the horizontal red lines represent the 90, 180, 270 slice, respectively; (b) Back-projected data for slices from grayscale image; (c) Back-projected data for slices from black/white threshold image; (d) After the smooth filter and threshold data from (c). The red line represents the edge detection from the threshold image.

Since the white/black images lost the gray-scale information, the resolution is low with serious artifacts, the smooth filter was necessary in the reconstruction. The results after the smooth filter are shown in Figure 5.6c. With threshold setting and reconstruction, the images of all slices are clearer which benefits the extraction of the edges of each layer (Figure 5.6d). An 8-adjacent Connection method was used to extract the edges (red lines) (Figure 5.7). Connecting each edge, the final result of 3D surface reconstruction of the phantom is shown in Figure 5.7.

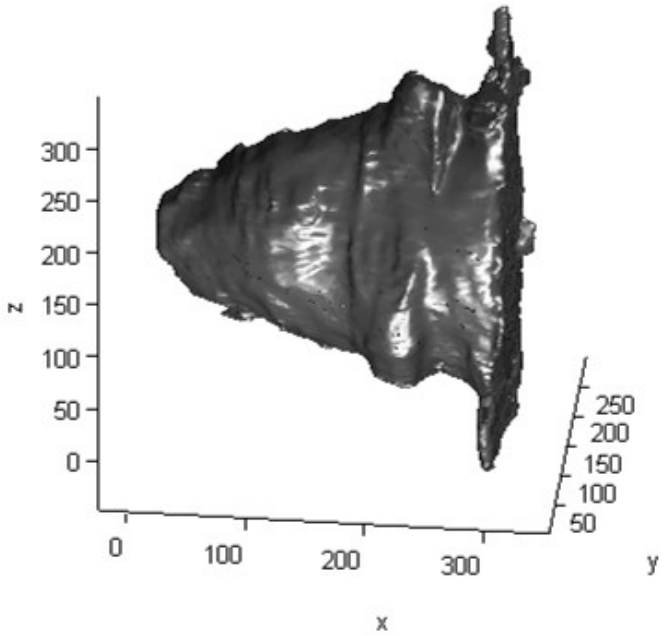


Figure 5.7 Result of 3D reconstructed surface of rat's head.

5.2.3.2 Surface reconstruction accuracy

To study the accuracy of the surface reconstruction setup, experiments were performed to vary the position of the sample with respect to the axis of rotation and to measure several different numbers of projections, varying from 200 projections to 10. The rat's head phantom was used to obtain different cross-sections (slice 90, 135, 180, 200, and 270). By reconstructing by inverse radon transform, the reconstructed planes (Figure 5.8) and the outer surface boundaries were extracted. The average radius of each plane was calculated by the number of projections (Figure 5.9a). We also present the results for the error in retrieving the radius (in percentage) versus number of projections for different planes (Figure 5.9b). Higher projection

numbers also present the longer capture time and longer reconstruction time. For *in vivo* real time imaging, the preferred setup should require minimal image capture time. Based on this consideration, 41 slides were chosen with 9° rotation which permits the minimum number of projections to acquire a well-defined surface. Additionally, it should be noted that even for optimal working conditions and a phantom placed in the center of rotation, an error of 1% is present due to the pixel size.

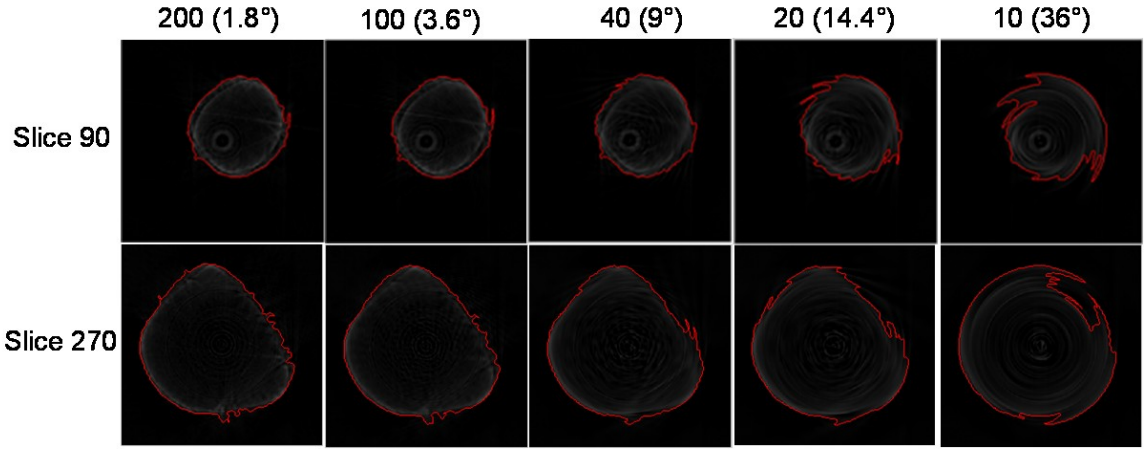


Figure 5.8 (a) Reconstructed slices of 90 and 270 from rat's head with different numbers of projection (different angles).

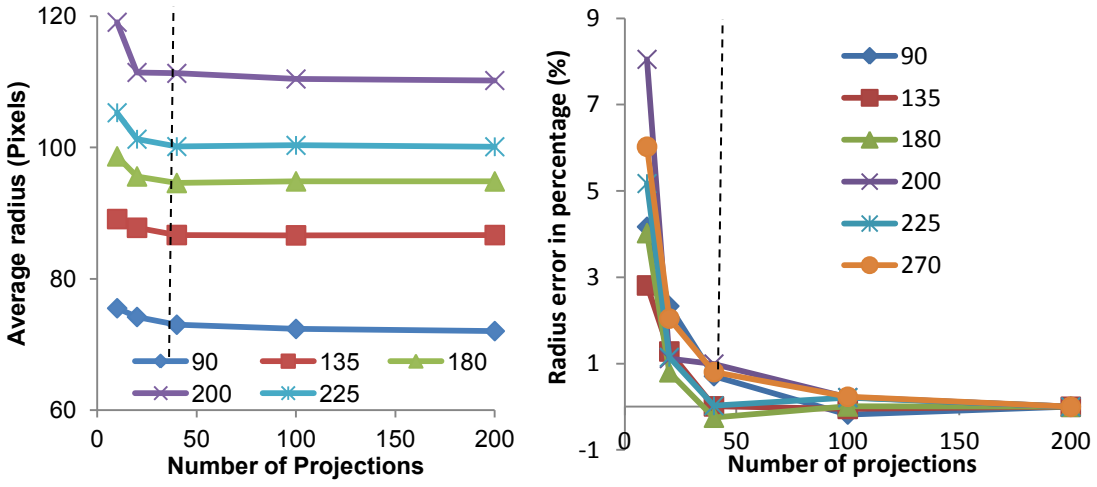


(a) (b)

Figure 5.9 (a) Reconstructed radius versus number of projections.
(b) Reconstructed radius versus distance in respect to the center of rotation for various numbers of projections.

5.2.3.3 Prototype performance evaluation with tissue-mimicking phantom (*in vitro*)

A set of multimodal images, including white light and multispectral fluorescence images, were captured at every craniocaudal rotation angle (9º). Following the 3-D reconstruction modeling from white light and reference channel, the surface images of tissue-mimicking phantom (gray) and the surface images of three spherical gelatin inclusions (color coded) were also generated (Figure 5.10). The localization of different spherical gelatin inclusions with different concentrations (0.01 – 0.1%) were also visualized in the 3D reconstructed models at different view directions (Figure 5.10). Different x-y cross-sections (three spherical gelatin inclusions with different concentrations) in the reference reconstructed model (Figure 5.11a) were compared with the ratiometric 3D models by taking the ratio of 3D pH-sensitive and reference reconstruction models (Figure 5.11b). Interestingly, we found the intensities varied in the reference and the reconstructed model. However, the ratio values are almost the same in the ratiometric model.

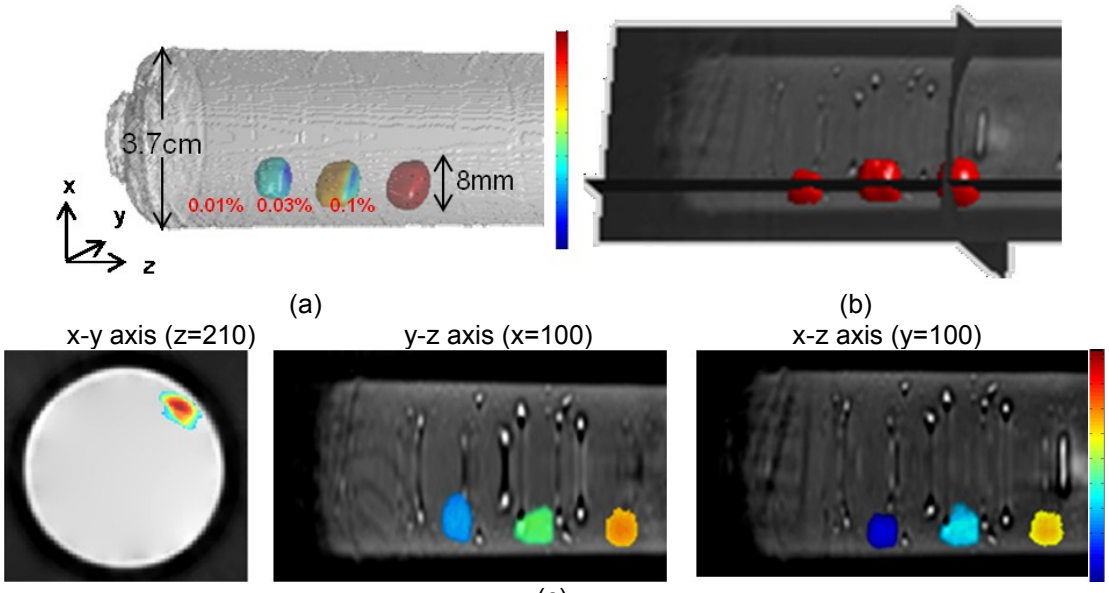


Figure 5.10 Result of 3D reconstructed models using tissue-mimicking phantom. (a) 3D reconstructed out surface of phantom (gray) and spherical gelatin inclusions with different concentration (0.01 – 0.1%)) of pH probes (color coded). (b) 3D reference reconstructed out surface of three spherical gelatin inclusions (red) of tissue-mimicking phantom with cross-sections at different orientations. (b) Different cross-section views at different orientations of pH probes.

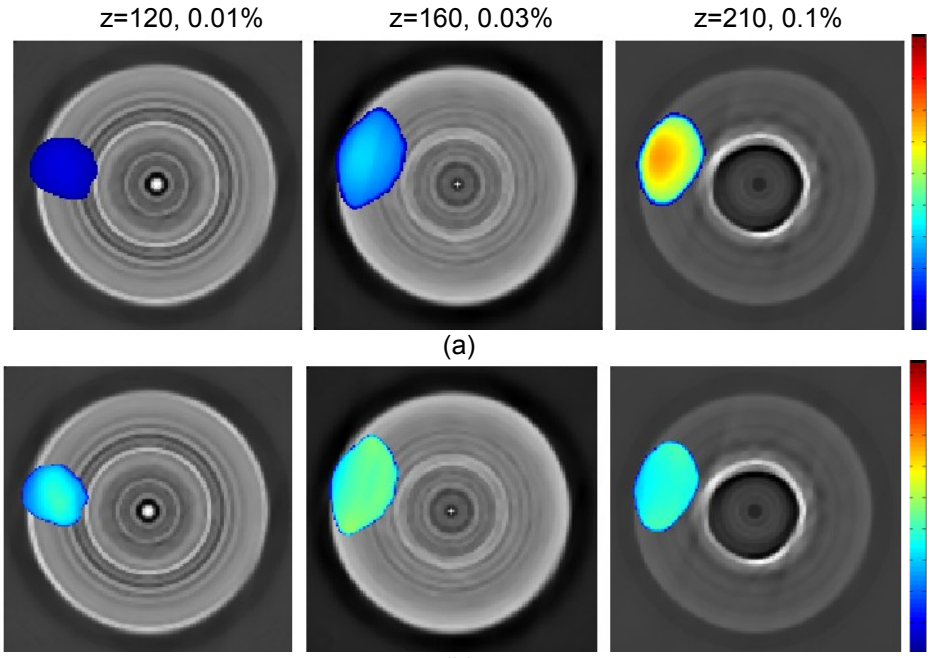


Figure 5.11 Result of 3D reconstructed models using tissue-mimicking phantom at different cross-sections of x-y axis from (a) 3D reference reconstructed model, and (b) ratiometric model.

5.2.3.4 Prototype performance evaluation with *in vivo* animal test

The potential of this setup on imaging small animals was then tested *in vivo*. First, the PNIPAM-Oyster800 probes (3 sites) were injected subcutaneously on the back of BALB/c mice in various locations (Figure 5.12). During the procedure, the mouse was anesthetized using isoflurane inhalation. A set of multimodal images, including X-ray, and multispectral fluorescence images, were captured at every craniocaudal rotation angle (9º). The images were spectrally unmixed and overlaid on the X-ray image with different projection angles (Figure 5.12, 5.13a). Following the 3-D reconstruction modeling, the surface data of mouse body (gray) and the three injections of PNIPAM-Oyster800 sites (red) were generated (Figure 5.13b). Without 3-D reconstruction it is impossible to get the shape information from capture images in the traditional 2-D X-ray and fluorescence imaging. After 3-D reconstruction, we could observe the details and injection locations at different sites. As shown in Figure 5.13c, d, e, the locations of different implant sites were clearly visualized at different directions.

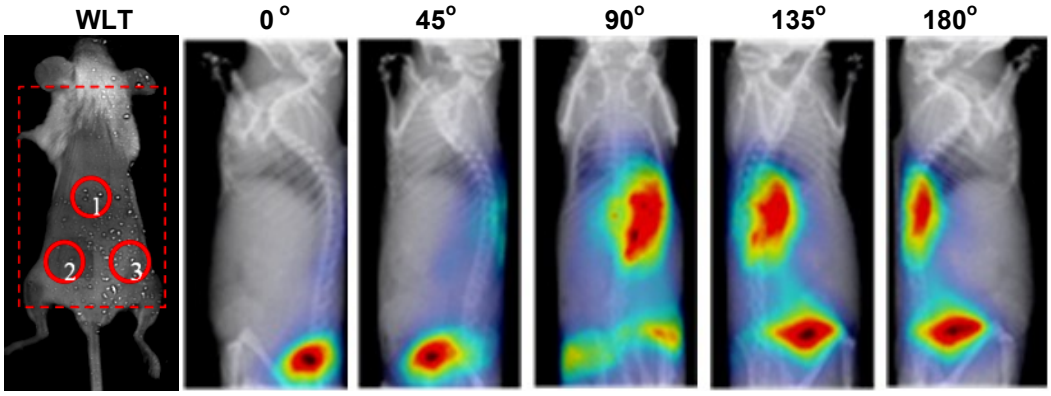


Figure 5.12 Mouse administered PNIPA-Oyter800 fluorescence agents and rotated 180 degrees about craniocaudal axis. X-ray and spectrally unmixed fluorescence overlays are shown every 45 degrees.

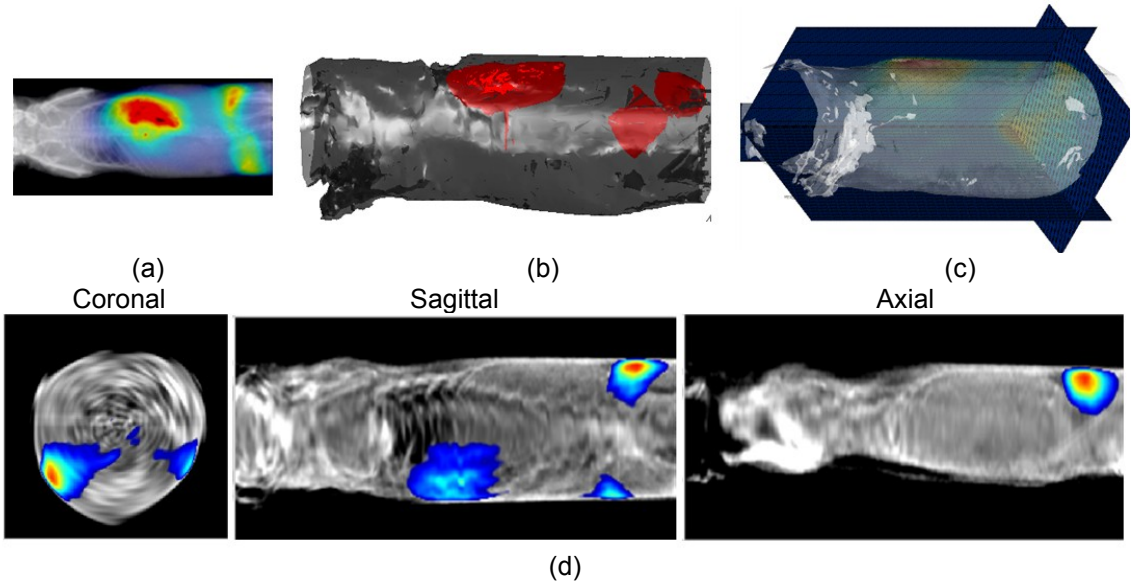


Figure 5.13 Result of 3D reconstructed models using *in vivo* model. (a) Schematic of 3 sites of PNIPAM-Oyster800 probes in 2D white light images. (b) 3D reconstructed out surface of mouse (gray) and 3 sites of PNIPAM-Oyster800 probes (red). (c) 3D reconstructed out surface of mouse with cross-sections at different orientations. (d) Different cross-sections for different views of PNIPAM-Oyster800 probes.

Next, we used this model for pH probes (pNIPA-CypHer5E-Oyster800) to detect implant-mediated inflammatory responses. $TiO_2$ microspheres and saline (as a control) were implanted into various locations on the back of mice. The pH probes were administrated intravenously. After 24 hours a set of multimodal images, including X-ray, and multispectral fluorescence images, were captured at every craniocaudal rotation angle (9º). The mouse was anesthetized using isoflurane inhalation during the procedure. The images were spectrally

unmixed and overlaid on the X-ray image with different projection angles (Figure 5.14). Following 3-D reconstruction modeling, the surface data of the mouse body (gray) and the bio-distribution of pH probes (red) were generated (Figure 5.14). After 3-D reconstruction, in the Oyster-800 channel (reference channel), we could see relatively high signals appearing at the kidneys' site, and less signals on the $TiO_2$ implantation sites (Figure 5.15), and we can also determine the positions of different organs, kidneys, liver, spleen, by applying local thresholding. However, after applying the pH ratiometric imaging, we found the relative high signals in the $TiO_2$ area, which means the pH reduced. As shown in Figure 5.156, we could visualize the location and shape of $TiO_2$ clearly by the surface rendering approach.

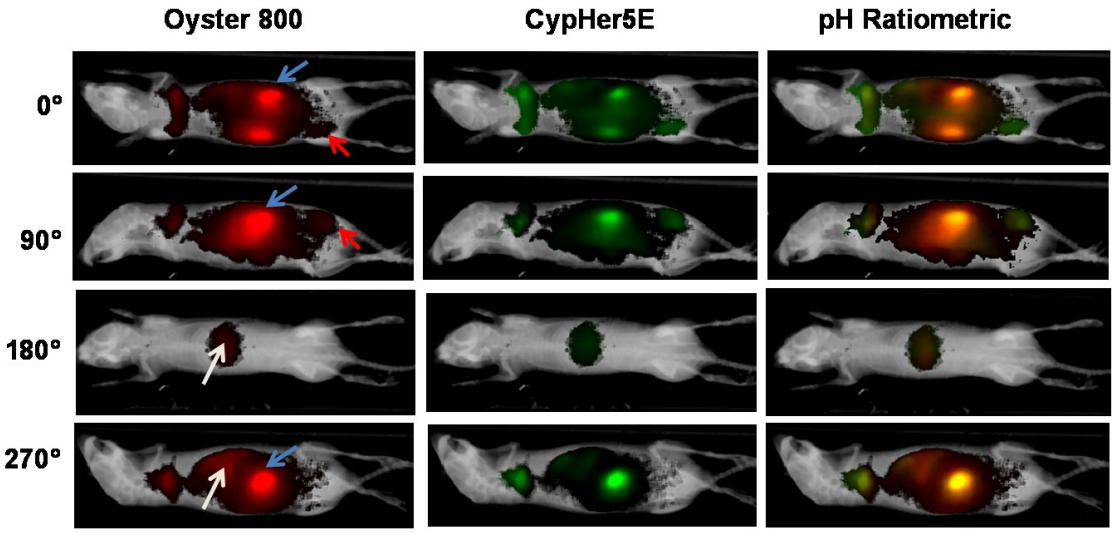


Figure 5.14 Mouse administered pH probes and rotated 180 degrees about craniocaudal axis. X-ray and spectrally unmixed fluorescence overlays are shown every 90 degrees, CypHer5E (green-coded) and Oyster800 channels (red-coded) and resulting ratio (mix with red and green). (Blure arrows show the location of kidney, white arrows show the location of liver, and red arrow show the implantation of $TiO_2$).

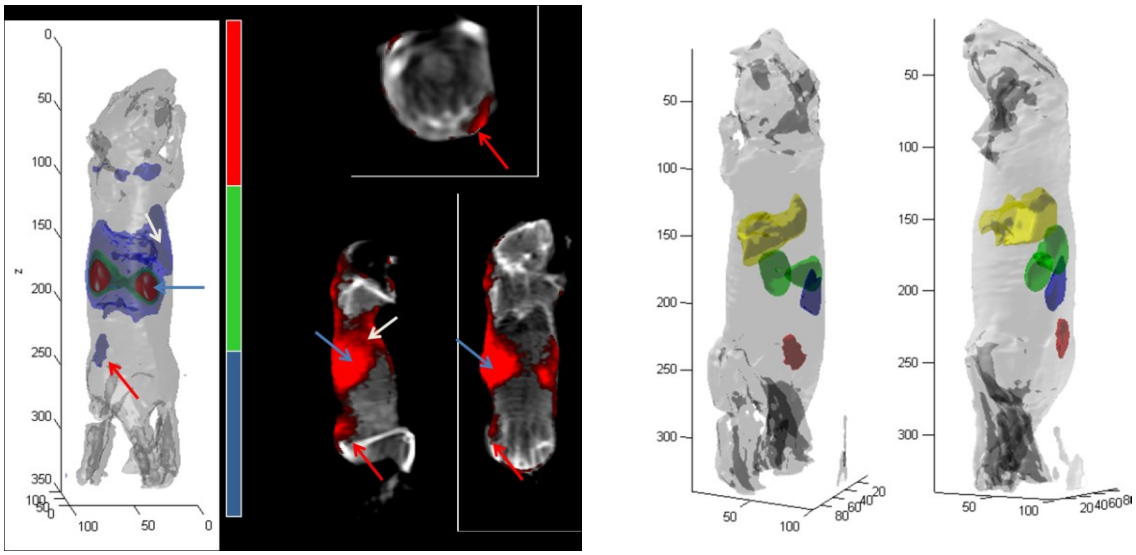

(a) (b) (c)

Figure 5.15 (a) Result of 3D reconstructed out surface of mouse with different surface thresholding. (b) Fused coronal (top), sagittal (left bottom) and axial (right bottom) slices for different view of pH probes in Oyster800 (reference channel). (Blue arrows show the location of kidney, white arrows show the location of liver, and red arrow show the implantation of $TiO_2$). (c) Location of different organs by at different view. (■: out surface of mouse, ■: Liver, ■: Spleen, ■:$TiO_2$ implant site.)

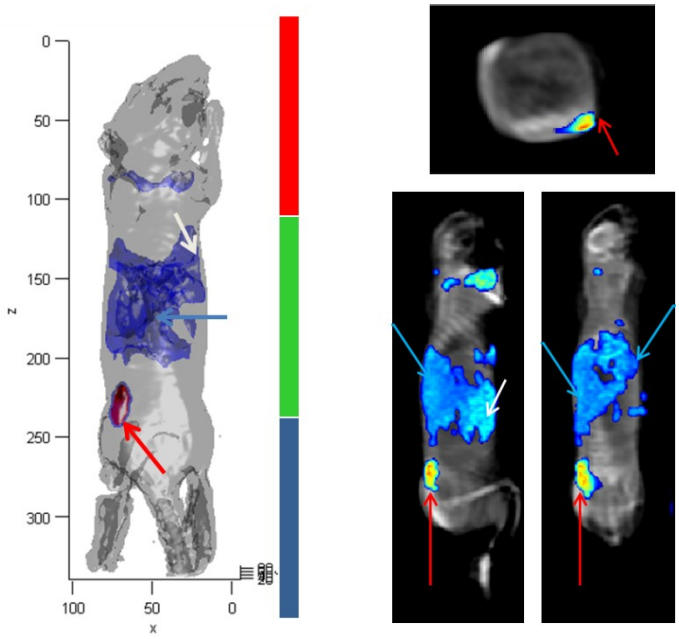

(a) (b)

Figure 5.16 (a) Result of 3D reconstructed out surface of mouse with different surface thresholding. (b) Fused coronal (top), sagittal (left bottom) and axial (right bottom) slices of pH probes in pH ratiometric channel. (Blure arrows show the location of kidney, white arrows show the location of liver, and red arrow show the implantation of $TiO_2$).

*5.2.4 Discussion & Conclusion*

In the present study, the design of a 3D reconstruction system has been implemented and tested in phantoms as well as in live mice for *in vivo* optical tomography. The approach presented here is useful due to its simplicity and relative low cost. Another advantage for this system is that it can provide the ability to acquire large data sets and number of projections without the need of matching fluids compared with other fiber-based systems or fixed geometry setups [62]. Our results demonstrate the feasibility of using this system to achieve 3D visualization of fluorescence probe distribution *in vivo*. However, the proposed inverse radon-transform-based 3D reconstruction consists of two hidden assumptions, which are: (1) negligible light absorption by background tissue/medium, (2) negligible light scattering of background tissue/medium. While ignoring the light absorption by background tissues, we have assumed that intensity of fluorescence light is probe-concentration dependent regardless of location of the fluorescent probe. Nevertheless, light intensities from excited and emitted fluorescence wavelengths are highly dependent on the location of fluorescent probe, and also attenuate with increase in depth, leading to dramatic errors in quantification. To reduce the absorption effect, we have proposed the ratiometric approach for 3D reconstruction models. In traditional 2D projection images, the results showed that ratiometric approach can avoid the influence of concentration (Figure 4.24) and depth (Figure 4.25). Moreover, the results from the tissue-mimicking phantom already demonstrated that ratiometric values from 3D reference and pH-sensitive reconstruction models are probe concentration independent at same depth (Figures 5.11). To further investigate the effect of tissue depths, we performed another phantom experiment. Two spherical gelatin inclusions with same probe concentration were embedded at different locations (3 mm and 18 mm below the surface) and 3D reconstructions were created followed by the proposed methods. Ratiometric model was then generated after obtaining the 3D pH-sensitive and reference model. Figure 5.17a exhibits the reference reconstructed model and Figure 5.17b shows the 3D ratiometric model. It clearly demonstrates that fluorescence

intensities for the deeper inclusion are lower than those for shallower inclusion (Figure 5.17a). After taking ratio between pH probe and reference images, Figure 5.17b shows similar ratiometric values for both inclusions regardless of the depth, indicating that ratiometric approach does help to correct the absorption effect during 3D reconstruction and thus helps quantification.

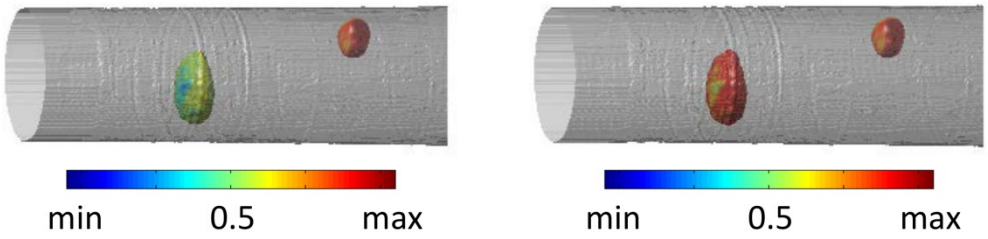


(a) (b)

Figure 5.17 (a) 3D reference reconstructed model for pH probe and (b) ratiometric model.

Another hidden assumption for the proposed methodology is ignoring the scattering effect of light, which may cause the loss of spatial resolution and location accuracy. Although no obvious localization errors were observed in tissue phantom and animal studies. However, to further investigate the influence of light scattering effect, we performed the 3D reconstruction under three different conditions, as follows:

(1) Inverse radon transform was executed with 0-180 degree data on the object's side

(2) Inverse radon transform was executed with 180-360 degree data on the side which is far from the object.

(3) Inverse radon transform was executed with 0-360 degree on whole object.

The 3D reconstructed pH-sensitive images are showed in Figure 5.18. The results from 0-180 degree (Figure 5.18a) and 0-360 degree (Figure 5.18c) were similar since the inverse radon transform was mainly contributed by the fluorescent signals from 0-180 degrees. However, the reconstructed model from 180-360 degree (Figure 5.18b) showed the localization error and the dramatic shape distortions due to light scattering effect. Similar results were found in previous literature [229]. To minimize the effects of light scattering, a deconvolution approach

could be used to apply scattering corrections during 3D reconstruction. The similar approach of scattering corrections was applied in PET [230] and optical 3D reconstruction [229]. Furthermore, the effectiveness of computational work needs to be optimized and is a topic for our future work.

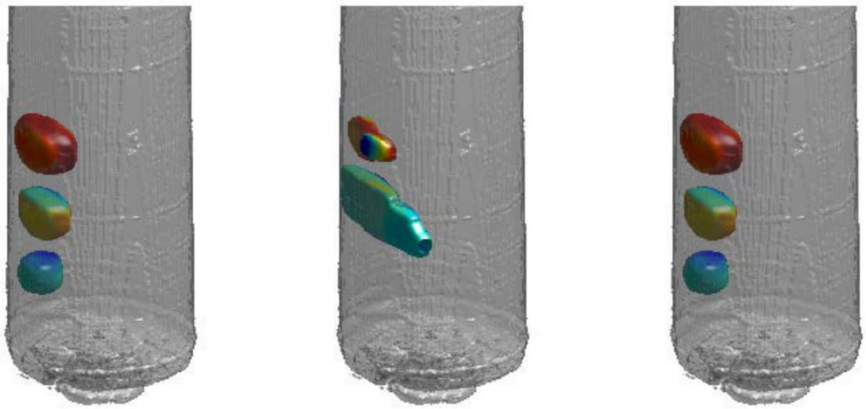

(a) (b) (c)

Figure 5.18 3D reference reconstructed models for pH probe from inverse radon transform were executed with (a) 0-180 degree data on the object's side, (b) 180-360 degree data on the side which is far from the object, and (c) with 0-360 degree of whole object.

The accuracy of surface reconstruction was first investigated *in vitro*. Considering the time and reconstruction accuracy, the results show that 41 (9°) and higher number of projections can generate well-defined surface image for our setup. However, it is difficult to maintain the target sample exactly on the center of rotation along its entire axis. It may produce reconstruction results with low precision because the lowest error retrievable is simply determined by the pixel size. For *in vivo* imaging, we have to consider the movement of mouse surface due to breathing and movement which may reduce the reconstruction accuracy. Because this setup is used for diffuse light imaging, any change in the order of the transport mean free path (typically 1 mm) will not have measurable impacts on the reconstructed data. We therefore believe that the accuracy of this approach is appropriate for *in vivo* imaging.

Currently we have tested this system in two different models. First, the mouse was injected subcutaneously at three locations. By performing 3D reconstruction, the location of PNIPA-Oyter800 injection sites and also the shape and depth of the PNIPA-Oyter800 can be

observed. The results show that our surface reconstruction model can be successfully used to visualize the location in 3D. A second animal model used evaluated in this study involves the use of the pH probe (combined with Oyster800, reference channel and CypHer5E, pH-sensitive channel) to detect implant-mediated ($TiO_2$) inflammatory response in a murine models [12, 91, 141]. Interestingly, the signals in the kidney and liver areas are relatively higher than the implantation site in the Oyster800 (reference channel). It is possible that most of the pH probes circulated to the kidney and liver area, while less accumulation occurred at the $TiO_2$ sites. However, by calculating the ratiometric imaging to represent the estimated pH values, we found the pH is similar in both kidney and liver (relatively high) and lower (acidic) at $TiO_2$ sites. By combining the information obtained from these two wavelengths, we could observe the bio-distribution of these probes while simultaneously acquiring the location of pH information in a 3D manner.

The utilization of 3D reconstruction technologies could also facilitate the research on different target organs and imaging applications with arbitrary boundaries, such as spleen, thymus, testes, limbs, and head. It can also benefit other molecular imaging applications. The technology could additionally be ideal for brain studies in small animals. This method is relatively straightforward, and may open new modalities for imaging disease, drug response, and inflammation *in vivo* with the potential for in-depth clinical applications.

The main drawbacks when using this type of approach is the fact that convex surfaces cannot be reconstructed [62]. However, the small animals used for imaging actually present very few regions of convexity. It is important to note that since the presented experimental setup allows significantly large data sets to be obtained, fast inversion schemes become crucial in efficient implementation in 3D optical tomography [231-233]. The inversion algorithm could also be further improved for faster more reliable reconstruction and rendering of the fluorescence data in 3D, thus fully exploiting the surface extraction capabilities of the system [62, 234]. In terms of instrumentation in the future, the setup could be improved by minimizing the time

required for one full experiment by designing and automating a system for filter alteration and autofocus zoom objectives as well as an *x*–*y* positioning system for the subject to enable the observation of various areas of interest (such as *in vivo* imaging of fluorescent protein emission in single organs) [62].

Overall the free-space approach can offer a significantly higher level of flexibility in using 3D optical imaging. This could lead to high performance optical tomographic investigations by enabling the collection of superior information content data sets compared with traditional 2D methods. Finally the setup design allows for straightforward use of the time-resolved technology further increasing the obtained data content [235].

CHAPTER 6

CONCLUSION

## 6.1 Summary

This dissertation summarizes my work on the development of imaging methods to study different processes governing inflammatory responses as depicted in Figure 6.1.

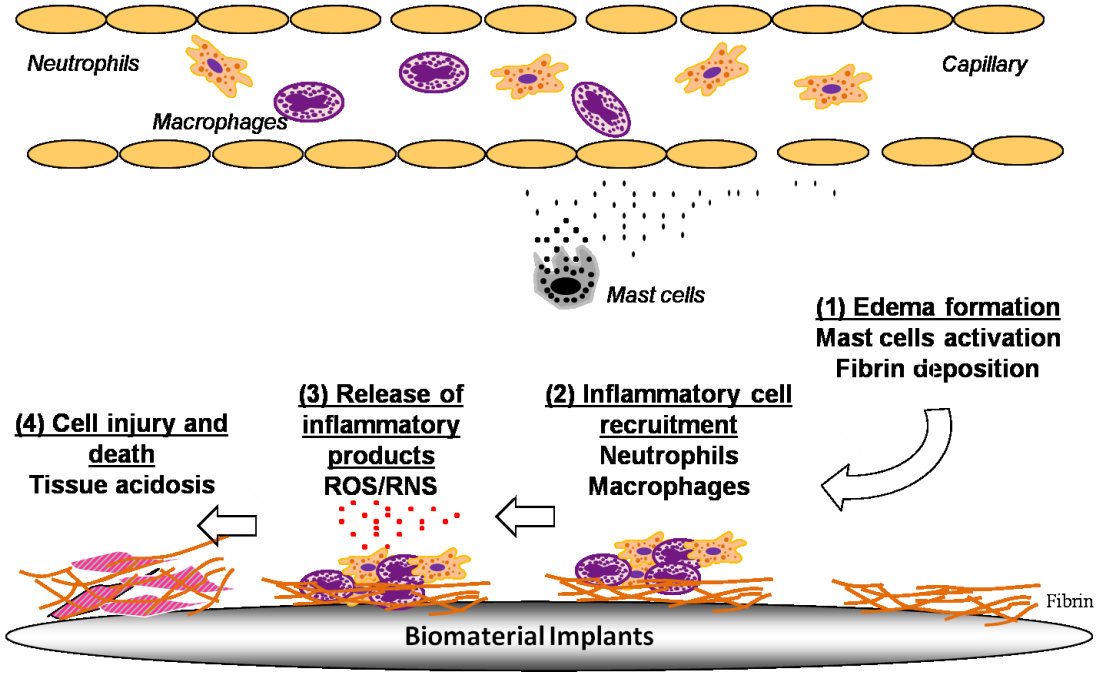


Figure 6.1 Summary of the development of imaging methods for different processes of the inflammatory response.

First, fibrin-affinity NIR probes were found to be able to detect fibrin deposition and the associated edema formation within 15 minutes after induced infection and inflammation. Mast cell activation is responsible for triggering this fibrin deposition.

Second, neutrophil- and macrophage- targeting NIR probes were fabricated to target formyl peptide receptor and folate receptor, respectively. Both probes were found to detect their targeted cells and the respective recruitment to LPS and biomaterial particle implant sites.

There is a good relationship between probes' fluorescent intensities and inflammatory cell counts by histological analyses. In addition, both probes can be used to non-invasively monitor inflammatory responses, including foreign body reactions and infection, in real time.

Third, L-012, a highly sensitive chemiluminescent probe, was found to be able to noninvasively monitor the inflammatory response-associated ROS activities both *in vitro* and *in vivo*. There is also a good linear relationship between chemiluminescence intensity and PMN numbers surrounding inflamed tissue. Our results also show that neutrophils are mostly responsible for the ROS production *in vivo*.

Finally, a novel pH ratiometric optical probe was fabricated to measure tissue pH *in vivo*. By taking the ratio of fluorescence intensities at different wavelengths, these probes provide excellent measurement, distribution, and change of tissue pH at different time points. We find that the ratiometric pH changes are a good indicator of inflammatory responses confirmed by histological analyses.

A parallel study was carried out to explore the possibility of monitoring fluorescence distribution via 3D models. A rotating device was developed as a prototype for 3D imaging and modeling. Using the device, I was able to map the spatio-temporal distribution of fluorescence probes leading to better understanding of *in vivo* locations. This was achieved using our modified model from the KODAK in vivo FX system. The results obtained in this study show that 3D reconstruction models can provide the shape, depth, and bio-distribution information for our inflammation model.

## 6.2 Future directions

Although these results are exciting, more studies are needed to push these imaging methods for routine use in the research and clinical setting. These efforts should be carried out in several areas as summarized below.

First, it's possible to fabricate different imaging probes with NIR dyes with different wavelengths. These probes can be applied to the same animals simultaneously. These

approaches will allow us to simultaneously study different cells and cellular responses.

Second, all imaging probes, excluding pH probes, may be subject to concentration and depth dependency. In our studies, all experiment were carried out in subcutaneous models, and we did not encounter any significant issues. However, if these probes will apply to the systemic models, such as diseases from deep tissues, we need to develop a new approach to overcome the dependence of concentration and tissue thickness. Ratiometric imaging method is one possible approach. The potential limitation of ratiometric imaging system is the tissue penetrating ability of light from different emission wavelengths of the two fluorophores. Basically, the emission of shorter wavelength shows stronger tissue absorbance than the emission of longer wavelength. In order to correct for the penetrating abilities of light at the different imaging wavelengths, the standard curve of fluorescence data were obtained under identical conditions.

Third, several probes, including macrophage- and neutrophil- targeting NIR probes and pH probes, used either PNIPAM particle or PEG polymer as carriers. It is well established that carriers' sizes would affect their penetration depth and circulation time. More studies are needed to optimize the current design for each probe.

Fourth, our recent studies have demonstrated that folate probes can be modified to detect foreign body reactions using PET imaging. To bridge the gaps between our research and clinical applications, additional studies are needed to explore the possibility of detecting different inflammatory processes in various inflammatory disease conditions.

Finally, several assumptions have been made on the development of 3D imaging models. To further improve the model, a standard curve of fluorescence data should be obtained under identical conditions to better correct for the light penetration and scattering properties at different wavelength. To address the variations due to spatial variations in the refractive indexes of different tissues, a deconvolution approach could be used to apply scattering corrections into small animal optical images similar to those used for PET scattering

corrections. Furthermore, the effectiveness of computational work need to be optimized and is a topic for our future work.

REFERENCES


1. Punnia-Moorthy, A., *Evaluation of pH changes in inflammation of the subcutaneous air pouch lining in the rat, induced by carrageenan, dextran and Staphylococcus aureus.* J Oral Pathol, 1987. **16**(1): p. 36-44.
2. De Backer, D., *Lactic acidosis.* Minerva Anestesiol, 2003. **69**(4): p. 281-4.
3. Eming, S.A., T. Krieg, and J.M. Davidson, *Inflammation in wound repair: molecular and cellular mechanisms.* J Invest Dermatol, 2007. **127**(3): p. 514-25.
4. Ramos, B.F., Y. Zhang, and B.A. Jakschik, *Mast cells contribute to fibrin deposition in reverse passive Arthus reaction in mouse skin.* Eur J Immunol, 1992. **22**(9): p. 2381-5.
5. Tang, L. and J.W. Eaton, *Fibrin(ogen) mediates acute inflammatory responses to biomaterials.* J Exp Med, 1993. **178**(6): p. 2147-56.
6. Valent, P., et al., *What have mast cells to do with edema formation, the consecutive repair and fibrinolysis?* Int Arch Allergy Immunol, 1998. **115**(1): p. 2-8.
7. Trautmann, A., et al., *Mast cell involvement in normal human skin wound healing: expression of monocyte chemoattractant protein-1 is correlated with recruitment of mast cells which synthesize interleukin-4 in vivo.* J Pathol, 2000. **190**(1): p. 100-6.
8. Martin, P. and S.J. Leibovich, *Inflammatory cells during wound repair: the good, the bad and the ugly.* Trends Cell Biol, 2005. **15**(11): p. 599-607.
9. Yurt, R.W. and B.A. Pruitt, Jr., *Decreased wound neutrophils and indiscrete margination in the pathogenesis of wound infection.* Surgery, 1985. **98**(2): p. 191-8.
10. Tang, L. and J.W. Eaton, *Inflammatory responses to biomaterials.* Am J Clin Pathol, 1995. **103**(4): p. 466-71.
11. Tang, L. and J.W. Eaton, *Natural responses to unnatural materials: A molecular mechanism for foreign body reactions.* Mol Med, 1999. **5**(6): p. 351-8.
12. Zhou, J., et al., *Real-time detection of implant-associated neutrophil responses using a formyl peptide receptor-targeting NIR nanoprobe.* Int J Nanomedicine, 2012. **7**: p. 2057-68.
13. Weiss, S.J., *Tissue destruction by neutrophils.* N Engl J Med, 1989. **320**(6): p. 365-76.
14. Sutherland, K., et al., *Degradation of biomaterials by phagocyte-derived oxidants.* J Clin Invest, 1993. **92**(5): p. 2360-7.
15. Ye, Q., et al., *The relationship between collagen scaffold cross-linking agents and neutrophils in the foreign body reaction.* Biomaterials, 2010. **31**(35): p. 9192-201.
16. Freeman, T.A., et al., *Reactive oxygen and nitrogen species induce protein and DNA modifications driving arthrofibrosis following total knee arthroplasty.* Fibrogenesis Tissue Repair, 2009. **2**(1): p. 5.
17. McCormick, T.S., S.R. Stevens, and K. Kang, *Macrophages and cutaneous inflammation.* Nat Biotechnol, 2000. **18**(1): p. 25-6.
18. Fujiwara, N. and K. Kobayashi, *Macrophages in inflammation.* Curr Drug Targets Inflamm Allergy, 2005. **4**(3): p. 281-6.
19. Steen, K.H., A.E. Steen, and P.W. Reeh, *A dominant role of acid pH in inflammatory excitation and sensitization of nociceptors in rat skin, in vitro.* J Neurosci, 1995. **15**(5 Pt 2): p. 3982-9.
20. Reeh, P.W. and K.H. Steen, *Tissue acidosis in nociception and pain.* Prog Brain Res, 1996. **113**: p. 143-51.
21. Mainnemare, A., et al., *Hypochlorous acid and taurine-N-monochloramine in periodontal diseases.* J Dent Res, 2004. **83**(11): p. 823-31.

22. Goldsmith, S.J. and S. Vallabhajosula, *Clinically proven radiopharmaceuticals for infection imaging: mechanisms and applications.* Semin Nucl Med, 2009. **39**(1): p. 2-10.
23. Lu, H., W. Ouyang, and C. Huang, *Inflammation, a key event in cancer development.* Mol Cancer Res, 2006. **4**(4): p. 221-33.
24. Monaco, C., et al., *T-cell-mediated signalling in immune, inflammatory and angiogenic processes: the cascade of events leading to inflammatory diseases.* Curr Drug Targets Inflamm Allergy, 2004. **3**(1): p. 35-42.
25. Grandics, P., *The cancer stem cell: evidence for its origin as an injured autoreactive T cell.* Mol Cancer, 2006. **5**: p. 6.
26. Anderson, J.M., A. Rodriguez, and D.T. Chang, *Foreign body reaction to biomaterials.* Semin Immunol, 2008. **20**(2): p. 86-100.
27. Baker, D.W., et al., *Fibroblast/fibrocyte: surface interaction dictates tissue reactions to micropillar implants.* Biomacromolecules, 2011. **12**(4): p. 997-1005.
28. Sabaliauskas, N.A., et al., *High-throughput zebrafish histology.* Methods, 2006. **39**(3): p. 246-54.
29. Gerstner, A.O., et al., *Quantitative histology by multicolor slide-based cytometry.* Cytometry A, 2004. **59**(2): p. 210-9.
30. Gotthardt, M., et al., *Imaging of inflammation by PET, conventional scintigraphy, and other imaging techniques.* J Nucl Med, 2010. **51**(12): p. 1937-49.
31. Ntziachristos, V., C. Bremer, and R. Weissleder, *Fluorescence imaging with near-infrared light: new technological advances that enable in vivo molecular imaging.* Eur Radiol, 2003. **13**(1): p. 195-208.
32. Quek, C.-H. and K.W. Leong, *Near-Infrared Fluorescent Nanoprobes for in Vivo Optical Imaging.* Nanomaterials, 2012. **2**(2): p. 92-112.
33. Boerman, O.C., et al., *Radiopharmaceuticals for scintigraphic imaging of infection and inflammation.* Inflamm Res, 2001. **50**(2): p. 55-64.
34. Vasanth, L.C., et al., *Using magnetic resonance angiography to measure abnormal synovial blood vessels in early inflammatory arthritis: a new imaging biomarker?* J Rheumatol, 2010. **37**(6): p. 1129-35.
35. McQueen, F.M., *Magnetic resonance imaging in early inflammatory arthritis: what is its role?* Rheumatology (Oxford), 2000. **39**(7): p. 700-6.
36. Kuseler, A., et al., *Contrast enhanced magnetic resonance imaging as a method to diagnose early inflammatory changes in the temporomandibular joint in children with juvenile chronic arthritis.* J Rheumatol, 1998. **25**(7): p. 1406-12.
37. Weinstein, J.S., et al., *Superparamagnetic iron oxide nanoparticles: diagnostic magnetic resonance imaging and potential therapeutic applications in neurooncology and central nervous system inflammatory pathologies, a review.* J Cereb Blood Flow Metab, 2010. **30**(1): p. 15-35.
38. Temme, S., et al., *19F magnetic resonance imaging of endogenous macrophages in inflammation.* Wiley Interdiscip Rev Nanomed Nanobiotechnol, 2012. **4**(3): p. 329-43.
39. Fornage, M., et al., *Biomarkers of Inflammation and MRI-Defined Small Vessel Disease of the Brain: The Cardiovascular Health Study.* Stroke, 2008. **39**(7): p. 1952-9.
40. McAteer, M.A., et al., *Magnetic resonance imaging of brain inflammation using microparticles of iron oxide.* Methods Mol Biol, 2011. **680**: p. 103-15.
41. McAteer, M.A., et al., *A leukocyte-mimetic magnetic resonance imaging contrast agent homes rapidly to activated endothelium and tracks with atherosclerotic lesion macrophage content.* Arterioscler Thromb Vasc Biol, 2012. **32**(6): p. 1427-35.

42. Na, H.B., I.C. Song, and T. Hyeon, *Inorganic Nanoparticles for MRI Contrast Agents.* Advanced Materials, 2009. **21**(21): p. 2133-2148.
43. Strijkers, G.J., et al., *MRI contrast agents: current status and future perspectives.* Anticancer Agents Med Chem, 2007. **7**(3): p. 291-305.
44. Lindner, J.R., *Microbubbles in medical imaging: current applications and future directions.* Nat Rev Drug Discov, 2004. **3**(6): p. 527-32.
45. Schneider, M., *SonoVue, a new ultrasound contrast agent.* Eur Radiol, 1999. **9 Suppl 3**: p. S347-8.
46. Takalkar, A.M., et al., *Binding and detachment dynamics of microbubbles targeted to P-selectin under controlled shear flow.* J Control Release, 2004. **96**(3): p. 473-82.
47. Eniola, A.O., P.J. Willcox, and D.A. Hammer, *Interplay between rolling and firm adhesion elucidated with a cell-free system engineered with two distinct receptor-ligand pairs.* Biophys J, 2003. **85**(4): p. 2720-31.
48. Omolola Eniola, A. and D.A. Hammer, *In vitro characterization of leukocyte mimetic for targeting therapeutics to the endothelium using two receptors.* Biomaterials, 2005. **26**(34): p. 7136-44.
49. Weller, G.E., et al., *Targeted ultrasound contrast agents: in vitro assessment of endothelial dysfunction and multi-targeting to ICAM-1 and sialyl Lewisx.* Biotechnol Bioeng, 2005. **92**(6): p. 780-8.
50. Hilderbrand, S.A., et al., *Near infrared fluorescence-based bacteriophage particles for ratiometric pH imaging.* Bioconjug Chem, 2008. **19**(8): p. 1635-9.
51. Ji, J., et al., *Synthesis and application of submicrometer fluorescence sensing particles for lysosomal pH measurements in murine macrophages.* Anal Chem, 2000. **72**(15): p. 3497-503.
52. Rudd, J.H., et al., *Imaging atherosclerotic plaque inflammation with [18F]-fluorodeoxyglucose positron emission tomography.* Circulation, 2002. **105**(23): p. 2708-11.
53. Keyaerts, M., et al., *Dynamic bioluminescence imaging for quantitative tumour burden assessment using IV or IP administration of D: -luciferin: effect on intensity, time kinetics and repeatability of photon emission.* Eur J Nucl Med Mol Imaging, 2008. **35**(5): p. 999-1007.
54. Weissleder, R. and U. Mahmood, *Molecular imaging.* Radiology, 2001. **219**(2): p. 316-33.
55. Low, P.S., W.A. Henne, and D.D. Doorneweerd, *Discovery and development of folic-acid-based receptor targeting for imaging and therapy of cancer and inflammatory diseases.* Acc Chem Res, 2008. **41**(1): p. 120-9.
56. Dinarello, C.A., *Immunological and inflammatory functions of the interleukin-1 family.* Annu Rev Immunol, 2009. **27**: p. 519-50.
57. Carlsen, H., et al., *In vivo imaging of NF-kappa B activity.* J Immunol, 2002. **168**(3): p. 1441-6.
58. Kielland, A., et al., *In vivo imaging of reactive oxygen and nitrogen species in inflammation using the luminescent probe L-012.* Free Radical Biology and Medicine, 2009. **47**(6): p. 760-766.
59. Liu, W.F., et al., *Real-time in vivo detection of biomaterial-induced reactive oxygen species.* Biomaterials, 2011. **32**(7): p. 1796-1801.
60. Hillman, E.M. and A. Moore, *All-optical anatomical co-registration for molecular imaging of small animals using dynamic contrast.* Nat Photonics, 2007. **1**(9): p. 526-530.

61. Walls, J.R., et al., *Correction of artefacts in optical projection tomography.* Phys Med Biol, 2005. **50**(19): p. 4645-65.
62. Meyer, H., et al., *Noncontact optical imaging in mice with full angular coverage and automatic surface extraction.* Appl Opt, 2007. **46**(17): p. 3617-27.
63. Cao, X., et al., *Reconstruction for limited-projection fluorescence molecular tomography based on projected restarted conjugate gradient normal residual.* Opt Lett, 2011. **36**(23): p. 4515-7.
64. Zilberman, Y., et al., *Fluorescence molecular tomography enables in vivo visualization and quantification of nonunion fracture repair induced by genetically engineered mesenchymal stem cells.* J Orthop Res, 2008. **26**(4): p. 522-30.
65. Akassoglou, K., et al., *Fibrin depletion decreases inflammation and delays the onset of demyelination in a tumor necrosis factor transgenic mouse model for multiple sclerosis.* Proc Natl Acad Sci U S A, 2004. **101**(17): p. 6698-703.
66. Tang, L., A.H. Lucas, and J.W. Eaton, *Inflammatory responses to implanted polymeric biomaterials: role of surface-adsorbed immunoglobulin G.* J Lab Clin Med, 1993. **122**(3): p. 292-300.
67. Nayak, S., et al., *Folate-Mediated Cell Targeting and Cytotoxicity Using Thermoresponsive Microgels.* Journal of the American Chemical Society, 2004. **126**(33): p. 10258-10259.
68. Daiber, A., et al., *Measurement of NAD(P)H oxidase-derived superoxide with the luminol analogue L-012.* Free Radical Biology and Medicine, 2004. **36**(1): p. 101-111.
69. Daiber, A., et al., *Detection of superoxide and peroxynitrite in model systems and mitochondria by the luminol analogue L-012.* Free Radic Res, 2004. **38**(3): p. 259-69.
70. Zhuang, H. and A. Alavi, *18-fluorodeoxyglucose positron emission tomographic imaging in the detection and monitoring of infection and inflammation.* Semin Nucl Med, 2002. **32**(1): p. 47-59.
71. Townsend, K.A., G. Wollstein, and J.S. Schuman, *Clinical application of MRI in ophthalmology.* NMR Biomed, 2008. **21**(9): p. 997-1002.
72. Li, S.K., M.J. Lizak, and E.K. Jeong, *MRI in ocular drug delivery.* NMR Biomed, 2008. **21**(9): p. 941-56.
73. Hu, W.J., et al., *Molecular basis of biomaterial-mediated foreign body reactions.* Blood, 2001. **98**(4): p. 1231-8.
74. Smiley, S.T., J.A. King, and W.W. Hancock, *Fibrinogen stimulates macrophage chemokine secretion through toll-like receptor 4.* J Immunol, 2001. **167**(5): p. 2887-94.
75. Languino, L.R., et al., *Fibrinogen Mediates Leukocyte Adhesion to Vascular Endothelium through an Icam-1-Dependent Pathway.* Cell, 1993. **73**(7): p. 1423-1434.
76. Altieri, D.C., et al., *Oligospecificity of the cellular adhesion receptor Mac-1 encompasses an inducible recognition specificity for fibrinogen.* J Cell Biol, 1988. **107**(5): p. 1893-900.
77. Loike, J.D., et al., *CD11c/CD18 on neutrophils recognizes a domain at the N terminus of the A alpha chain of fibrinogen.* Proc Natl Acad Sci U S A, 1991. **88**(3): p. 1044-8.
78. Perez, R.L. and J. Roman, *Fibrin enhances the expression of IL-1 beta by human peripheral blood mononuclear cells. Implications in pulmonary inflammation.* J Immunol, 1995. **154**(4): p. 1879-87.
79. Szaba, F.M. and S.T. Smiley, *Roles for thrombin and fibrin(ogen) in cytokine/chemokine production and macrophage adhesion in vivo.* Blood, 2002. **99**(3): p. 1053-9.
80. Tang, L., et al., *Molecular determinants of acute inflammatory responses to biomaterials.* J Clin Invest, 1996. **97**(5): p. 1329-34.

81. Zdolsek, J., J.W. Eaton, and L. Tang, *Histamine release and fibrinogen adsorption mediate acute inflammatory responses to biomaterial implants in humans.* J Transl Med, 2007. **5**: p. 31.
82. Tang, L., T.A. Jennings, and J.W. Eaton, *Mast cells mediate acute inflammatory responses to implanted biomaterials.* Proc Natl Acad Sci U S A, 1998. **95**(15): p. 8841-6.
83. McCarthy, J.R., et al., *Multimodal Nanoagents for the Detection of Intravascular Thrombi.* Bioconjugate Chemistry, 2009. **20**(6): p. 1251-1255.
84. Zhang, Y., et al., *In vivo near-infrared imaging of fibrin deposition in thromboembolic stroke in mice.* PLoS One, 2012. **7**(1): p. e30262.
85. Sohaebuddin, S.K., et al., *Nanomaterial cytotoxicity is composition, size, and cell type dependent.* Part Fibre Toxicol, 2010. **7**: p. 22.
86. Neeves, K.B., D.A. Illing, and S.L. Diamond, *Thrombin flux and wall shear rate regulate fibrin fiber deposition state during polymerization under flow.* Biophys J, 2010. **98**(7): p. 1344-52.
87. Zhou, J., et al., *Real time monitoring of biomaterial-mediated inflammatory responses via macrophage-targeting NIR nanoprobes.* Biomaterials, 2011. **32**: p. 9383-9390.
88. Gray, L.D., et al., *Recombinant factor VIIa analog NN1731 (V158D/E296V/M298Q-FVIIa) enhances fibrin formation, structure and stability in lipidated hemophilic plasma.* Thromb Res, 2011. **128**(6): p. 570-6.
89. Hogg, P.J., et al., *Binding of fibrin monomer and heparin to thrombin in a ternary complex alters the environment of the thrombin catalytic site, reduces affinity for hirudin, and inhibits cleavage of fibrinogen.* J Biol Chem, 1996. **271**(42): p. 26088-95.
90. Simmons, C.A., M.D. Burdick, and R.G. Schaub, *Heparin inhibits fibrin, but not leukocytes, in a model of deep-vein thrombosis.* J Surg Res, 1987. **43**(5): p. 468-75.
91. Zhou, J., et al., *Noninvasive assessment of localized inflammatory responses.* Free Radic Biol Med, 2012. **52**(1): p. 218-26.
92. Dorozhkin, S.V., *Biocomposites and hybrid biomaterials based on calcium orthophosphates.* Biomatter, 2011. **1**(1): p. 3-56.
93. Kokubo, T., H.M. Kim, and M. Kawashita, *Novel bioactive materials with different mechanical properties.* Biomaterials, 2003. **24**(13): p. 2161-75.
94. Bratlie, K.M., et al., *Rapid biocompatibility analysis of materials via in vivo fluorescence imaging of mouse models.* PLoS One, 2010. **5**(4): p. e10032.
95. Ma, M., et al., *Development of cationic polymer coatings to regulate foreign-body responses.* Adv Mater, 2011. **23**(24): p. H189-94.
96. Coleman, J.W., *Nitric oxide: a regulator of mast cell activation and mast cell-mediated inflammation.* Clin Exp Immunol, 2002. **129**(1): p. 4-10.
97. van Hinsbergh, V.W., A. Collen, and P. Koolwijk, *Role of fibrin matrix in angiogenesis.* Ann N Y Acad Sci, 2001. **936**: p. 426-37.
98. Pereira, M. and P.J. Simpson-Haidaris, *Fibrinogen modulates gene expression in wounded fibroblasts.* Ann N Y Acad Sci, 2001. **936**: p. 438-43.
99. Simpson-Haidaris, P.J. and B. Rybarczyk, *Tumors and fibrinogen. The role of fibrinogen as an extracellular matrix protein.* Ann N Y Acad Sci, 2001. **936**: p. 406-25.
100. Laudano, A.P. and R.F. Doolittle, *Synthetic peptide derivatives that bind to fibrinogen and prevent the polymerization of fibrin monomers.* Proceedings of the National Academy of Sciences, 1978. **75**(7): p. 3085-3089.
101. Aruva, M.R., et al., *Imaging thromboembolism with fibrin-avid 99mTc-peptide: evaluation in swine.* J Nucl Med, 2006. **47**(1): p. 155-62.

102. Thakur, M.L., et al., *Imaging vascular thrombosis with 99mTc-labeled fibrin alpha-chain peptide.* J Nucl Med, 2000. **41**(1): p. 161-8.
103. Frangioni, J.V., *In vivo near-infrared fluorescence imaging.* Curr Opin Chem Biol, 2003. **7**(5): p. 626-34.
104. Andre, P., et al., *Pro-coagulant state resulting from high levels of soluble P-selectin in blood.* Proc Natl Acad Sci U S A, 2000. **97**(25): p. 13835-40.
105. Cooley, B.C., *In vivo fluorescence imaging of large-vessel thrombosis in mice.* Arterioscler Thromb Vasc Biol, 2011. **31**(6): p. 1351-6.
106. Aspenberg, P. and O. Virchenko, *Platelet concentrate injection improves Achilles tendon repair in rats.* Acta Orthop Scand, 2004. **75**(1): p. 93-9.
107. Gomi, K., et al., *Antithrombotic effect of recombinant human thrombomodulin on thrombin-induced thromboembolism in mice.* Blood, 1990. **75**(7): p. 1396-9.
108. Tang, L. and W. Hu, *Molecular determinants of biocompatibility.* Expert Rev Med Devices, 2005. **2**(4): p. 493-500.
109. Metz, M. and M. Maurer, *Mast cells--key effector cells in immune responses.* Trends Immunol, 2007. **28**(5): p. 234-41.
110. Hattori, Y., M. Sakaguchi, and Y. Maitani, *Folate-linked lipid-based nanoparticles deliver a NFkappaB decoy into activated murine macrophage-like RAW264.7 cells.* Biol Pharm Bull, 2006. **29**(7): p. 1516-20.
111. Thakur, M.L., et al., *Indium-111-labeled autologous leukocytes in man.* J Nucl Med, 1977. **18**(10): p. 1014-21.
112. Fischman, A.J., et al., *Imaging focal sites of bacterial infection in rats with indium-111-labeled chemotactic peptide analogs.* J Nucl Med, 1991. **32**(3): p. 483-91.
113. Babich, J.W., et al., *Localization of radiolabeled chemotactic peptide at focal sites of Escherichia coli infection in rabbits: evidence for a receptor-specific mechanism.* J Nucl Med, 1997. **38**(8): p. 1316-22.
114. Derian, C.K., et al., *Selective inhibition of N-formylpeptide-induced neutrophil activation by carbamate-modified peptide analogues.* Biochemistry, 1996. **35**(4): p. 1265-9.
115. Fischman, A.J., et al., *Imaging Focal Sites of Bacterial-Infection in Rats with Indium-111-Labeled Chemotactic Peptide Analogs.* Journal of Nuclear Medicine, 1991. **32**(3): p. 483-491.
116. vanderLaken, C.J., et al., *Technetium-99m-labeled chemotactic peptides in acute infection and sterile inflammation.* Journal of Nuclear Medicine, 1997. **38**(8): p. 1310-1315.
117. Xiao, L., et al., *Synthesis of the Cyanine 7 labeled neutrophil-specific agents for noninvasive near infrared fluorescence imaging.* Bioorganic & Medicinal Chemistry Letters, 2010. **20**(12): p. 3515-3517.
118. Hilgenbrink, A.R. and P.S. Low, *Folate receptor-mediated drug targeting: From therapeutics to diagnostics.* Journal of Pharmaceutical Sciences, 2005. **94**(10): p. 2135-2146.
119. Chen, W.T., et al., *Arthritis imaging using a near-infrared fluorescence folate-targeted probe.* Arthritis Research & Therapy, 2005. **7**(2): p. R310-R317.
120. Paulos, C.M., et al., *Folate receptor-mediated targeting of therapeutic and imaging agents to activated macrophages in rheumatoid arthritis.* Advanced Drug Delivery Reviews, 2004. **56**(8): p. 1205-1217.
121. Lifland, A.W., C. Zurla, and P.J. Santangelo, *Single Molecule Sensitive Multivalent Polyethylene Glycol Probes for RNA Imaging.* Bioconjug Chem, 2010.

122. Henderson, R.B., et al., *Rapid recruitment of inflammatory monocytes is independent of neutrophil migration.* Blood, 2003. **102**(1): p. 328-35.
123. Hao, Q., et al., *Neutrophil depletion decreases VEGF-induced focal angiogenesis in the mature mouse brain.* J Cereb Blood Flow Metab, 2007. **27**(11): p. 1853-60.
124. Lorenz, U., et al., *In vivo detection of Staphylococcus aureus in biofilm on vascular prostheses using non-invasive biophotonic imaging.* Eur J Vasc Endovasc Surg, 2011. **41**(1): p. 68-75.
125. Mermel, L.A., S.M. Stolz, and D.G. Maki, *Surface antimicrobial activity of heparin-bonded and antiseptic-impregnated vascular catheters.* J Infect Dis, 1993. **167**(4): p. 920-4.
126. Thevenot, P.T., et al., *The effect of incorporation of SDF-1alpha into PLGA scaffolds on stem cell recruitment and the inflammatory response.* Biomaterials, 2010. **31**(14): p. 3997-4008.
127. Weng, H., et al., *Tissue responses to thermally-responsive hydrogel nanoparticles.* J Biomater Sci Polym Ed, 2004. **15**(9): p. 1167-80.
128. Xiao, L., et al., *Synthesis of the Cyanine 7 labeled neutrophil-specific agents for noninvasive near infrared fluorescence imaging.* Bioorg Med Chem Lett, 2010. **20**(12): p. 3515-7.
129. Locke, L.W., et al., *A novel neutrophil-specific PET imaging agent: cFLFLFK-PEG-64Cu.* J Nucl Med, 2009. **50**(5): p. 790-7.
130. Fakhari, A., et al., *Controlling ligand surface density optimizes nanoparticle binding to ICAM-1.* J Pharm Sci, 2011. **100**(3): p. 1045-56.
131. Healy, J.M., et al., *Pharmacokinetics and biodistribution of novel aptamer compositions.* Pharm Res, 2004. **21**(12): p. 2234-46.
132. Suzuki, T., et al., *Physicochemical and biological properties of poly(ethylene glycol)-coupled immunoglobulin G.* Biochim Biophys Acta, 1984. **788**(2): p. 248-55.
133. Niedel, J.E., I. Kahane, and P. Cuatrecasas, *Receptor-mediated internalization of fluorescent chemotactic peptide by human neutrophils.* Science, 1979. **205**(4413): p. 1412-4.
134. Johansson, B., et al., *N-formyl peptide receptors in human neutrophils display distinct membrane distribution and lateral mobility when labeled with agonist and antagonist.* The Journal of cell biology, 1993. **121**(6): p. 1281-9.
135. Stephenson, K.A., et al., *Bridging the gap between in vitro and in vivo imaging: isostructural Re and 99mTc complexes for correlating fluorescence and radioimaging studies.* Journal of the American Chemical Society, 2004. **126**(28): p. 8598-9.
136. Jeyaseelan, S., et al., *Transcriptional profiling of lipopolysaccharide-induced acute lung injury.* Infection and Immunity, 2004. **72**(12): p. 7247-7256.
137. Zhou, H., et al., *Role of Endothelial TLR4 for Neutrophil Recruitment into Central Nervous System Microvessels in Systemic Inflammation.* Journal of Immunology, 2009. **183**(8): p. 5244-5250.
138. Bhatia, M., et al., *The effects of neutrophil depletion on a completely noninvasive model of acute pancreatitis-associated lung injury.* Int J Pancreatol, 1998. **24**(2): p. 77-83.
139. Iyer, A.K., et al., *Exploiting the enhanced permeability and retention effect for tumor targeting.* Drug Discov Today, 2006. **11**(17-18): p. 812-8.
140. Hirose, K., et al., *A novel approach to reduce catheter-related infection using sustained-release basic fibroblast growth factor for tissue regeneration in mice.* Heart and Vessels, 2007. **22**(4): p. 261-267.

141. Zhou, J., et al., *In vivo evaluation of medical device-associated inflammation using a macrophage-specific positron emission tomography (PET) imaging probe.* Bioorganic & Medicinal Chemistry Letters, 2013. **23**(7): p. 2044-2047.
142. Blackburn, W.H. and L.A. Lyon, *Size Controlled Synthesis of Monodispersed, Core/Shell Nanogels.* Colloid Polym Sci, 2008. **286**(5): p. 563-569.
143. Hellweg, T., et al., *PNIPAM-co-polystyrene core-shell microgels: structure, swelling behavior, and crystallization.* Langmuir, 2004. **20**(11): p. 4330-5.
144. Ji, T., et al., *Increased Sensitivity in Antigen Detection with Fluorescent Latex Nanosphere-IgG Antibody Conjugates.* Bioconjug Chem, 2010.
145. Dube, D., et al., *Preparation and tumor cell uptake of poly(N-isopropylacrylamide) folate conjugates.* Bioconjug Chem, 2002. **13**(3): p. 685-92.
146. Paliwal, R., et al., *Cell-selective mitochondrial targeting: progress in mitochondrial medicine.* Curr Drug Deliv, 2007. **4**(3): p. 211-24.
147. Quintana, A., et al., *Design and function of a dendrimer-based therapeutic nanodevice targeted to tumor cells through the folate receptor.* Pharm Res, 2002. **19**(9): p. 1310-6.
148. Henne, W.A., et al., *Detection of folate binding protein with enhanced sensitivity using a functionalized quartz crystal microbalance sensor.* Anal Chem, 2006. **78**(14): p. 4880-4.
149. Antohe, F., et al., *Increased uptake of folate conjugates by activated macrophages in experimental hyperlipemia.* Cell Tissue Res, 2005. **320**(2): p. 277-85.
150. Shapira, L., et al., *Protection against endotoxic shock and lipopolysaccharide-induced local inflammation by tetracycline: correlation with inhibition of cytokine secretion.* Infect Immun, 1996. **64**(3): p. 825-8.
151. Hansch, A., et al., *In vivo imaging of experimental arthritis with near-infrared fluorescence.* Arthritis Rheum, 2004. **50**(3): p. 961-7.
152. Weissleder, R., et al., *In vivo imaging of tumors with protease-activated near-infrared fluorescent probes.* Nat Biotechnol, 1999. **17**(4): p. 375-8.
153. Zhang, J., et al., *The targeted behavior of thermally responsive nanohydrogel evaluated by NIR system in mouse model.* J Control Release, 2008. **131**(1): p. 34-40.
154. Ruan, G. and S.S. Feng, *Preparation and characterization of poly(lactic acid)-poly(ethylene glycol)-poly(lactic acid) (PLA-PEG-PLA) microspheres for controlled release of paclitaxel.* Biomaterials, 2003. **24**(27): p. 5037-44.
155. Aggarwal, P., et al., *Nanoparticle interaction with plasma proteins as it relates to particle biodistribution, biocompatibility and therapeutic efficacy.* Advanced Drug Delivery Reviews, 2009. **61**(6): p. 428-437.
156. Cedervall, T., et al., *Understanding the nanoparticle-protein corona using methods to quantify exchange rates and affinities of proteins for nanoparticles.* Proceedings of the National Academy of Sciences of the United States of America, 2007. **104**(7): p. 2050-2055.
157. Sutton, D., et al., *Functionalized micellar systems for cancer targeted drug delivery.* Pharmaceutical Research, 2007. **24**(6): p. 1029-1046.
158. Turk, M.J., et al., *Folate-targeted imaging of activated macrophages in rats with adjuvant-induced arthritis.* Arthritis Rheum, 2002. **46**(7): p. 1947-55.
159. Schutte, R.J., et al., *In vivo cytokine-associated responses to biomaterials.* Biomaterials, 2009. **30**(2): p. 160-8.
160. Lang, C.H., et al., *Endotoxin stimulates in vivo expression of inflammatory cytokines tumor necrosis factor alpha, interleukin-1beta, -6, and high-mobility-group protein-1 in skeletal muscle.* Shock, 2003. **19**(6): p. 538-46.

161. Koning, G.A., et al., *Targeting of angiogenic endothelial cells at sites of inflammation by dexamethasone phosphate-containing RGD peptide liposomes inhibits experimental arthritis.* Arthritis and Rheumatism, 2006. **54**(4): p. 1198-1208.
162. Maeda, H., G.Y. Bharate, and J. Daruwalla, *Polymeric drugs for efficient tumor-targeted drug delivery based on EPR-effect.* Eur J Pharm Biopharm, 2009. **71**(3): p. 409-19.
163. Greenhalgh, D.G., *The role of apoptosis in wound healing.* Int J Biochem Cell Biol, 1998. **30**(9): p. 1019-30.
164. Halliwell, B. and M. Whiteman, *Measuring reactive species and oxidative damage in vivo and in cell culture: how should you do it and what do the results mean?* British Journal of Pharmacology, 2004. **142**(2): p. 231-255.
165. Lee, D., et al., *In vivo imaging of hydrogen peroxide with chemiluminescent nanoparticles.* Nature Materials, 2007. **6**(10): p. 765-769.
166. Lee, D., et al., *Detection of hydrogen peroxide with chemiluminescent micelles.* Int J Nanomedicine, 2008. **3**(4): p. 471-6.
167. Panizzi, P., et al., *Oxazine Conjugated Nanoparticle Detects in Vivo Hypochlorous Acid and Peroxynitrite Generation.* Journal of the American Chemical Society, 2009. **131**(43): p. 15739-15744.
168. Chen, W.T., C.H. Tung, and R. Weissleder, *Imaging reactive oxygen species in arthritis.* Mol Imaging, 2004. **3**(3): p. 159-62.
169. Gross, S., et al., *Bioluminescence imaging of myeloperoxidase activity in vivo.* Nat Med, 2009. **15**(4): p. 455-61.
170. Liu, W.F., et al., *Real-time in vivo detection of biomaterial-induced reactive oxygen species.* Biomaterials, 2010.
171. Jahde, E. and M.F. Rajewsky, *Tumor-selective modification of cellular microenvironment in vivo: effect of glucose infusion on the pH in normal and malignant rat tissues.* Cancer Res, 1982. **42**(4): p. 1505-12.
172. Gerweck, L.E., S. Vijayappa, and S. Kozin, *Tumor pH controls the in vivo efficacy of weak acid and base chemotherapeutics.* Mol Cancer Ther, 2006. **5**(5): p. 1275-9.
173. Sun, H., et al., *Synthesis and characterization of ratiometric, pH sensing nanoparticles with covalently attached fluorescent dyes.* Chemistry of Materials, 2006. **18**(15): p. 3381-3384.
174. Lee, H., et al., *Near-Infrared pH-Activatable Fluorescent Probes for Imaging Primary and Metastatic Breast Tumors.* Bioconjug Chem, 2011.
175. Davis, M.H., et al., *Estimation of intramitochondrial pCa and pH by fura-2 and 2,7 biscarboxyethyl-5(6)-carboxyfluorescein (BCECF) fluorescence.* Biochem Biophys Res Commun, 1987. **149**(1): p. 40-5.
176. Martin, G.R. and R.K. Jain, *Noninvasive measurement of interstitial pH profiles in normal and neoplastic tissue using fluorescence ratio imaging microscopy.* Cancer Res, 1994. **54**(21): p. 5670-4.
177. Myochin, T., et al., *Rational design of ratiometric near-infrared fluorescent pH probes with various pKa values, based on aminocyanine.* J Am Chem Soc, 2011. **133**(10): p. 3401-9.
178. Kohchi, C., et al., *ROS and innate immunity.* Anticancer Res, 2009. **29**(3): p. 817-21.
179. Luo, Y. and M.E. Dorf, *Isolation of mouse neutrophils.* Curr Protoc Immunol, 2001. **Chapter 3**: p. Unit 3 20.
180. Kamath, S., et al., *Surface chemistry influences implant-mediated host tissue responses.* J Biomed Mater Res A, 2008. **86**(3): p. 617-26.

181. Park, H.S., et al., *Cutting edge: direct interaction of TLR4 with NAD(P)H oxidase 4 isozyme is essential for lipopolysaccharide-induced production of reactive oxygen species and activation of NF-kappa B.* J Immunol, 2004. **173**(6): p. 3589-93.
182. Miletic, A.V., et al., *Vav proteins control MyD88-dependent oxidative burst.* Blood, 2007. **109**(8): p. 3360-8.
183. Sun, Y.G., et al., *Cellular basis of itch sensation.* Science, 2009. **325**(5947): p. 1531-4.
184. Liu, T., et al., *Toll-like receptor 7 mediates pruritus.* Nat Neurosci, 2010. **13**(12): p. 1460-2.
185. Tomoe, S., et al., *Comparison of substance P-induced and compound 48/80-induced neutrophil infiltrations in mouse skin.* Int Arch Allergy Immunol, 1992. **97**(3): p. 237-42.
186. Riley, J.F. and G.B. West, *Tissue mast cells: studies with a histamine-liberator of low toxicity (compound 48/80).* J Pathol Bacteriol, 1955. **69**(1-2): p. 269-82.
187. Imada, I., et al., *Analysis of reactive oxygen species generated by neutrophils using a chemiluminescence probe L-012.* Anal Biochem, 1999. **271**(1): p. 53-8.
188. Samuni, A., et al., *On radical production by PMA-stimulated neutrophils as monitored by luminol-amplified chemiluminescence.* Free Radic Biol Med, 1991. **10**(5): p. 305-13.
189. Romson, J.L., et al., *Reduction of the extent of ischemic myocardial injury by neutrophil depletion in the dog.* Circulation, 1983. **67**(5): p. 1016-23.
190. Neumann, F.J., et al., *Cardiac release of cytokines and inflammatory responses in acute myocardial infarction.* Circulation, 1995. **92**(4): p. 748-55.
191. Valko, M., et al., *Free radicals and antioxidants in normal physiological functions and human disease.* Int J Biochem Cell Biol, 2007. **39**(1): p. 44-84.
192. Lademann, J., et al., *Application of optical non-invasive methods in skin physiology: a comparison of laser scanning microscopy and optical coherent tomography with histological analysis.* Skin Res Technol, 2007. **13**(2): p. 119-32.
193. Mason, W.T., *Fluorescent and luminescent probes for biological activity : a practical guide to technology for quantitative real-time analysis*. 2nd ed. Biological techniques. 1999, San Diego, Calif.: Academic Press. xxv, 647 p.
194. Yang, Z. and J.S. Marshall, *Zymosan treatment of mouse mast cells enhances dectin-1 expression and induces dectin-1-dependent reactive oxygen species (ROS) generation.* Immunobiology, 2009. **214**(4): p. 321-330.
195. Francois, P., et al., *Physical and biological effects of a surface coating procedure on polyurethane catheters.* Biomaterials, 1996. **17**(7): p. 667-78.
196. Krafte-Jacobs, B., et al., *Catheter-related thrombosis in critically ill children: comparison of catheters with and without heparin bonding.* J Pediatr, 1995. **126**(1): p. 50-4.
197. Du, Y.J., L.R. Berry, and A.K. Chan, *Chemical-Physical Characterization of Polyurethane Catheters Modified with a Novel Antithrombin-Heparin Covalent Complex.* J Biomater Sci Polym Ed, 2010.
198. Hoffmann, J., et al., *Blood cell and plasma protein repellent properties of Star-PEG-modified surfaces.* Journal of Biomaterials Science-Polymer Edition, 2006. **17**(9): p. 985-996.
199. Conus, S. and H.U. Simon, *Cathepsins: Key modulators of cell death and inflammatory responses.* Biochemical Pharmacology, 2008. **76**(11): p. 1374-1382.
200. Whiteman, M. and J.P.E. Spencer, *Loss of 3-chlorotyrosine by inflammatory oxidants: Implications for the use of 3-chlorotyrosine as a bio-marker in vivo.* Biochemical and Biophysical Research Communications, 2008. **371**(1): p. 50-53.
201. Andreev, O.A., et al., *Mechanism and uses of a membrane peptide that targets tumors and other acidic tissues in vivo.* Proc Natl Acad Sci U S A, 2007. **104**(19): p. 7893-8.

202. Carmo, V.A., et al., *Biodistribution study and identification of inflammation sites using 99mTc-labelled stealth pH-sensitive liposomes.* Nucl Med Commun, 2008. **29**(1): p. 33-8.
203. Weng, H., et al., *Tissue responses to thermally-responsive hydrogel nanoparticles.* J Biomat Sci-Polym E, 2004. **15**(9): p. 1167-1180.
204. Cai, T., M. Marquez, and Z. Hu, *Monodisperse thermoresponsive microgels of poly(ethylene glycol) analogue-based biopolymers.* Langmuir, 2007. **23**(17): p. 8663-6.
205. Gorbacheva, L., et al., *Activated protein C prevents glutamate- and thrombin-induced activation of nuclear factor-kappaB in cultured hippocampal neurons.* Neuroscience, 2010. **165**(4): p. 1138-46.
206. Overly, C.C., et al., *Quantitative measurement of intraorganelle pH in the endosomal-lysosomal pathway in neurons by using ratiometric imaging with pyranine.* Proc Natl Acad Sci U S A, 1995. **92**(8): p. 3156-60.
207. Nair, A., et al., *Biomaterial implants mediate autologous stem cell recruitment in mice.* Acta Biomater, 2011. **7**(11): p. 3887-95.
208. Nair, A., et al., *Species and density of implant surface chemistry affect the extent of foreign body reactions.* Langmuir, 2008. **24**(5): p. 2015-24.
209. Yu, Z., et al., *Comparative appraisal of clodronate, aspirin and dexamethasone as agents reducing alendronate-induced inflammation in a murine model.* Basic Clin Pharmacol Toxicol, 2005. **97**(4): p. 222-9.
210. Olmez, D., et al., *Efficacy of sulphasalazine on lung histopathology in a murine model of chronic asthma.* Exp Lung Res, 2008. **34**(8): p. 501-11.
211. Pelton, R.H. and P. Chibante, *Preparation of aqueous latices with N-isopropylacrylamide.* Colloids Surface, 1986. **20**(3): p. 247-256.
212. Ntziachristos, V., et al., *Looking and listening to light: the evolution of whole-body photonic imaging.* Nat Biotechnol, 2005. **23**(3): p. 313-20.
213. Kim, S., H.E. Pudavar, and P.N. Prasad, *Dye-concentrated organically modified silica nanoparticles as a ratiometric fluorescent pH probe by one- and two-photon excitation.* Chem Commun, 2006(19): p. 2071-2073.
214. Kircher, M.F., R. Weissleder, and L. Josephson, *A dual fluorochrome probe for imaging proteases.* Bioconjug Chem, 2004. **15**(2): p. 242-8.
215. Vijayasekaran, S., et al., *Cell viability and inflammatory response in hydrogel sponges implanted in the rabbit cornea.* Biomaterials, 1998. **19**(24): p. 2255-67.
216. Mi, F.L., et al., *In vivo biocompatibility and degradability of a novel injectable-chitosan-based implant.* Biomaterials, 2002. **23**(1): p. 181-91.
217. Liang, H.C., et al., *Effects of crosslinking degree of an acellular biological tissue on its tissue regeneration pattern.* Biomaterials, 2004. **25**(17): p. 3541-52.
218. La Flamme, K.E., et al., *Biocompatibility of nanoporous alumina membranes for immunoisolation.* Biomaterials, 2007. **28**(16): p. 2638-45.
219. Carmoa, V.A.S., et al., *Biodistribution study and identification of inflammation sites using Tc-99m-labelled stealth pH-sensitive liposomes.* Nucl Med Commun, 2008. **29**(1): p. 33-38.
220. Bellocq, A., et al., *Low environmental pH is responsible for the induction of nitric-oxide synthase in macrophages - Evidence for involvement of nuclear factor-kappa B activation.* J Biol Chem, 1998. **273**(9): p. 5086-5092.
221. Teichgraber, V., et al., *Ceramide accumulation mediates inflammation, cell death and infection susceptibility in cystic fibrosis.* Nat Med, 2008. **14**(4): p. 382-391.

222. Vihola, H., et al., *Cytotoxicity of thermosensitive polymers poly(N-isopropylacrylamide), poly(N-vinylcaprolactam) and amphiphilically modified poly(N-vinylcaprolactam).* Biomaterials, 2005. **26**(16): p. 3055-64.
223. Jaffer, F.A., et al., *Optical visualization of cathepsin K activity in atherosclerosis with a novel, protease-activatable fluorescence sensor.* Circulation, 2007. **115**(17): p. 2292-8.
224. Horisawa, E., et al., *Size-dependency of DL-lactide/glycolide copolymer particulates for intra-articular delivery system on phagocytosis in rat synovium.* Pharmaceut Res, 2002. **19**(2): p. 132-139.
225. Hoet, P.H., I. Bruske-Hohlfeld, and O.V. Salata, *Nanoparticles - known and unknown health risks.* J Nanobiotechnology, 2004. **2**(1): p. 12.
226. McNamara, K.P., et al., *Synthesis, characterization, and application of fluorescence sensing lipobeads for intracellular pH measurements.* Anal Chem, 2001. **73**(14): p. 3240-6.
227. Cai, W., et al., *Peptide-labeled near-infrared quantum dots for imaging tumor vasculature in living subjects.* Nano Lett, 2006. **6**(4): p. 669-76.
228. Liu, Z., et al., *Assessment of inflammatory response in ischemic rat hearts with various durations of reperfusion using a 99mTc-labeled dual-domain cytokine ligand.* J NUCL MED MEETING ABSTRACTS, 2012. **53**(1_MeetingAbstracts): p. 462-.
229. Tsyganov, E.N., et al., *Micro-SPECT combined with 3-D optical imaging.* 2004 IEEE Nuclear Science Symposium Conference Record, Vols 1-7, 2004: p. 3275-3279.
230. Manavaki, R., et al. *Scatter modeling for 3-d PET list-mode EM reconstruction*. in *Nuclear Science Symposium Conference Record, 2002 IEEE*. 2002.
231. Ripoll, J., et al., *Fast analytical approximation for arbitrary geometries in diffuse optical tomography.* Opt Lett, 2002. **27**(7): p. 527-9.
232. Markel, V.A. and J.C. Schotland, *Symmetries, inversion formulas, and image reconstruction for optical tomography.* Phys Rev E Stat Nonlin Soft Matter Phys, 2004. **70**(5 Pt 2): p. 056616.
233. Ripoll, J. and V. Ntziachristos, *Iterative boundary method for diffuse optical tomography.* J Opt Soc Am A Opt Image Sci Vis, 2003. **20**(6): p. 1103-10.
234. Wu, P., et al., *Detection of mouse liver cancer via a parallel iterative shrinkage method in hybrid optical/microcomputed tomography imaging.* J Biomed Opt, 2012. **17**(12): p. 126012.
235. Turner, G.M., et al., *Complete-angle projection diffuse optical tomography by use of early photons.* Opt Lett, 2005. **30**(4): p. 409-11.

## BIOGRAPHICAL INFORMATION

Yi-Ting Tsai was born on November 10, 1979 in Tauoyuan city, Taiwan. She received her Bachelor of Biomedical Engineering in Chung Yuan Christian University, Tauoyuan city, Taiwan in June 2001. In Fall 2001, she started her graduate studies in Institution of Biomedical Engineering, National Cheng Kung University, Tainan city, Taiwan and graduated with a Master of Science in June 2003. After completion of her Master's degree, she worked in Pacific Image Electronics Co., Ltd. (PIE) for a year and then worked at BenQ in Taipei, Taiwan, for three and an half years before enrolled into Ph. D program in Bioengineering Department at the University of Texas at Arlington in spring 2008. She has started her Doctoral studies in bioengineering department, the University of Texas at Arlington, under the supervision of Dr. Liping Tang. Her plan is to complete her Doctor of Philosophy in Biomedical Engineering at the joint graduate program of the University of Texas at Arlington and the University of Texas at Southwestern Medical Center at Dallas in May 2013. Her research interests include software development, optical imaging techniques, and medical imaging analyses.